TAMPEREEN TEKNILLINEN YLIOPISTO
TAMPERE UNIVERSITY OF TECHNOLOGY

Teemu Hakkarainen

Site-Controlled Epitaxy and Fundamental Properties of InAs Quantum Dot Chains

Julkaisu 1189 • Publication 1189

Tampere 2014

Tampereen teknillinen yliopisto. Julkaisu 1189
Tampere University of Technology. Publication 1189

Teemu Hakkarainen

Site-Controlled Epitaxy and Fundamental Properties of InAs Quantum Dot Chains

Thesis for the degree of Doctor of Science in Technology to be presented with due permission for public examination and criticism in Tietotalo Building, Auditorium TB104, at Tampere University of Technology, on the 25th of January 2014, at 12 noon.

Tampereen teknillinen yliopisto - Tampere University of Technology
Tampere 2014

ISBN 978-952-15-3220-7 (printed)
ISBN 978-952-15-3230-6 (PDF)
ISSN 1459-2045

Abstract

Self-assembled InAs/GaAs quantum dots (QD) are artificial atoms which exhibit extremely high optical and structural quality and enable tailoring of the quantum confinement by adjusting their size, shape, and chemical composition. However, a disadvantage of the self-assembled formation process is that the QDs are randomly located on the GaAs surface. The ability to determine the positions of the QDs at the moment of nucleation, i.e. site-controlled growth, is essential for the new generation of photonic applications including single- and entangled-photon sources and nanophotonic integrated circuits. The purpose of this thesis is to introduce a new nanomaterial system composed of site-controlled InAs quantum dot chains (QDC) grown by molecular beam epitaxy in nanoimprint lithography prepared grooves. A thorough investigation of the structural and optical properties of QDCs is also presented.

The thesis demonstrates that, regardless of the inherent anisotropy of the GaAs(100) surface, QDCs having similar density, size, and emission energy can be grown simultaneously on nanopatterns with different orientations by carefully selecting the growth parameters. However, the in-plane optical polarization of the spontaneous emission from the QDCs depends on their orientation. In more general perspective, this thesis reveals that the nanopattern on which the site-controlled QDs are grown has a strong influence on their morphological properties, including shape, size, strain profile, and composition profile. These properties are strongly cross-correlated and they all influence the electronic and optical characteristics of the QDs. For example, the growth of QDs in the grooves increases their oscillator strength for the vertically polarized spontaneous emission, which is the polarization component that can be coupled to surface plasmons in a metal film. This polarization property accompanied by the possibility of deterministic lateral positioning makes the site-controlled QDCs potential building blocks for plasmonic and nanophotonic waveguides.

Acknowledgments

The work presented in this thesis was carried out at the Optoelectronics Research Centre (ORC) at the Tampere University of Technology during the years 2009–2013. The research was funded by the Academy of Finland, to which I wish to express my gratitude. On a personal level, I would like to thank the Finnish National Graduate School in Materials Physics, Jenny and Antti Wihuri Foundation, Finnish Foundation for Technology Promotion, and Emil Aaltonen Foundation for the financial support they have provided.

At ORC I have had the privilege to work with professionals in various fields of photonics and semiconductor physics and technology. I am deeply indebted to my supervisor, Prof. Mircea Guina, for giving me guidance and support whenever it was needed, but yet letting me find my own path through the doctoral studies. I wish to thank Prof. Emeritus Markus Pessa, the founder of ORC, and Dr. Pekka Savolainen, the current director of ORC, for the opportunity to work and grow in this remarkable environment that encourages students and researchers to learn new skills and strive towards new scientific findings and technological innovations. I express my gratitude to the Development Manager Anne Viherkoski, who has an unrivaled skill to find the way through the jungle of university bureaucracy, and thus making the life of the research staff so much easier. I greatly acknowledge Docent Mihail Dumitrescu, who initiated site-controlled quantum dot related research at ORC, as well as Prof. Tapio Niemi and Dr. Janne Simonen for their expertise in optics and electromagnetism.

The results presented in this thesis are the outcome of an intensive team work. I am especially grateful to my closest colleagues Dr. Andreas Schramm and Dr. Juha Tommila without whom the publications that make this thesis would not exist. I wish to thank Risto Ahorinta and Ville Polojärvi for their world-class AFM and RTA skills, respectively, as well as for their marvelously bad sense of humor that I have had a privilege to enjoy. I am ever grateful to Dr.

Esperanza Luna from PDI Berlin whose TEM work has been in a quintessential role not only in the last two publications but also in the major part of the body of this thesis.

I wish to thank all my current and former MBE colleagues, in particular Dr. Lauri Toikkanen, Dr. Tomi Leinonen, Dr. Jari Lyytikäinen, Dr. Antti Tukiainen, Dr. Soile Suomalainen, Jussi-Pekka Penttinen, Arto Aho, and Ville-Markus Korpijärvi, for their help and companionship. Furthermore, I am thankful to Laboratory Manager Ilkka Hirvonen for his efforts at the construction and maintenance of the infrastructure of the laboratory equipment and to Dr. Antti Härkönen for his valuable help in construction of optical measurement setups.

I thank all the colleagues at ORC, especially those who are unjustly left unacknowledged, for the friendly, familylike working environment, the heart of which is the second floor coffee room.

Finally, wish to express my deepest gratitude to my friends, family, and my girlfriend Mari for their love and support.

Tampere, January 2014
Teemu Hakkarainen

Table of Contents

List of Publications

The following publications are included in this thesis as appendices. In the text they are referred to as [P1]–[P7].

[P1] T. V. Hakkarainen, A. Schramm, A. Tukiainen, R. Ahorinta, L. Toikkanen and M. Guina, "Lateral Ordering of InAs Quantum Dots on Crosshatch Patterned GaInP", *Nanoscale Research Letters,* vol. 5, no. 12, pp. 1892–1896, 2010.

[P2] T. V. Hakkarainen, J. Tommila, A. Schramm, A. Tukiainen, R. Ahorinta, M. Dumitrescu, and M. Guina, " Structural and optical properties of InAs quantum dot chains grown on nanoimprint lithography structured GaAs with different pattern orientations", *Applied Physics Letters*, vol. 97, issue 17, 173107, 2010.

[P3] T. V. Hakkarainen, J. Tommila, A. Schramm, A. Tukiainen, R. Ahorinta, M. Dumitrescu, and M. Guina, "Structural characterization of InAs quantum dot chains grown by molecular beam epitaxy on nanoimprint lithography patterned GaAs(100)", *Nanotechnology* 22, 295604, 2011.

[P4] T. V. Hakkarainen, A. Schramm, J. Tommila, and M. Guina, "The effect of InGaAs strain reducing layer on the optical properties of InAs quantum dot chains grown on patterned GaAs(100)", *Journal of Applied Physics*, vol. 111, issue 1, 014306, 2012.

[P5] T. V. Hakkarainen, V. Polojärvi, A Schramm, J Tommila, and M Guina,"The Influence of Post-growth Annealing on the Optical Properties of InAs Quantum Dot Chains Grown on Pre-patterned GaAs(100)", *Nanotechnology*, vol. 23, 115702, 2012.

[P6] T. V. Hakkarainen, A. Schramm, E. Luna, J. Tommila, M. Guina, "Temperature dependence of photoluminescence for site-controlled InAs/GaAs quantum dot chains", *Journal of Crystal growth*, vol. 378, pp. 470–474, 2013.

[P7] T. V. Hakkarainen, E. Luna, J. Tommila, A. Schramm, and M. Guina, ” Impact of the non-planar morphology of pre-patterned substrates on the structural and electronic properties of embedded site-controlled InAs quantum dots”, *Journal of Applied Physics,* vol. 114, issue 17, 174304, 2013.

Author's Contribution

The work presented in this thesis is essentially teamwork. The author's role in these joint efforts has been the design of the sample structures, epitaxial growth, spectroscopy, and theoretical calculations. A summary of the author's contribution to the research work and to the manuscript preparation is given in the table below. The main aspects provided by the coworkers listed in the publications include nanopatterning, structural characterization, and thermal annealing.

Table 1. Author's contribution to the papers included in the thesis.

Paper #	Contribution to research work	Contribution to writing the paper
P1	Group work (60%)	Main author
P2	Group work (70%)	Main author
P3	Group work (60%)	Main author
P4	Group work (70%)	Main author
P5	Group work (60%)	Main author
P6	Group work (70%)	Main author
P7	Group work (80%)	Main author

List of Abbreviations and Symbols

AlGaAs	Aluminum gallium arsenide
AFM	Atomic force microscopy
CS	Compressive strain
DFTEM	Dark field transmission electron microscopy
EBL	Electron beam lithography
FEM	Finite element method
FIB	Focused ion beam lithography
Ga	Gallium
GaAs	Gallium arsenide
GaInAs	Gallium indium arsenide
GaInP	Gallium indium phosphide
HRTEM	High-resolution transmission electron microscopy
In	Indium
InAs	Indium arsenide
InGaAs	Indium gallium arsenide
LIL	Laser interference lithography
MBE	Molecular beam epitaxy
MD	Misfit dislocation
MOCVD	Metalorganic chemical vapor deposition
NIL	Nanoimprint lithography
ORC	Optoelectronics Research Centre
PL	Photoluminescence
QD	Quantum dot
QDC	Quantum dot chain
RGB	Regrowth buffer

RTA	Rapid thermal annealing
SAQD	Self-assembled quantum dot
SQD	Small quantum dot
SEM	Scanning electron microscopy
SK	Stranski-Krastanov
SRL	Strain-reducing layer
TEM	Transmission electron microscopy
TS	Tensile strain
UHV	Ultra-high vacuum
UV-NIL	Ultraviolet nanoimprint lithography
WL	Wetting layer

Symbols, Greek Alphabet

α	Varshni parameter for temperature dependency of band gap
β	Varshni parameter for temperature dependency of band gap
γ	Surface energy
ΔE	Transition energy
Δ_{so}	Spin-orbit splitting in the absence of strain
ε	Elastic strain
ε_{ii}	Diagonal components of the strain tensor. $i=x,y,z$
ε_{ij}	Off-diagonal components of the strain tensor. $i,j=x,y,z,\ i \neq j$.
$\varepsilon_{\parallel}$	In-plane strain
$\varepsilon_{\perp}$	Out-of-plane strain in reference to natural lattice constant of the material
$\varepsilon_{\perp}^{*}$	Out-of-plane strain in reference to the lattice constant of GaAs
ε_{hydro}	Hydrostatic strain
ε_{shear}	Shear strain
θ	Coverage
θ_c	Critical coverage for quantum dot formation
κ	Surface curvature
μ	Chemical potential

v	Poisson ratio
σ	Stress
Ψ_{e0}	Wave function of electron ground state
Ψ_{h0}	Wave function of hole ground state
Ω	Atomic volume

Symbols, Other

a	Lattice constant
$a_{\parallel}$	In-plane lattice constant
$a_{\perp}$	Out-of-plane lattice constant
a_c	Hydrostatic strain deformation potential for conduction band
a_v	Hydrostatic strain deformation potential for valence band
AR	Aspect ratio
$\mathbf{b}$	Burgers vector
b	Base width
$\mathbf{b}_{\parallel}$	In-plane component of the Burgers vector
$\mathbf{b}_{\perp}$	Out-of-plane component of the Burgers vector
b_t	Tetragonal shear strain deformation potential
c_{ij}	Elastic constant
DOP	Degree of polarization
$\hat{\mathbf{e}}$	Unit direction vector of photon polarization
E_c	Conduction band energy
E_{hh}	Heavy hole band energy
E_{lh}	Light hole band energy
E_{so}	Split-off band energy
E_{e0}	Electron ground state energy
E_{h0}	Hole ground state energy
f	Lattice mismatch
$f_{e0\rightarrow h0}$	Oscillator strength for optical transition between electron and hole ground states
G	Shear modulus

GR	Growth rate
h	Height
h_{MD}	Distance of a dislocation from the surface
I_{TE}	Intensity of in-plane polarized photoluminescence emission
I_{TM}	Intensity of out-of-plane polarized photoluminescence emission
$\vec{\mathbf{p}}$	Momentum operator
$\mathbf{r}$	Position vector
T	Temperature
x, y, and z	Spatial coordinates
x_{In}	Indium compostion
Y	Young's modulus

Chapter 1

1 Introduction

Semiconductor quantum dots (QD), also known as artificial atoms, are nanoclusters that are usually composed of 10^4–10^5 atoms. Although the size of the QDs is some orders of magnitude larger than, for example, the radius of a carbon atom, they are small enough to provide quantum confinement of charge carriers in all three spatial dimensions. This special construction allows tailoring of quantum states of the QDs by adjusting their size, shape, and composition.

The most widely explored type of semiconductor QDs is coherently strained epitaxial QDs. Although the first observation of the strain-driven InAs clustering in the InAs/GaAs material system was observed already in 1985 [1], the pioneering work on these so-called self-assembled QDs (SAQD) was performed in the 90s when it was demonstrated that deposition of a thin layer of InAs on GaAs surface enables a controllable, spontaneous formation of nanoscale islands due to the lattice mismatch between the two materials [2–5]. Since then, extensive materials research has been carried out on this material system. These 20 years of basic research has laid the foundation for a high-quality photonic material system that provides seamless integration to thin film heterostructures devices. Consequently, research groups around the world have presented a large number of QD-based optoelectronics devices including laser diodes, photodetectors, and solar cells [5,6]. Although companies providing QD-based devices exist, the commercial breakthrough of semiconductor QDs is yet to happen. This is largely due to the fact that QDs have not been able to compete with quantum well (QW) heterostructures in the market of traditional optoelectronic devices.

Yet the full benefits of semiconductor QD systems are expected to lead to a new class of devices where they provide unmatched features. This new generation of applications includes, for example, single- and entangled-photon [7] sources, nanophotonic integrated circuits [8], and nanophotonic waveguides [9], as well as photonic crystal lasers having ultra-low lasing threshold [10]. All of these devices rely on the unique excitonic properties of semiconductor QDs. The exploitation of the novel quantum dot based photonic structures in quantum computing and all-optical logics and data transfer are considered as a potential solution for the extension of the Moore's law as well as solving the chip-to-chip interconnect bottleneck, which are the current challenges in silicon-based information technology. However, the practicality of SAQDs is limited because most these emerging applications require a precise positioning of the QD with respect to the cavity, waveguide or other device structure, which has created a demand for the controlled lateral positioning of QDs.

Controlling the positions of semiconductor QDs at the moment of nucleation, also known as site-controlled QD growth, is commonly based on a combination of a nanopatterning technique and epitaxial growth. The nanopatterns are fabricated by lithography-based methods including electron beam lithography (EBL), focused ion beam lithography (FIB), laser interference lithography (LIL), and nanoimprint lithography (NIL). The epitaxial techniques include molecular beam epitaxy (MBE) and metalorganic chemical vapor deposition (MOCVD). So far, the most successful varieties are the MBE growth of QDs on shallow patterned GaAs(100) and the MOCVD growth on GaAs(111)B surface with selectively-etched (111)A-facetted pyramidal pits. Both methods enable fabrication of site-controlled QDs having high optical quality. However, their difference is in the selectivity of the growth. The MOCVD method is extremely selective: growth takes place only inside the pyramidal pit and it is completely terminated once the pit is filled [11]. The MBE method is less selective, but it enables also planar growth which is essential for the device integration.

This thesis focuses on the fabrication of site-controlled QDs by a combination of NIL and MBE. In particular, it presents a simultaneous formation of quantum dot chains (QDCs) having different orientations by MBE growth on NIL prepared nanoscale groove patterns. The purpose of the scientific articles that form this thesis is to present this new nanomaterial system and investigate its structural and electronic properties. The potential applications of the site-controlled QDCs include nanophotonic waveguides [9] and QD-based gain media for

subwavelength plasmonic devices [12,13]. A more general motivation for this thesis is to provide new insight into the site-controlled QD growth process and its influence on the QD properties, which are still far away from being fully understood.

The work presented in this thesis has been conducted in parallel with another branch of QD research currently ongoing at Optoelectronics Research Centre (ORC), which focuses on formation of arrays of single site-controlled InAs QDs [14–17].

This thesis is organized as follows. Chapter 2 introduces the MBE growth process including growth of planar layers and formation of SAQDs. Chapter 3 covers the basic principle of site-controlled QD growth, which is described by presenting three different experimental methods for controlling the nucleation sites of the QDs. Chapter 4 presents the fundamental morphological properties of semiconductor QDs and explores the influence of the nanopatterned growth surface on them. Chapter 4 includes an experimental analysis of QD morphology and strain accompanied with theoretical strain calculations. The morphology of the QD determines its electronic properties which are covered in Chapter 5 presenting quantum mechanical calculations of the electron and hole states in site-controlled QDs. Chapter 6 focuses on the photoluminescence properties, such as emission energy and polarization, of site-controlled QDs and presents two methods for modifying them. The concluding remarks and outlook are combined in Chapter 7.

Chapter 2

2 Molecular Beam Epitaxy of Lattice-Mismatched Materials

Molecular beam epitaxy, invented in the 1960s at the Bell Telephone Laboratories by J.R. Arthur and Alfred Y. Cho, is a method for growing epitaxial metal, insulator and semiconductor thin films. The thin films are grown in ultra-high vacuum (UHV; i.e. a pressure of the residual gas is less than 10^{-9} mbar) chambers on single crystal substrates by a flux of atomic or molecular beams of constituent elements. The semiconductor materials grown by MBE range from elemental silicon (Si) and germanium (Ge) crystals to III-V and II-VI semiconductors, which are stoichiometric compounds of elements from two different groups of the periodic system. The atomic and molecular beams are produced by heating extremely pure elemental materials in effusion cells. The MBE growth process is controlled by adjusting the fluxes and the temperature of the substrate while the relative flux densities of the constituent atoms define the composition of the grown material. In appropriate growth conditions, the atoms or molecules of the beam stick to the surface of the substrate and the newly grown epitaxial film copies the crystal structure of the underlying layer (the substrate). This process is referred to as *epitaxial growth*. Typical growth rates in MBE are 0.5–3 μm/h [18–20].

In the MBE growth process atomic or molecular source materials are physisorbed or chemisorbed on the substrate surface on which they may (i) migrate on energetically favorable lattice cites, (ii) gather at surface contaminations, (iii) form agglomerations of atoms of the same type (e.g. droplet formation), and (iv) migrate on the surface and eventually evaporate

[19]. Typically process (i) is essential for the formation of an epitaxially grown layer, but the energetics of the adatoms on the growth surface depend strongly on the materials and the growth conditions. Consequently, the epitaxial growth of material on a substrate by MBE may proceed by several different modes. The three primary modes are known as Frank-van der Merve, Volmer-Weber, and Stranski-Krastanov. Frank-van der Merve is a pure two-dimensional layer-by-layer growth mode which is usually the most desirable mode for the growth of planar layers. Volmer-Weber is a pure three-dimensional island growth mode that leads to clustering of the deposited material. The third primary growth mode, Stranski-Krastanow, is a three-dimensional mode which initiates as layer-by-layer growth that is followed by subsequent island formation [18]. It should be noted that planar growth of smooth films cannot be obtained by Volmer-Weber and Stranski-Krastanow modes, but they are commonly used for fabrication of QDs and other low-dimensional nanostructures [21]. The samples investigated in [P1–P7] contain planar layers grown by Frank-van der Merve mode and QDs grown by Stranski-Krastanov mode. The principles of these two growth modes will be discussed in detail in the following.

Figure 2.1. MBE grower operating a VG V90 MBE system used in the course of this thesis work. The V90 system is equipped with aluminium, indium, and gallium effusion cells as group III sources and phosphorus and arsenic crackers as group V sources.

2.1 Frank-van der Merve growth of strained layers

If the equilibrium lattice constants of the substrate and the deposited material are equal, the epitaxial grown layer will be lattice-matched with respect to the substrate. In the case of lattice-matched growth, the epitaxial layer will maintain its natural atomic spacing in both vertical and horizontal direction and there is no build-up of elastic strain. This is the case, for example, in homoepitaxial growth of GaAs on a GaAs substrate.

If the equilibrium lattice constant of the epitaxially grown material is smaller or larger than that of the substrate, it is said to be lattice-mismatched. The lattice mismatch is commonly defined as

$$f = \frac{a_0 - a_s}{a_s}, \tag{2.1}$$

where a_0 and a_s are the equilibrium lattice constants of the epitaxially grown layer and the substrate, respectively. Figure 2.2 illustrates the lattice-mismatched growth of Material 2 on a substrate composed of Material 1. Material 2 has a larger lattice constant than Material 1 (i.e. $a_0 > a_s$), but the epitaxially grown layer compresses in the direction of the growth plane in order to copy the lateral lattice spacing of the substrate. This gives rise to in-plane elastic strain defined as

$$\varepsilon_{\parallel} = \frac{a_{\parallel} - a_0}{a_0}, \tag{2.2}$$

where $a_{\parallel}$ is the in-plane lattice constant of the layer. The out-of-plane lattice constant of the epitaxially grown material expands in order to accommodate the misfit. The resulting out-of-plane strain is defined as

$$\varepsilon_{\perp} = \frac{a_{\perp} - a_0}{a_0} = -2\frac{c_{13}}{c_{33}}\varepsilon_{\parallel}, \tag{2.3}$$

where $a_{\perp}$ is the out-of-plane lattice constant of the layer and c_{13} and c_{13} are elastic constants. Material 1 in Figure 2.2 is said to be compressively-strained (CS) because its unit cell has to

compress laterally in order to adapt to the lattice spacing of Material 1, whereas tensile strain (TS) arises when $a_0 < a_s$. This so-called pseudomorphic layer-by-layer growth causes build-up of elastic strain energy with increasing layer thickness. Eventually, at the so-called critical layer thickness, the strain energy is so large that it causes formation of misfit dislocations (MD) at the substrate-layer interface. At this point, the layer is said to be metamorphic. Theoretically, the value of the critical thickness is determined by the lattice mismatch and elastic properties of the particular material system [22], but in practice it is also affected by the growth conditions. Pseudomorphic layer-by-layer growth, followed by plastic strain relaxation and MD formation once the critical layer thickness is exceeded, is the typical growth mode for example for moderately mismatched (*f* around 0 to 2%) compositions of GaInP and InGaAs grown on GaAs [23]. As the mismatch increases the three-dimensional Stranski-Krastanov growth becomes the most energetically favorable process of strain relaxation.

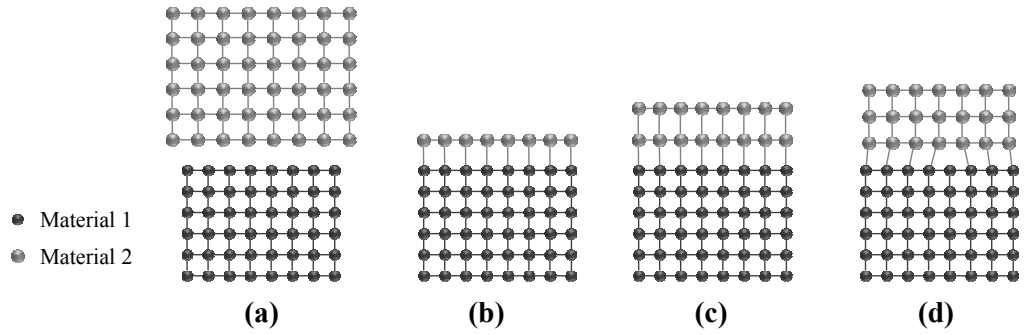

Figure 2.2. Illustration of lattice-mismatched layer-by-layer growth. (a) shows equilibrium crystal structures of Material 1 and Material 2. (b) and (c) represent pseudomorphic growth of Material 2 on Material 1 with the thickness of the epitaxially grown layer approaching the critical value. Finally, in (d) the layer thickness has exceeded the critical value for MD formation and the epilayer has become metamorphic.

2.2 Stranski-Krastanov growth of InAs quantum dots

The pioneering work for the self-assembled formation of coherently strained InAs QDs on GaAs(100), initially observed in 1985 [1], was performed in the mid-1990s [2–4] when it was demonstrated that the 7.2% lattice mismatch of InAs on GaAs enables controllable formation of nanoscale islands by SK growth mode. The principal stages of SK QD formation are illustrated in Figure 2.3. The initial stage is the formation of a two-dimensional wetting layer (WL) shown in Figure 2.3(b). Once the critical value of InAs coverage (θ_c) is exceeded, InAs begins to nucleate as three-dimensional islands [Figure 2.3(c)]. The three-dimensional shape of the islands allows the expansion of the in-plane lattice constant of InAs towards its equilibrium value, which causes distortion to the underlying GaAs crystal. This so-called elastic strain relaxation makes the formation of three-dimensional islands energetically favorable for highly mismatched material systems, such as InAs/GaAs. For the ternary $In_xGa_{1-x}As$ alloy SK QD formation is observed for x>0.3 [24,25]. The critical coverage θ_c for InAs is around 1.6 monolayers (ML). For $In_xGa_{1-x}As$ it increases with decreasing In composition [24].

The formation of self-assembled SK QDs (SAQD) is a statistical process which is sensitive to the InAs growth rate (*GR*), surface temperature (*T*), and the ratio of group V and group III fluxes. These growth parameters determine the migration length of In adatoms on the surface, which along with θ controls the average size and density of the SAQDs. The density of InAs/GaAs SAQDs is in the range from 1×10^8 to 1×10^{11} cm^{-2} and the typical height and base width range from 2 to 12 nm and from 10 to 50 nm, respectively [26]. Direct consequences of the statistical nature of the SAQD growth process are that the resulting QDs are randomly located on the surface and that their sizes vary from dot to dot according to a Gaussian distribution [27]. The shape of InAs SAQDs is approximately a pyramid, which is formed by a combination of steep {111} and {110} facets and/or shallow {135} and {137} facets [28,29]. Figure 2.3(d) shows an atomic force microscope (AFM) image of InAs SAQDs formed by depositing 2.2 ML InAs with a *GR* of 0.05 μm/h at substrate temperature of 515 °C.

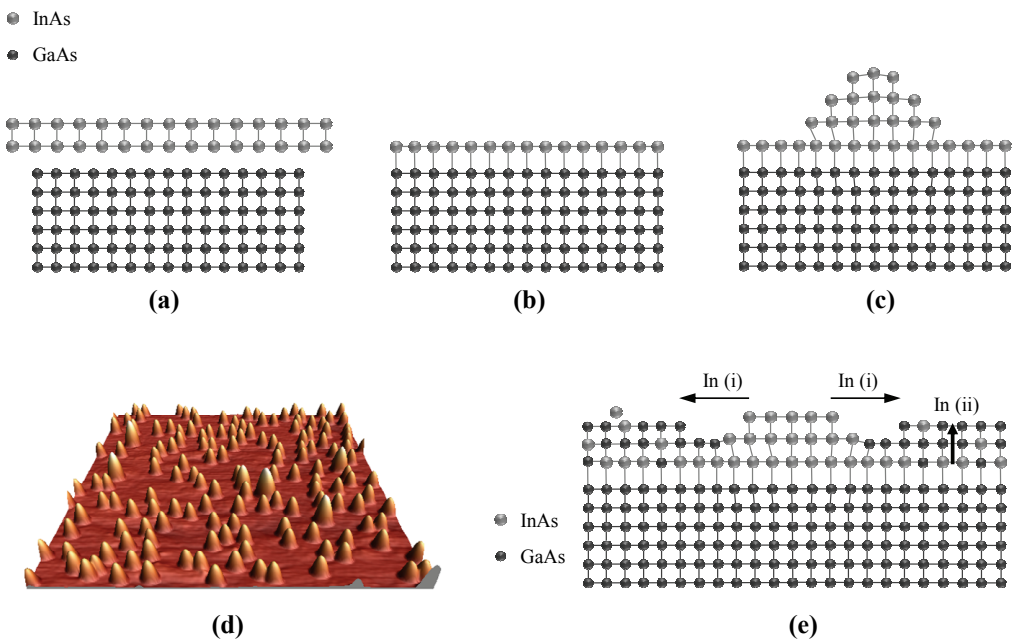

Figure 2.3. InAs Stranski-Krastanov QD formation on GaAs surface. (a) shows the equilibrium crystal structures of InAs and GaAs. SK growth begins by formation of a two-dimensional WL (b). Once the critical thickness for island formation is exceeded InAs accumulates as coherent three-dimensional islands (c). 1×1 μm^2 AFM picture of InAs/GaAs(100) SAQDs having a density of around 1×10^{10} cm^{-2} (d). During overgrowth by GaAs (e), the height of the QD is reduced due to migration of In atoms from the top of the QD to the surrounding GaAs surface (i) and In atoms from the WL segregate to the surface (ii).

Once the InAs SAQDs are formed, they are usually stabilized by capping them with GaAs. Figure 2.3(e) illustrates the early stage of overgrowth of the InAs SAQD by GaAs. The elastically relaxed InAs island is an energetically unfavorable location for GaAs growth due to the lattice mismatch, and thus in the beginning of capping there is no GaAs growth on top of the QD. Before being covered by GaAs layer the QD experiences a strong reduction of its height [30], which depends on the GaAs growth rate and temperature. Already the first few monolayers of overgrown GaAs increase the elastic energy of the QD significantly because the freedom for elastic strain relaxation is reduced. Furthermore, the GaAs layer covering the WL affects the surface energy in the surroundings of the QD. The surface energy of InAs is lower than that of most of the GaAs surfaces, and therefore there is a tendency of In atoms to detach

from the top of the QD and migrate on the newly-formed GaAs surface in order to create a second WL [31]. For the same reason, In atoms from the WL segregate to the GaAs covered surface, which reduces the In composition of the WL. According to the microscopic model for the capping process of InAs SAQDs proposed by Costantini *et al.* based on scanning tunneling microscopy (STM) observations, the reduction of QD height takes place during the deposition of the first 4 MLs of the GaAs layer [32]. They proposed that the detachment of In atoms from the QD is caused by the direct flux of Ga atoms to top of the QD. The QD height is stabilized as the alloy of detached In atoms and the Ga atoms of the capping flux covers the flanks of the QD. Finally, as the overgrowth proceeds, the QD becomes fully covered by GaAs. The increase of elastic energy during GaAs overgrowth as well as the abrupt composition gradient over the QD-GaAs interface gives rise to intermixing of In atoms from the QD with Ga atoms from the surrounding GaAs matrix. The intermixing process may reduce the In composition of the InAs QD significantly and create various different composition gradients depending on the overgrowth conditions and initial morphology of the QD [33–36]. Consequently, many different kinds of QD morphologies can be obtained by adjusting the conditions of InAs deposition and GaAs overgrowth.

Chapter 3

3 Site-controlled Growth of InAs Quantum Dots

An inherent disadvantage self-assembled SK growth is that the QDs are randomly distributed on the substrate. Various methods have been developed to overcome this disadvantage [37], but essentially they are all based on controlling the migration of In adatoms and creating energetically favorable nucleation sites. The adatom migration on a surface with non-uniform properties is driven by local gradients in the chemical potential, which for In can be expressed as [31,38]

$$\mu^{\mathrm{In}}(\mathbf{r}) = \left[\mu_0^{\mathrm{In}} + \frac{Y\varepsilon_{\parallel}^2(\mathbf{r})\Omega}{2} \right] + \gamma\Omega\kappa(\mathbf{r}), \tag{3.1}$$

where μ_0^{In} is the chemical potential of In on a flat, uniform reference surface. The second term is elastic correction to μ_0^{In}, where Y is Young's modulus, $\varepsilon_{\parallel}(\mathbf{r})$ the local in-plane elastic strain, and the Ω atomic volume. The third term is the surface energy contribution to the chemical potential, where γ is the surface energy and $\kappa(\mathbf{r})$ the surface curvature. From Eq. (3.1) we see that the migration of In adatoms on a GaAs surface can be controlled by adjusting $\varepsilon_{\parallel}(\mathbf{r})$, $\kappa(\mathbf{r})$, or γ. Local variations of $\varepsilon_{\parallel}(\mathbf{r})$ can be introduced for example by exploiting the stress field of underlying MDs. A non-zero $\kappa(\mathbf{r})$ can be created by the exploitation of nanopatterning

techniques. Variations of γ can be provided by creating a surface which is composed of different facets. All of the above-mentioned three ways to control the migration of In adatoms, and thus control the nucleation of QDs, are discussed in this chapter using practical examples developed in the thesis work.

3.1 Site-control by stress fields of misfit dislocations

The formation of misfit dislocations is crystal's way to reduce the elastic energy arising from the lattice-mismatch. The MDs are usually formed at the bottom interface of the strained layer [15]. Two main types of dislocations are edge dislocations and screw dislocations. The edge dislocation is either an additional or a missing row of atoms and its Burgers vector (**b**) is perpendicular to the dislocation line direction, while in the screw dislocation **b** is parallel to the dislocation line [39]. The MDs observed in two-dimensionally grown GaInP/GaAs(100) and InGaAs/GaAs(100) materials are typically so-called 60° dislocations that are neither pure edge nor screw dislocations, but rather those of mixed type [40]. The 60° dislocations have **b** in a 60° angle with respect to the dislocation line and in 45° angle with respect to the (100) plane. The magnitude of the Burgers vector for these dislocations is $\|\mathbf{b}\| = a/\sqrt{2}$ [22]. The strain relieving edge component of **b** can be decomposed into parts parallel and perpendicular to the layer-substrate interface: $\mathbf{b}_{edge} = \mathbf{b}_{\|} + \mathbf{b}_{\perp}$. The magnitudes of the in-plane and out-of-plane components of the Burgers vector for a 60° MD are [41]

$$b_{\|} = \pm\frac{\|\mathbf{b}\|}{2} = \pm\frac{a}{2\sqrt{2}} \quad \text{and} \tag{3.2a}$$

$$b_{\perp} = \pm\frac{\|\mathbf{b}\|}{\sqrt{2}} = \pm\frac{a}{2}. \tag{3.2b}$$

The signs of $b_{\|}$ and $b_{\perp}$ depend on the exact orientation of **b**. For a strain relieving MD in CS layer we have negative signs for both $b_{\|}$ and $b_{\perp}$, whereas in the case of TS, the sign of $b_{\|}$ is positive and the sign of $b_{\perp}$ negative. The formation of MDs at the layer-substrate interface induces a stress field that causes local fluctuations of $\varepsilon_{\|}(\mathbf{r})$ on the sample surface. Assuming

an infinitely large crystal, the tangential stress component of a pure edge dislocation lying at the distance h_{MD} below the surface is [42]

$$\sigma_{\mathrm{xx}}^{\mathrm{MD}} = \frac{4G}{\pi(1-\nu)} \times \frac{hx\left(h_{MD} b_{\perp} - x b_{\parallel}\right)}{\left(x^2 + h_{MD}^2\right)^2}, \tag{3.3}$$

where G is the shear modulus, ν is the Poisson's ratio, and x is the lateral distance from the MD. Figure 3.1(a) and (b) show stress fields on the surface 90 nm above MDs formed in TS and CS layers, respectively. The stress field of a MD is a local fluctuation that exhibits positive and negative maxima on the adjacent sides of it. The positive maximum corresponds to a region where $a_{\parallel}$ is larger than further away from the MD. Since InAs has a larger a than GaAs, $\varepsilon_{\parallel}(\mathbf{r})$ for an In adatom is reduced in the area where $\sigma_{\mathrm{xx}}^{\mathrm{MD}}$ is larger than zero. According to Eq. (3.1), this creates a local gradient in $\mu^{\mathrm{In}}(\mathbf{r})$ that causes a preferable nucleation of InAs QDs on the tensile stressed side of the MD. As shown in Figure 3.1(c), the growth of InAs QDs on a MD network, referred to as a cross-hatch pattern, leads to the formation of QDCs oriented along the [011] and [01$\bar{1}$] directions.

In [P1] we investigated the lateral alignment of InAs QDs grown on GaAs covered tensile-strained GaInP (TS-GaInP) and compressively strained GaInP (CS-GaInP). Compressively strained GaInAs (CS-GaInAs) was used as a reference because the ordering of InAs QDs on CS-GaInAs has already been thoroughly studied [43–46]. As shown in [P1] (Figures 2 and 3), there is no difference between CS-GaInP and CS-GaInAs in terms of QD ordering, which is observed as a preferable nucleation of QDs on the MDs as multi-QD wide rows. However, QDs grown on TS-GaInP formed single-dot wide chains. The explanation for the difference between the TS and CS layers lies in the surface morphology. The stress field of the MD not only affects the QD nucleation but also causes local variations of growth rate during the two-dimensional growth of the strained layers and GaAs cap layer. In case of CS-GaInP and CS-GaInAs, this results in a ridge-valley morphology; the ridge is located on the tensile-stressed and the valley on the compressively-stressed side of the MD as shown in Figure 3.1(a). In the sample with TS-GaInP, the valley is located on the tensile-stressed side of the MD [Figure 3.1(a)]. The surface curvature of the ridge-valley morphology gives an additional contribution to the QD formation. In this respect, the groove is a preferable nucleation site for the InAs QDs. In the sample with

TS-GaInP the surface curvature and stress field direct the migration of In adatoms on the same side of the MD, which results in a strong ordering of QDs. In the CS-GaInP and CS-GaInAs samples, on the other hand, the influences of the stress field and the surface curvature are counteracting each other, which weakens the QD ordering effect of the cross-hatch pattern.

While InAs QD growth on the cross-hatch patterned TS-GaInP enables the formation of well-defined QDCs, this technique has two major disadvantages. There is a lot of additional QD nucleation in between the MDs, which might be possible to avoid or at least minimize by fine tuning the growth conditions as well as the thickness and composition of the GaInP layer. However, more severe limitation is that, although the QDs arrange on the MDs, the MDs themselves are randomly located. Therefore, this method does not directly enable the control of the positions of the QDCs on the sample.

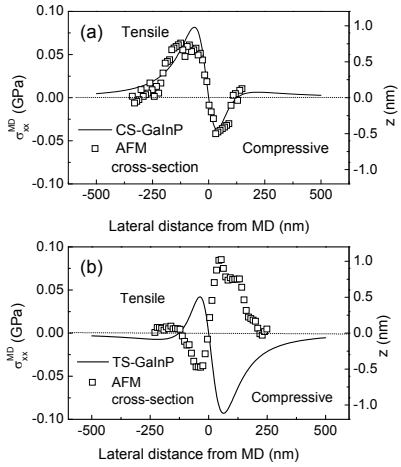

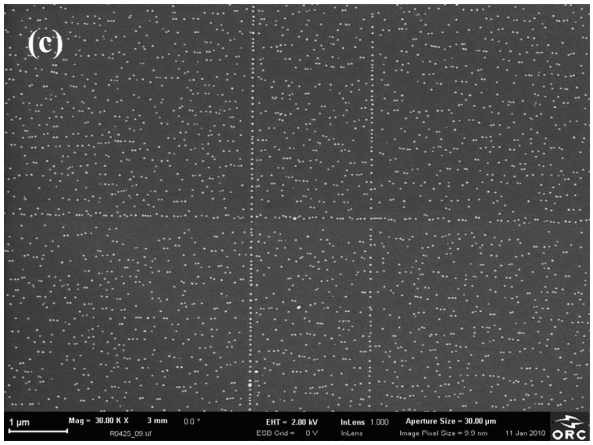

Figure 3.1. The stress field induced by a MD formed in a CS layer (a) and in a TS layer (b) presented by the solid curves. The dotted curves in (a) and (b) are AFM cross-sections of the sample surface above the dislocation. The SEM picture in (c) shows InAs QDs grown on a 60 nm TS GaInP layer covered by a 30 nm GaAs layer.

3.2 Site-control by substrate patterning

A widely used method for obtaining QD nucleation precisely on predetermined locations is to create local variations of $\kappa(\mathbf{r})$ in Eq. (3.1) by nanopatterning the GaAs surface [47–50]. On such nanopatterned surface the net migration of adatoms to the bottom of the pits or grooves, or other recesses is driven by the curvature-induced capillarity [51]. In the microscopic view the driving force for the nucleation of InAs QDs in the recesses can be understood as a preferential accumulation of In adatoms at the step edges [52] or local inhibition of adatom migration due to the high step density in the recess. It has been also proposed that $\kappa(\mathbf{r})$ of the recess causes a change in surface strain which gives rise to a local reduction of critical coverage θ_c [53]. Figure 3.2(a)–(c) shows the basic steps of the regrowth process on a nanopatterned GaAs surface. Typically, the patterned surface is first covered by a thin GaAs regrowth buffer (RGB) in order to bury the patterning process related impurities and to smoothen the surface. The surface morphology after the RGB growth is illustrated in Figure 3.2(b). InAs deposition on the RGB results in (i) formation of a WL that covers the corrugated surface and (ii) nucleation of QDs in the recesses. Therefore, these QDs are essentially SK-QDs formed in pre-determined locations, and thus this growth method is commonly referred to as site-controlled SK growth.

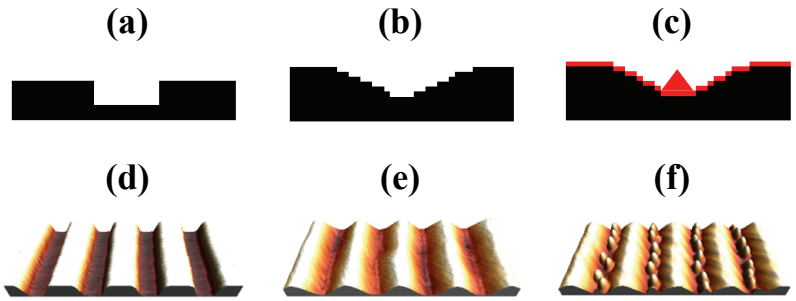

Figure 3.2. Schematic illustration of QD growth on patterned surface. (a) nanopatterned GaAs surface, (b) GaAs surface covered by a GaAs buffer, (c) InAs WL and QDs grown on the buffer. AFM pictures in (d)–(f) illustrate steps (a)–(c), respectively, for InAs QDCs grown on NIL patterned grooves. Initial depth, width, and period of the grooves are 30 nm, 90 nm, and 180 nm, respectively.

The predetermined QD nucleation sites can be defined by several lithography techniques, including oxidization by atomic force microscopy [47], focused ion beam lithography [54], and especially electron beam lithography [48,49,55,56]. In [P2–P7] we have fabricated site-controlled InAs QDCs by UV-NIL, which has been demonstrated to be an effective tool for the positioning of single InAs QDs [14–17]. The basic steps of GaAs patterning by UV-NIL are described in the following.

3.2.1 Substrate patterning using nanoimprint lithography

Nanoimprint lithography (NIL) is a nanofabrication method based on mechanical replication of a surface structure from a master template onto the sample. At ORC, the NIL process has been applied in several applications in addition to site-controlled QD growth. These include e.g. fabrication of metal nanocones [57], periodic gratings of distributed feedback lasers [58], and moth-eye antireflection coatings for photovoltaics [59].

The groove patterns used for the MBE growth of the QDC samples studied in [P2–P7] is a soft ultraviolet nanoimprint lithography (UV-NIL) process consisting of the seven steps described below and illustrated in Figure 3.3.

1. Fabrication of the desired nanopattern on the silicon master by laser interference lithography.
2. Pressing a glass composite on the master spin coated with OrmoStamp resist (Micro resist technology GmbH, Germany) followed by hardening the resist with UV light.
3. Removal of the glass composite from the master with the hardened resist now attached to it. The glass composite with the hardened resist on it forms the stamp that is a negative of the master pattern.
4. Spin coating mr-UVCur06 UV-NIL resist (Micro Resist Technology GmbH) on the template, which is a GaAs/AlGaAs/GaAs layer structure grown by MBE on a GaAs wafer. Details of the template are presented in [P2].
5. Pressing the stamp on the template and curing the resist with UV light.
6. Removal of the stamp from the template followed by removal of the residual layer.
7. Transferring the pattern to the template by BCl_3/Ar chemistry and inductively coupled plasma reactive ion etching based etching.

The glass composite used in the NIL stamp is composed of three functional layers bonded to a thick carrier glass: a silicone cushion layer which distributes the imprint pressure and adapts to the shape of the sample; a thin glass (thickness 50–150 μm) layer, which is attached to the silicone layer, and prevents the lateral deformation of the pattern during the imprint; and the patterned OrmoStamp resist layer, which has inverted nanostructure on the surface. A fluorine containing molecule layer was used as an anti-adhesive in the UV-NIL process [60].

The NIL patterned GaAs wafers used in this thesis for the growth of site-controlled QDCs had four 10 mm × 10 mm areas with [011]-, [01$\bar{1}$]-, [010]-, and [001]-oriented grooves and a planar reference area in the middle of them. The grooves on each area were 30 nm deep, 90 nm wide, and they had a period of 180 nm.

Before the patterned wafers were loaded into the MBE chamber for QD growth, they went through a chemical cleaning and oxide removal process. This process was a chemical treatment including an isopropyl alcohol (IPA) rinse before and after a chemical etch consisting of solutions of HCl, IPA and NH_4OH [14].

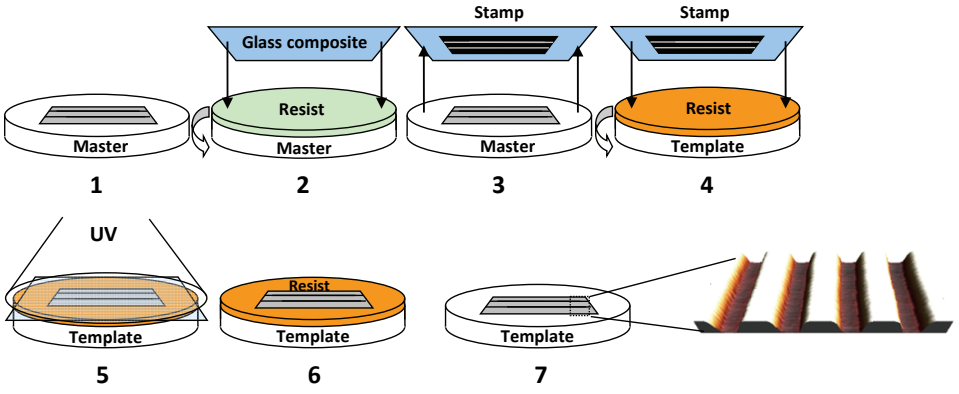

Figure 3.3. Basic steps of UV-NIL process for fabrication of groove patterns on GaAs surface of the template wafer.

3.2.2 Fabrication of the regrowth buffer

After the NIL process and chemical cleaning the groove patterned sample was instantly transferred into the MBE system. A standard degassing at 300°C was first performed in the preparation chamber in order to evaporate water molecules from the sample surface. Then the sample was transferred to the growth chamber for thermal oxide removal carried out in As_2 flux at 590°C. After the heat treatment the surface of the patterned sample was clean and free of oxide, and thus it was ready to be overgrown with GaAs. The GaAs RGB was grown at a relatively low temperature of 490 °C in order to avoid too rapid planarization of the patterned surface. The growth rate was 0.6 μm/h.

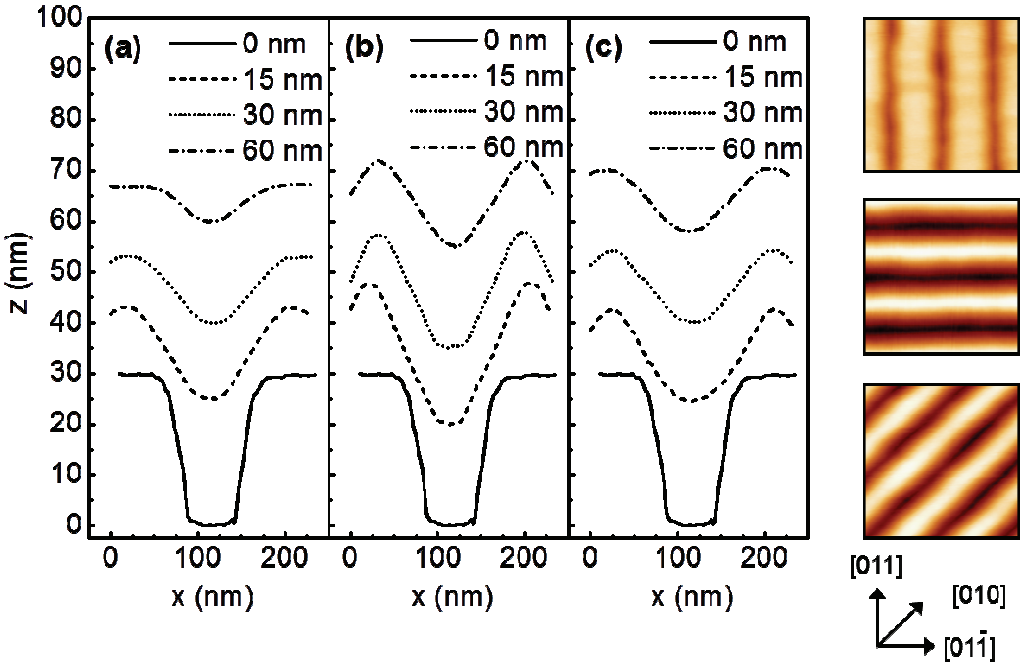

Figure 3.4. AFM cross-sections of grooves patterns before regrowth and after the growth of GaAs RGBs with different thicknesses. (a)–(c) presents [011]-, [01$\bar{1}$]-, and [010]-oriented grooves respectively. The AFM pictures on the right side of the graph show the [011]-, [01$\bar{1}$]-, and [010]-oriented grooves after the growth of 60 nm RGB.

Figure 3.4 shows AFM cross-sections of [011]-, [01$\bar{1}$]-, and [010]-oriented grooves before regrowth and after the growth of 15 nm, 30 nm, and 60 nm thick RGBs. The [001]-oriented grooves will be omitted from the discussion from now on since they are crystallographically symmetric to the [010]-oriented grooves. As shown in Figure 3.4, the groove depths decrease with increasing RGB thickness due to the directed migration of Ga adatoms to the bottom of the grooves, which is again driven by the surface curvature term in Eq. (3.1). The spontaneous planarization of the patterned surface in GaAs overgrowth sets the upper limit for the RGB thickness. It is also evident from Figure 3.4 that the planarization rate depends on the groove orientation in the following relation.

$$[01\bar{1}] < [010] < [011]. \tag{3.4}$$

The origin for the orientation dependency of the growth rate at the bottom of the groove arises from the anisotropies of Ga adatom migration and step attachment. The predominant migration direction of the Ga adatoms is along the [01$\bar{1}$] direction [61]. Therefore, ridge-to-groove migration of the Ga is strong for the [011]-oriented and weak for the [01$\bar{1}$]-oriented pattern, while the [010]-oriented pattern is an intermediate case. The second contribution to the anisotropic planarization of the grooves arises from the nature of the atomic steps that form the groove structure. The steps in the [011]-oriented grooves are As-terminated B-type steps which are more favorable locations for Ga adatom attachment than the Ga-terminated A-type steps found in the [01$\bar{1}$]-oriented pattern [62,63].

It should be noted that the groove structure may also be composed of crystallographic facets rather than stepped [100] surface. Generally, the Ga-terminated (n11)A are more stable than the As-terminated (n11)B facets because of the lower surface energy [64]. This leads to some degree of A-type facet preservation during GaAs overgrowth, which hinders the planarization of the [01$\bar{1}$]-oriented grooves. A thorough facet analysis for different groove orientations is presented in [P3].

3.2.3 Quantum dot growth on groove patterns

The growth of the GaAs RGB was followed by a subsequent formation of QDCs by deposition of InAs. It was estimated that obtaining dense QDCs at the bottom of each groove requires less

than 40 nm centre-to-centre separation between the neighboring QDs along the chain. This translates into a QD density of 1.5×10^{10} cm^{-2} for 180 nm groove separation. Based on a series of samples with SAQDs grown on planar GaAs, such QD density can be obtained by deposition of 2.2 ML of InAs 0.05 μm/h growth rate at the temperature of 515 °C which was used as a starting point for QDC growth parameter optimization. The influence of the growth temperature on the formation of InAs QDs on grooves with different orientations is shown in Figure 3.5. At the lowest temperature of 505 °C we observe a high density of small QDs which are scattered in grooves. As the growth temperature is elevated to 515 °C, the QD density is reduced and the

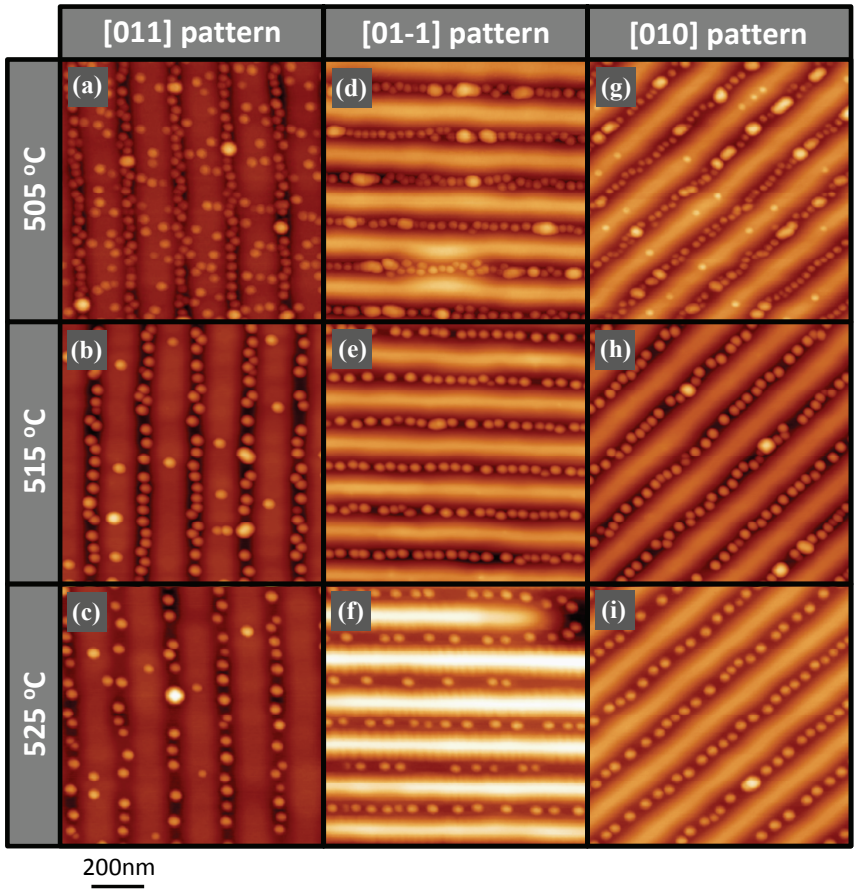

Figure 3.5. AFM pictures of InAs QDCs grown at different temperatures. In (a)–(c), [011]-oriented QDCs, in (d)–(f) $[01\bar{1}]$-oriented, and in (g)-(i) [010]-oriented QDCs. The height scale in (a)–(i) is 35 nm.

QD size increased. Finally at the highest temperature of 525 °C, the QDs get even larger and the density is not high enough to completely fill the grooves. The QD ordering and QD densities for different QDC growth temperatures and RGB thicknesses are presented in [P3]. It is worth pointing out that only the RGB thickness of 60 nm and the QDC growth temperature of 515 °C resulted in similar QD densities for each pattern orientation. With the other sets of growth parameters the QD density depends on the pattern orientation due to a combined effect of the pattern anisotropy and anisotropic In adatom migration [65].

3.3 Site-control by facet-dependent surface energy

The exploitation of strain and surface curvature for the lateral ordering of InAs QDs was discussed in the previous sections. According to Eq. (3.1), the third parameter that influences the migration of In adatoms on the GaAs surface is the surface energy γ. Since the net migration of In adatoms is towards lower chemical potential, the InAs QDs nucleate preferentially on crystal facets with low γ.

In this thesis the influence of γ on QD nucleation was observed on the sidewalls of the $[01\bar{1}]$-oriented grooves as reported [P3, P6]. Figure 3.6(a)–(c) show surface morphologies of samples with 2.2 ML InAs deposited on 15 nm, 30 nm, and 60 nm thick RGBs, respectively. The groove sidewalls of the sample with 15 nm RGB are decorated with a periodic ripple, which is reduced as the RGB thickness is increased to 30 nm and nearly vanished by further increase to 60 nm. The ripple was identified as a chain of small QDs (SQD) by cross-sectional dark field transmission electron microscopy (DFTEM).

The reason for the formation of the SQDs on the sidewalls of the $[01\bar{1}]$-oriented grooves lies in the presence of the (411)A facets which have a surface energy comparable to low index GaAs surfaces [66]. As shown in Figure 3.6(e), the facet angle distribution of these grooves is dominated by the (411)A facets for the RGB thicknesses of 15 nm and 30 nm. As the RGB thickness is increased to 60 nm, (611)A facets become predominant. GaAs(611)A is most probably an unstable high-energy facet since it has not been reported elsewhere. This explains why the SQDs are nearly non-existent on the sample with RGB thickness of 60 nm. The influence of the SQDs on the carrier dynamics of the QDCs is discussed in [P6].

In summary, we used stress fields of misfit dislocations for the lateral ordering of InAs QDs in P[1]. The influence of facet-dependent surface energy on QD formation was observed in [P3] and its effect on photoluminescence was studied in [P6]. However, the primary method for controlling the nucleation sites of QDs in this thesis is the local surface curvature provided by the patterned substrate, which enabled formation of site-controlled QDCs investigated in [P2–P7]. The next chapter focuses on the influence of the non-planar growth surface on the structural properties of InAs quantum dots.

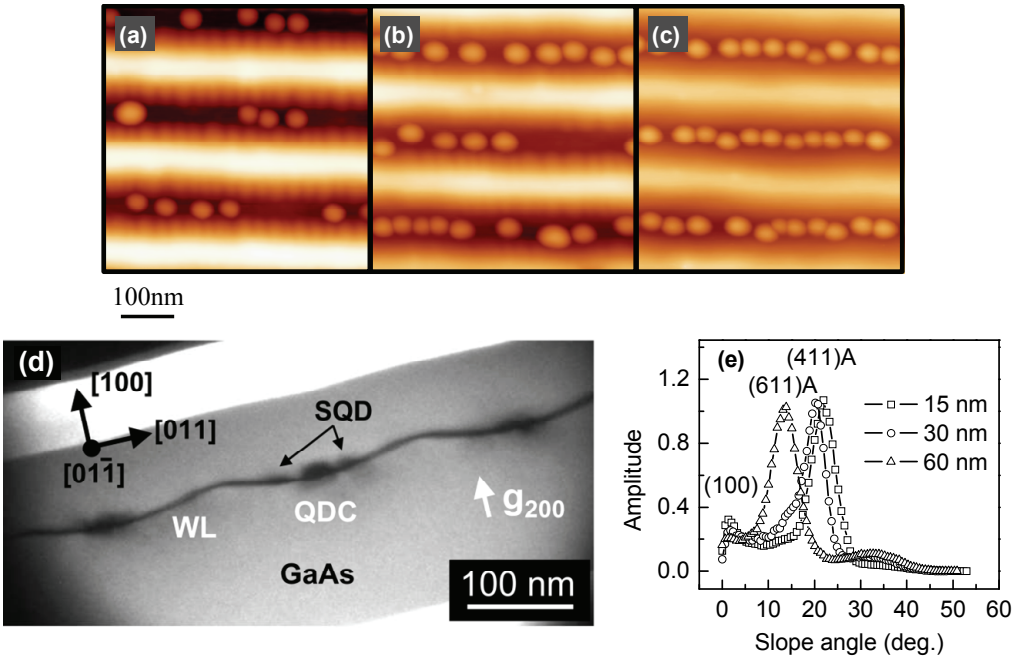

Figure 3.6. Formation of SQDs on the sidewalls of the [01$\bar{1}$]-oriented grooves. AFM pictures in (a)–(c) show the QDCs and pattern morphology for RGB thicknesses of 15 nm, 30 nm, and 60 nm, respectively. The cross-sectional DFTEM micrograph in (e) illustrates WL, QDCs, and SQDs after capping with GaAs. The slope angle graph in (d) shows the facets observed in the grooves shown in (a)–(c).

Chapter 4

4 Structural Properties of InAs Quantum Dots Grown in Grooves

As discussed in the previous chapter, the accumulation of indium adatoms on the lithographically defined locations is driven by local gradients in the surface chemical potential arising from the surface curvature. However, the patterned surface may also influence the shape, composition, and elastic strain fields of the QD, which determine its electronic structure. The influences of the growth on the groove pattern on the structural properties of InAs quantum dots are discussed in this chapter, which is based on the work presented in [P7]. Since the QD morphology is heavily changed during the GaAs overgrowth, the focus of the structural investigation was on QDs embedded in a GaAs matrix. The structural investigation was mostly limited to QDs grown in $[01\bar{1}]$ oriented grooves (sample QD1). SAQDs grown in identical conditions on a planar surface (sample QD2) were used as a reference structure.

4.1 Morphology

The influence of the pattern on the morphology of the embedded QDs was investigated by means of a statistical DFTEM analysis. The DFTEM micrographs were taken using two-beam **g**=(200) imaging conditions. Since $\mathbf{g}_{200}$ DFTEM is sensitive to the chemical composition for semiconductors with zinc blende structure, it provides a reliable determination of the QDs dimensions and morphology [67,68].

A truncated pyramidal QD shape with a slight elongation along the [01 $\bar{1}$] direction was observed both for QD1 [Figure 4.1(b)] and QD2 [Figure 4.1(c)]. A truncated pyramidal cross-section can be associated to several different three-dimensional QD shapes, such as truncated pyramids with square bases oriented along either <001> [69–71] or <011> directions [70,72]. The <001> and <011> oriented pyramids are composed of {110} and {111} facetted sidewalls, respectively. There are also several reports of truncated pyramids with octagonal bases [73–75], which are composed of a combination of {110} and {111} facets. A detailed evaluation of about 40 QDs per sample indicated that the QDs in both QD1 and QD2 are truncated pyramids bound by (100) top facets and inclined side facets. The existence of both {110} and {111} side facets was observed in both samples, but a statistical evaluation of the facet angles revealed that the steeper {111} planes are the predominant facets in QD1, while shallower {110} planes are the predominant facets in QD2.

The DFTEM micrographs reveal also other differences in the morphology of QD1 and QD2. While QD2 [Figure 4.1(c)] has a flat bottom, we found that the shape of the groove determines the shape of the lower part of QD1 [Figure 4.1(a)]. In particular, we observed that the bottom of QD1 replicates the groove morphology, i.e., it is flat only in a reduced area at the centre and curves on the sides towards the groove sidewalls. Furthermore, it is obvious from Figure 4.1 that the QDs grown in the grooves are taller than the QDs grown on the planar surface. In order to investigate the QD size in both samples more thoroughly, we performed a statistical analysis of the QD height h, base width b, and aspect ratio $AR = h/b$. The average QD dimensions and their standard deviations were determined after analyzing more than 40 QDs per sample from DFTEM micrographs with [011] zone axis. As a result, we obtained h=8.3 nm±1.0 nm, b=29.0 nm±3.0 nm, and AR=0.29±0.4 for QD1 and h=5.5 nm±0.6 nm, b=28.1 nm±3.1 nm, and AR=0.20±0.3 for QD2. As these values indicate, AR is significantly larger for QD1 than for QD2 and the difference originates predominantly from the difference in the QD height. Since the height of the QDs before capping was found to be the same (12 nm) for both QD1 and QD2, the difference of the aspect ratios between the QDs grown on the nanopattern and on the planar surface seems to appear during the capping process.

Similar, although not so comprehensive, DFTEM analysis was performed also for the QDs formed in the [011]-, and [010]-oriented grooves, for which the average values of b, h, and AR

were similar to those of QD1. Furthermore, they exhibited elongation along the [01 $\bar{1}$] direction as well as {111} planes as predominant facets similarly to QD1.

Figure 4.1(d) and (e) illustrate the QD and WL geometries of QD1 and QD2, respectively, constructed based on the DFTEM statistics. It should be noted that the value of *b* was determined for both QD1 and QD2 from DFTEM micrographs taken along the [011] zone axis. Consequently, *b* is the side of the square base of QD1, while for QD2 it is the diagonal of the base. Although the $\mathbf{g}_{200}$ DFTEM micrographs contain information about the chemical composition, they cannot be directly used for the determination of the In content of the QDs due to elastic relaxation as well as experimental uncertainties related to location of the QD in the TEM foil.

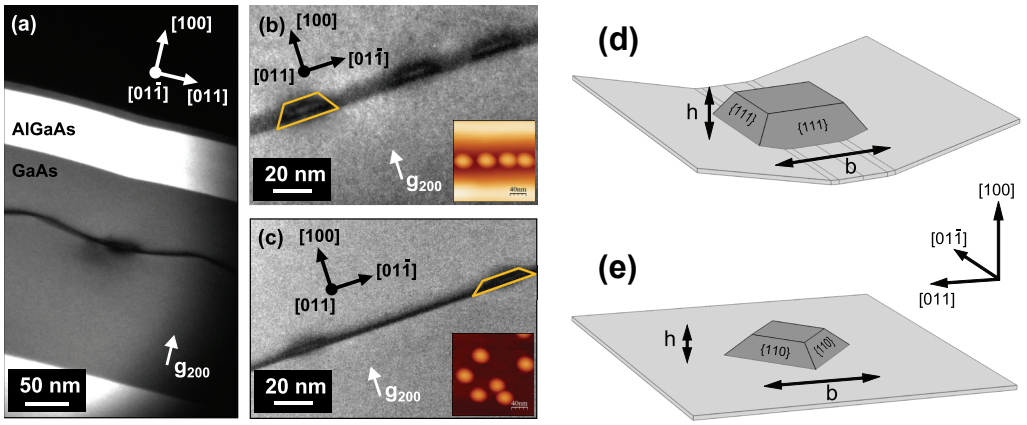

Figure 4.1. Chemically sensitive cross-sectional $\mathbf{g}_{200}$ DFTEM micrographs. In (a) and (b) QD1 is viewed along the [01 $\bar{1}$] and [011] zone axes, respectively. (c) shows QD2 viewed along the [011] zone axis. The insets in (b) and (c) show AFM pictures of QD1 and QD2 before capping. (d) and (e) show schematic illustrations of the QD and WL geometries for QD1 and QD2, respectively, as determined from the DFTEM statistics. The GaAs matrix has been excluded from (d) and (e) for the sake of clarity.

4.2 Elastic strain

The elastic strain in a QD arises from the lattice mismatch between the matrix and the QD materials, which in case of InAs QDs is determined by the actual In content of the QD after embedding. The strain in a QD is partly relieved by elastic strain relaxation, which depends on the shape of the QD. In [P7] we utilized an experimental high-resolution TEM (HRTEM) based strain analysis in conjunction with finite element method (FEM) calculations in order to determine the influence of the growth on groove pattern on the strain and In composition of InAs QDs. The most important findings of that analysis are presented in the following.

4.2.1 Experimental strain analysis

The HRTEM micrographs shown in Figure 4.2(a) and (c) reveal that both QD1 and QD2 grow coherently strained on top of the GaAs prepatterned and planar surfaces, respectively. The coherent strain in the InAs QDs produces a tetragonal distortion of the cubic unit cells that can directly be assessed from the HRTEM images. We use the LADIA program package [76] to evaluate the strain distribution. The tetragonal lattice distortion of the layer is the derivative of the displacement between the atomic positions and the reference lattice, which in our case was the GaAs matrix [77]. Figure 4.2(b) and (d) display the out-of-plane ($\varepsilon_{zz}^{*} = \varepsilon_{\perp}^{*}$) strain distributions in QD1 and in QD2, derived from the HRTEM micrographs in Fig. 4(a) and (c), respectively. Symbol "*" in $\varepsilon_{\perp}^{*}$ indicates that the strain is measured in reference to the lattice constant of the GaAs matrix, not in reference to the natural unstrained lattice constant of the QD material as in Eq. (2.3). The out-of-plane strain is given by

$$\varepsilon_{\perp}^{*} = \frac{a_{\perp} - a_{GaAs}}{a_{GaAs}} \tag{4.1}$$

where $a_{\perp}$ is the out-of-plane lattice constant and a_{GaAs} is the GaAs lattice constant. The strain maps in Figure 4.2 evidence not only the morphological differences between QD1 and QD2 (in particular, the different *h* and *AR*) but also reveal the significant differences in their strain distributions. In QD2, grown on the planar surface, the maximum $\varepsilon_{\perp}^{*}$ localizes at the centre of the QD with $\varepsilon_{\perp}^{*}$ (max) around 12.2%. These features are in agreement with previous works on the strain field of InAs SAQDs [78,79]. On the other hand, unlike QD2, the maximum strain at

QD1 localizes at the very top part of the QD and amounts for a lower value of about 10.7%. The examination of QD1 along both [01 $\bar{1}$] and [011] zone axes yields the same result and, in particular, it confirms this specific strain distribution where the maximum strain value localizes at the upper part of the QD.

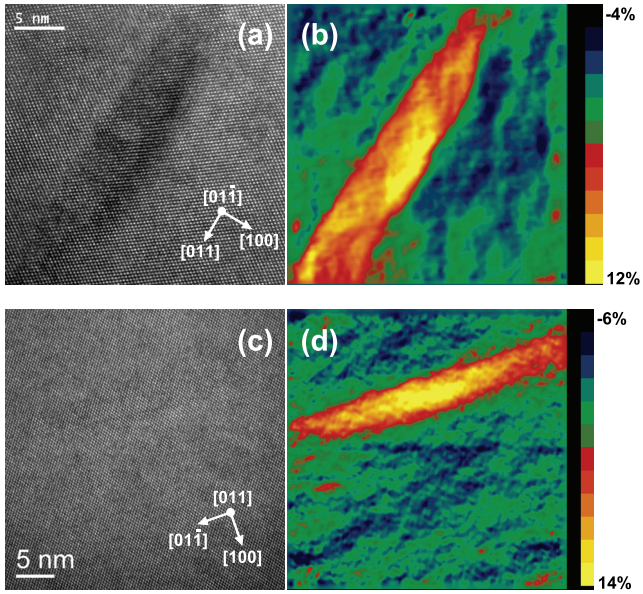

Figure 4.2. HRTEM images of QD1 (a) and QD2 (c). (b) and (d) display the out-of-plane strain $\varepsilon_{\perp}^{*}$ maps obtained from the HRTEM images in (a) and (c), respectively, after the analysis with the LADIA software.

4.2.2 Strain model

Further insight into the elastic strain in structures QD1 and QD2 was obtained from three-dimensional continuum mechanical strain calculations. The QD-WL geometries for QD1 [Figure 4.1(d)] and QD2 [Figure 4.1(e)] for the strain model were constructed based on the DFTEM data and AFM cross-sections of the groove. The lattice mismatch was incorporated in the model by pseudo-thermal expansion [80] and the elastic strain in the QDs was solved by minimization of elastic energy by FEM [81]. The details of the strain model are described in [P7].

Figure 4.3(a) and (b) present 2D cross-sections of $\varepsilon_{\perp}^{*}$ for QD1 and QD2, respectively, calculated assuming that the QDs are consisting of pure InAs. The elastic strain relaxation is most pronounced in the upper corners of both QD1 and QD2 as well as in the curved bottom of QD1. Both QD1 and QD2 exhibit an area of uniform high $\varepsilon_{\perp}^{*}$ value in the middle section of the QD. The maximum values of $\varepsilon_{\perp}^{*}$ in QD1 [Figure 4.3(a)] and QD2 [Figure 4.3(b)] are 10.9% and 11.7%, respectively. These values are in remarkable agreement with the data extracted from the experimental strain maps shown in Figure 4.2(b) and (d). However, the simulation performed assuming a uniform InAs composition [Figure 4.3(a)] does not reproduce the low value of $\varepsilon_{\perp}^{*}$ observed in the bottom part of QD1 [Figure 4.2(b)]. Therefore, the model was refined by introducing a more realistic composition profile for QD1.

Since the experimentally observed strain profile in QD1 in Figure 4.2(b) strongly resembles observations on $In_{0.5}Ga_{0.5}As/GaAs$ QDs where an inverse-cone type composition profile was proposed [79,82], a graded In composition (x_{In}) profile of the inverse-cone type was introduced in the strain calculations, as illustrated in Figure 4.3(c) and (d) for QD1 and QD2, respectively. The graded composition profiles have pure InAs material along the line that runs vertically through the centre of the QD and an inverse-cone type gradient towards the bottom corners where the In composition x_{In} is approximately 0.5.

Figure 4.3(e) and (f) show the simulated $\varepsilon_{\perp}^{*}$ distribution maps for QD1 and QD2 obtained from strain simulations assuming the inverse-cone type x_{In} profiles. The introduction of the graded composition profile for QD1 [Figure 4.3(e)] yields to an excellent agreement both qualitatively and quantitatively between the predicted and the experimental strain maps [Figure 4.2(b)]: the model predicts a maximum $\varepsilon_{\perp}^{*}$ value of about 10.1% in the upper part of the QD, whereas $\varepsilon_{\perp}^{*}$ reduces towards the bottom of QD1. Regarding QD2, as shown in Figure 4.3(f), the graded composition profile produces a vertical strain gradient which, however, is not observed in the experimental strain maps [Figure 4.2(b)]. In this case, the uniform In composition model [Figure 4.3 (b)] yields a better agreement with the experimental strain distribution.

An advantage of solving the complete strain tensor is that we can investigate also the magnitude of other strain components, such as (i) the shear strain $\varepsilon_{shear} = \varepsilon_{zz} - 0.5\times(\varepsilon_{xx}+\varepsilon_{yy})$ that gives rise to

the splitting of the heavy and light hole valence bands and (ii) the hydrostatic strain $\varepsilon_{hydro}=\varepsilon_{xx}+\varepsilon_{yy}+\varepsilon_{zz}$ that changes the energy separation between the conduction and valence bands [83,84]. It should be noted here that the strain components ε_{xx}, ε_{yy}, *and* ε_{zz} are calculated with respect to the equilibrium lattice constant of the QD material, as in Eq. (2.2).

Shear strain distributions for QD1 calculated using uniform and inverse-cone type x_{In} distributions as well as for QD2 composed of pure InAs are presented in [P3] (Figures 7 and 9). The most important finding from the comparison of ε_{shear} distributions of QD1 and QD2 is that the curved geometry of the lower part of QD1 provides additional strain relaxation along the [011] direction, which is observed as an hourglass shape in the ε_{shear} map. This contribution arises from the influence of the groove where QD1 is located and it gives rise to a lateral anisotropy of ε_{shear} in QD1. The influence of this anisotropy on the hole confinement will be discussed in the following chapter.

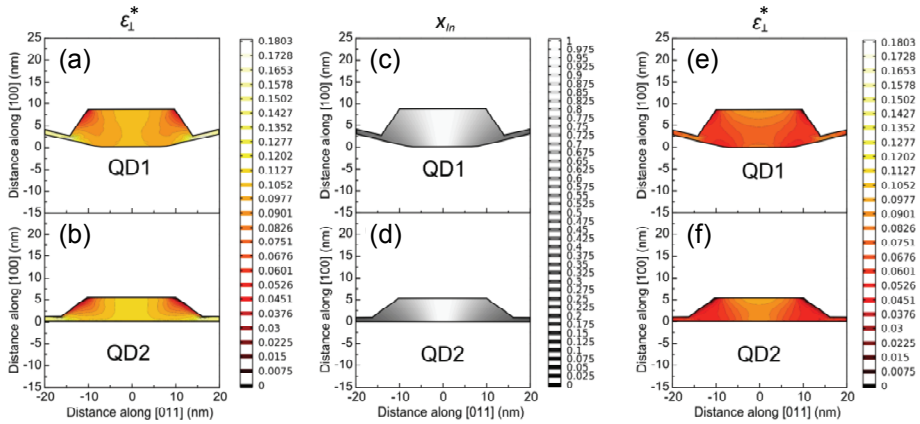

Figure 4.3. 2D cross-sectional maps of the out-of-plane strain component $\varepsilon_{\perp}^{*}$ for QD1 (a) and QD2 (b) with uniform In compositions. Inverse-cone type graded In composition profiles (x_{In}) for QD1 (c) and QD2 (d).). The out-of-plane strain $\varepsilon_{\perp}^{*}$ distributions for QD1 (e) and QD2 (f) are obtained from FEM simulations using the x_{In} distributions in (c) and (d), respectively. The cross-sections in (a)–(f) are taken along the centre of the QD.

In P[3] we also investigated the influence of the morphological differences between QD1 and QD2 on their hydrostatic strain. We found out that the maximum value of ε_{hydro} in QD1 is 9.0%, while in QD2 it is 8.0%. By analyzing the results of several simulations we came to the

conclusion that 80% of this difference arises from the difference in the *AR* and 20% from the curvature of the bottom of QD1. The influence of ε_{hydro} on the bandgaps of QD1 and QD2 will be discussed in the following chapter.

4.2.3 Evolution of strain during capping process

As discussed above, the QDs nucleated in the grooves experience less height reduction during the capping process than SAQDs grown on a planar surface. Furthermore, they exhibit an inverse-cone type composition profile while the SAQDs have a uniform composition. As the height of the embedded InAs QDs is determined by the early stage of the capping process, additional simulations were performed in order to determine the evolution of strain in QD1 during GaAs capping. QD2 was again used as a reference. The results are presented in Figure 4.4, which shows that the elastic strain energy in QD1 is smaller than in QD2 for GaAs cap thicknesses below 10 nm. The heights of QD1 and QD2 were assumed to be 8.3 nm and 5.5 nm, respectively during the whole capping process. This is not exactly correct since for 0 nm cap thickness the height of both QD1 and QD2 should be 12 nm, as obtained from AFM analysis of uncapped QDs [P7]. However, as shown in the inset of Figure 4.4, the truncation factor of a pyramidal QD (i.e. height) does not determine the value of elastic strain energy in the beginning of the capping process, because at this point the strain energy is condensed into the bottom of the QD which is in contact with the GaAs surface below. It should be noted that the interface area between the QD base and GaAs surface is larger in QD1 than in QD2 [c.f. Figure 4.1(d) and (e)].We can, therefore, state that the curvature at the bottom of QD1 reduces the elastic strain during GaAs capping. As the GaAs cap thickness increases and both QD1 and QD2 are fully capped, the elastic strain energy of QD1 saturates at a higher level than that of QD2 because of the difference in the volumes between these two structures. Therefore, QD1 is more stable than QD2 at the early stage of the capping, while the situation is reversed once both structures are fully embedded. This explains why QD1 experiences less height reduction which takes place at the beginning of capping. Furthermore, the larger elastic strain energy after capping increases the tendency for strain driven intermixing, which is most probably the driving force for the formation of the inverse-cone type composition grading which is initiated by the large strain in the bottom corners of QD1 observed in Figure 4.3(a).

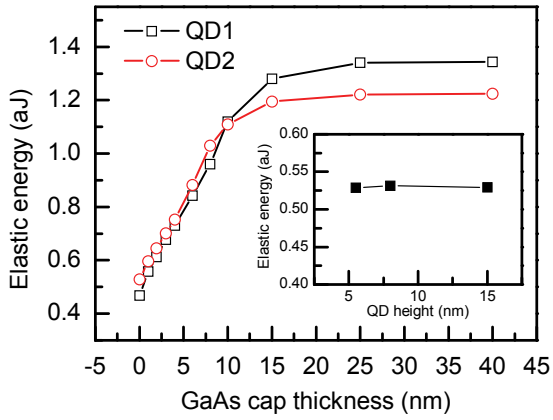

Figure 4.4. Elastic strain energy in QD1 and QD2 with respect to GaAs cap thickness. In the main plot the height of QD2 is assumed to be 5.5 nm. The inset shows the elastic energy before capping for QD2 for three truncations. The largest height represents a full pyramid.

Chapter 5

5 Electronic Properties of InAs Quantum Dots Grown in Grooves

Quantum dots composed of In(Ga)As have a smaller band gap than the surrounding GaAs matrix, and thus they provide confinement of charge carriers in all three spatial dimensions. The depth and shape of the potential well that the QD creates depends on the shape and composition of the QD as well as on the strain-induced band deformation and piezoelectricity. Confinement of charge carriers into a nanoscale volume gives rise to discretization of allowed energy states of electrons in the conduction band and holes in the valence band. The energy state hierarchy in the QD resembles that of an atom, and thus QDs are sometimes referred to as artificial atoms. The energy state structure determines, for example, the properties of the photoluminescence (PL) emission arising from the recombination of confined electrons and holes. As discussed in the previous chapter, growth on a groove pattern influences the shape, composition, and strain of InAs QDs. The impact of these morphological parameters on the electronic properties of InAs QDs is discussed in this chapter.

5.1 Band gap

The unstrained bulk band gaps ($E_g(0)$) of InAs and GaAs at 0 K temperature are 0.417 eV and 1.519 eV, respectively. For the ternary InGaAs compound with In composition x_{In} the bandgap can be estimated by cubic interpolation [85]:

$$E_g(0) = 0.417\text{eV} \times x_{In} + 1.519\text{eV} \times (1 - x_{In}) - 0{,}447\text{eV} \times (1 - x_{In}) \times x_{In}. \qquad (5.1)$$

The temperature dependence of the InGaAs band gap can be estimated by the semi-experimental Varshni relation:

$$E_g(T) = E_g(0) - \frac{\alpha T^2}{\beta + T}, \qquad (5.2)$$

where the parameters α and β depend on x_{In} are typically obtained by a linear interpolation of the values of InAs and GaAs.

As discussed in Section 4.2.2, QD1 has an inverse-cone type composition grading, and thus its unstrained band gap will vary spatially according to Eq. (5.1). QD2, on the other hand, has a uniform band gap since it can be assumed to be composed of pure InAs. The band gaps of both QD1 and QD2 are affected by hydrostatic and shear strain components arising from the compressive lattice mismatch between In(Ga)As and GaAs.

The hydrostatic strain causes a shift of the average valence band energy $E_{v,av} = (E_{hh} + E_{lh} + E_{so})/3$, where E_{hh}, E_{lh}, and E_{so} are heavy hole, light hole, and split-off band edge energies, respectively:

$$\Delta E_{v,av}^{hydro} = a_v(\varepsilon_{xx} + \varepsilon_{yy} + \varepsilon_{zz}) \qquad (5.3a)$$

and similarly for the conduction band energy

$$\Delta E_c^{hydro} = a_c(\varepsilon_{xx} + \varepsilon_{yy} + \varepsilon_{zz}), \qquad (5.3b)$$

where a_v and a_c are hydrostatic strain deformation potentials for the valence and conduction bands, respectively. The signs of a_v and a_c are negative and positive, respectively [83,84].

The shear strain couples to the spin-orbit interaction and leads to a splitting of the valence band energies. In the case of growth on (100) surface, the energy shifts relative to $E_{hh} = E_{v,av} + \Delta_{so}/3$ (Δ_{so} is the spin-orbit splitting in the absence of strain) are as follows:

$$\Delta E_{hh}^{shear} = -\frac{1}{2}\delta E^{shear}, \qquad (5.4a)$$

$$\Delta E_{lh}^{shear} = -\frac{1}{2}\Delta_{so} + \frac{1}{4}\delta E^{shear} + \frac{1}{2}\left[\Delta_{so}{}^{2} + \Delta_{so}\delta E^{shear} + \frac{9}{4}\left(\delta E^{shear}\right)^{2}\right]^{1/2}, \quad (5.4b)$$

$$\Delta E_{so}^{shear} = -\frac{1}{2}\Delta_{so} + \frac{1}{4}\delta E^{shear} - \frac{1}{2}\left[\Delta_{so}{}^{2} + \Delta_{so}\delta E^{shear} + \frac{9}{4}\left(\delta E^{shear}\right)^{2}\right]^{1/2}. \quad (5.4c)$$

The strain-induced shift δE^{shear} depends on the surface orientation. In the case of growth on a (100) surface it can be expressed as:

$$\delta E^{shear} = 2b_t\left[\varepsilon_{zz} - \frac{1}{2}\left(\varepsilon_{xx} + \varepsilon_{yy}\right)\right], \quad (5.4)$$

where b_t is the tetragonal shear deformation potential, which has a negative sign [83,84].

In the case of compressively-strained material, such as InGaAs grown on GaAs, ε_{hydro} raises the conduction band and lowers the valence band, which leads to an overall increase of the band gap. According to our strain calculations, the ε_{hydro} is 9.0% in QD1 and 8.0% and QD2. It is therefore expected that the band gap in the In-rich core of QD1, where x_{In}=1, is larger than in QD2 that is composed of pure InAs. The shear strain, on the other hand, lifts up the heavy hole band and pulls down the light hole band. Therefore, the potential for holes is minimized in the areas where the ε_{shear} is maximized. As discussed in Section 4.2.2, QD2 exhibits a lateral anisotropy of ε_{shear}, which is expected to give rise to a lateral anisotropy of hole confinement. The influences of this anisotropy on the band gap and carrier confinement are addressed in Section 5.2, where the quantum mechanical model for electron and hole states in QDs is described.

In addition to the band deformation, there is another strain-induced phenomenon that affects the potential environment in the QD-matrix system. Shear strain induces static piezoelectric charge dipoles in the InGaAs-GaAs interfaces. The polarization vector of these dipoles can be expressed as [86]

$$\mathbf{P} = \begin{pmatrix} P_x \\ P_y \\ P_z \end{pmatrix} = e_{14}\begin{pmatrix} 2\varepsilon_{yz} \\ 2\varepsilon_{xz} \\ 2\varepsilon_{xy} \end{pmatrix}, \quad (5.5)$$

where e_{14} is the piezoelectric coefficient, which is -0.160 C/m^2 for GaAs and -0.044 C/m^2 for InAs [87]. ε_{ij} $(i \neq j)$ are off-diagonal elements of the strain tensor. The piezoelectric charge density can be calculated from the divergence of the polarization

$$\rho_{\text{piezo}} = -\text{div}\,\mathbf{P}\,. \tag{5.6}$$

The piezoelectric dipoles are in zincblende structures formed around [111]-oriented interfaces. Thus in QD1 the piezoelectric dipoles are induced around the side facets of the truncated pyramid [c.f. Figure 4.1(d)], while in QD2 they are located around the edges of the side facets [c.f. Figure 4.1(e)]. The orientation of the charges is such that the positive charge is inside the QD along the [01 $\bar{1}$] and outside the QD along the [011] direction.

5.2 Calculation of electron and hole states

The quantum mechanical models for QD1 and QD2 were created with the *nextnano*^{3} simulation package [88,89] using the three-dimensional QD geometries shown in Figure 4.1(d) and (e). The WL was excluded from the model for the sake of simplicity. Both strain-induced band deformation and piezoelectricity were included in the model. The band offsets for the In(Ga)As-GaAs interfaces were taken from the *nextnano*^{3} database. The band bending in the interfaces was obtained from the Poisson equation which was solved self-consistently with the Schrödinger equation. The calculations were performed for 10 K temperature.

The electron and hole wave functions and eigenenergies for QD1 and QD2 were solved by 8-band **k.p** method using Dresselhaus 8-band parameters (L, M, and N), which were calculated from 6-band parameters taken from the *nextnano*^{3} database. The quantum mechanical model was tested using both Dirichlet and Neumann boundary conditions. When the size of the computational cell was increased enough, both boundary conditions produced the same results. The final calculations were performed using Dirichlet boundary conditions.

Figure 5.1 shows the simulated conduction and valence band edge diagrams for QD1 and QD2 along with the ground states and first excited states for electrons and holes. Only the electron and hole ground states were analyzed in detail because exclusion of the WL will make the model inaccurate for the excited energy states located closer to the GaAs band edges. In both

QD1 [Figure 5.1(a)] and QD2 [Figure 5.1(b)], the hole ground states lie very close to the heavy hole valence band edge, while the electron ground state in QD1 is located closer to the conduction band edge than in QD2 due to the larger h value in QD1. Moreover, the band gap is larger in QD1 than in QD2 due to the larger hydrostatic strain in QD1. It should be also noted that in QD1 the tails of the electron and hole wave functions extend to the In-poor sides of the QD where the band gap is larger. This effect slightly lifts the electron states and lowers the hole states compared with the case of QD1 with a uniform In composition (simulation not shown). Consequently, the energy separation between the electron and hole ground states $\Delta E = E_{e0} - E_{h0}$ is around 1.01 eV for both QD1 and QD2, regardless of the fact that the former has a significantly larger height. In other words, the effects of the difference in the QD height are compensated by the contributions arising from the difference in the hydrostatic strain as well as in the composition. The 8-band **k.p** model takes into account the conduction band and all three valence bands shown in Figure 5.1 in the calculation of electron and hole states. This is important because, although the heavy hole band is the highest valence band in compressively strained QDs, the hole states is not purely heavy hole like due to band coupling. For example, the contributions of the conduction, heavy hole, light hole, and split-off bands to the hole grounds state of QD1 are 0.6%, 95.6%, 3.3%, and 0.5%, respectively. These values are similar to what has been reported to InAs SAQDs [90]. Similarly, there is around 5% contribution of valence bands in the electron ground state of QD1.

Figure 5.2 shows the probability densities of the ground state electrons and holes calculated for QD1 with the inverse-cone composition gradient, and for QD2 composed of pure InAs material. The vertical size of both electron and hole orbitals is larger in QD1 than in QD2 due to the larger value of h in QD1. Moreover, the inverse-cone composition gradient provides an additional lateral carrier confinement in QD1. Note that the anisotropy of both electron and hole orbitals between the vertical [100] direction and the lateral [011] direction is significantly smaller in QD1 than in QD2.

Furthermore, as shown in Figure 5.3, the lateral ε_{shear} anisotropy in QD1 causes an additional hole confinement along the [011] direction, giving rise to an in-plane hole anisotropy between the [011] and [01 $\bar{1}$] directions. The lateral anisotropy of the hole confinement arising from ε_{shear} is discussed in more detail in [P7].

The orbital shapes and energies of the electron and hole states determine photon energy, intensity, and polarization of the spontaneous emission arising from the recombination of electrons and holes in the QDs. The carrier confinement potentials, on the other hand, largely determine the temperature-dependency of the spontaneous emission. The next chapter describes the emission properties of site-controlled InAs quantum dots by means of photoluminescence experiments.

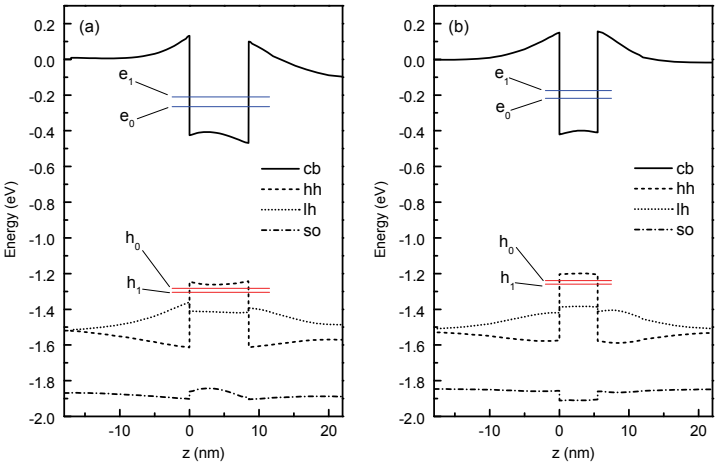

Figure 5.1. Simulated conduction and valence band structures for QD1 with an inverse-cone type composition grading (a) and QD2 composed of pure InAs (b). The band edge curves are taken vertically along the centre of the QDs.

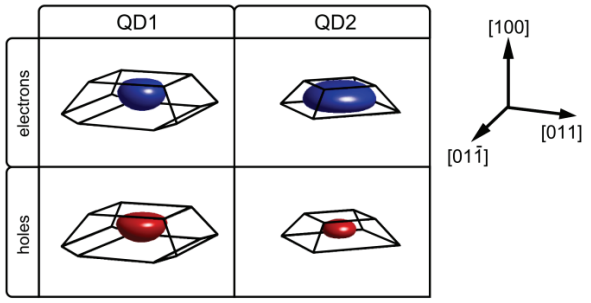

Figure 5.2. Probability densities of the ground state electrons and holes for QD1 with inverse-cone type graded composition profile (a) and for QD2 composed of pure InAs (b).

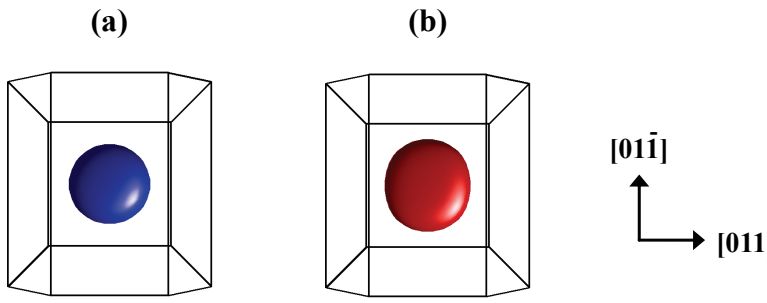

Figure 5.3. Probability densities of the ground state electrons (a) and holes (b) for QD1 with inverse-cone type graded composition profile viewed in the [100] directions.

Chapter 6

6 Optical Properties of InAs Quantum Dots Grown in Grooves

The spontaneous emission of photons that are produced by the recombination of confined electrons and holes is commonly measured by photoluminescence spectroscopy where the electron-hole pairs are created by optical pumping. The electron-hole pairs may be generated either directly to the QD (resonant injection) or to the GaAs matrix or WL (non-resonant injection). In the latter case, the carriers thermalize to the confined QD states by inelastic processes involving interaction with phonons. The probability for radiative recombination of electron-hole pairs can be expressed by the oscillator strength, which for a dipole transition between ground state electrons and holes is given as [91,92]:

$$f_{e0\to h0} = \frac{2m^* \left| < \Psi_{e0} \,|\, \hat{\mathbf{e}} \bullet \vec{\mathbf{p}} \,|\, \Psi_{h0} > \right|^2}{\hbar \left(E_{e0} - E_{h0} \right)}, \tag{6.1}$$

where m^* is the carrier effective mass, $\hbar$ is Planck constant and Ψ_{e0} and Ψ_{h0} are the wave functions for ground state electrons and holes, respectively. $\hat{\mathbf{e}}$ is the unit direction vector of the photon polarization and $\vec{\mathbf{p}}$ the electron momentum operator. It should be noted that both electron and hole ground states have two-fold spin-degeneracy, and thus there are altogether four possible transitions between the hole ground state and electron ground state, but only two of these transitions are allowed by the spin selection rules. The probability of the radiative ground state transition is thus the sum of the oscillator strengths of the two spin allowed transitions.

6.1 Excitonic transitions

In semiconductor structures with higher dimensionality the radiative recombination of electrons and holes can be either band-to-band transition or recombination of excitons which are bound states of electrons and holes that are attracted to each other by Coulomb forces [93]. However, in a zero-dimensional structure, such as a QD, only excitonic transitions exist because the recombining electrons and holes are always bound to each other within the small volume confined by the QD.

Figure 6.1(a) shows a schematic illustration of a single exciton, negatively charged exciton, and biexciton formed by ground state electrons and holes in a QD that has two allowed energy states for both electrons and holes. The recombination of a single exciton produces a narrow homogenously broadened Lorentzian spectral peak. A typical exciton lifetime for InAs/GaAs QDs emitting below 1000 nm is around 700 ps [17], which equals few μeV lifetime broadened peak width. However, the peak widths observed in steady-state PL spectra [Figure 6.1(b)] are usually slightly broader due to a time-dependent Stark shift caused by charge fluctuations in the proximity of the QD [94]. For example, the exciton peak widths of single InAs QDs grown by MBE on NIL patterned GaAs are around 40 μeV [17,60].

Figure 6.1(c) shows a simulated PL spectrum of an ensemble of 100 QDs, which illustrates exciton peaks corresponding to the ground state (GS) and excited state (ES1 and ES2) transitions. The exciton peaks of the ensemble are spectrally scattered according to the Gaussian size distribution. The ensemble and single QD PL spectra can be measured with micro-PL measurement systems, which use microscope objectives for focusing excitation laser and collecting PL signal. A typical PL setup equipped with a regular lens collects light from a macroscopic ensemble of QDs. Figure 6.1(d) shows the quasi-continuous PL spectrum measured from such ensemble. As we can see from Figure 6.1(d), a macro PL spectrum does not provide information about the Lorentzian peak widths of individual QDs. Instead, the width of the spectral peaks of the ground state and excited state transitions are determined by the width of the Gaussian size distribution.

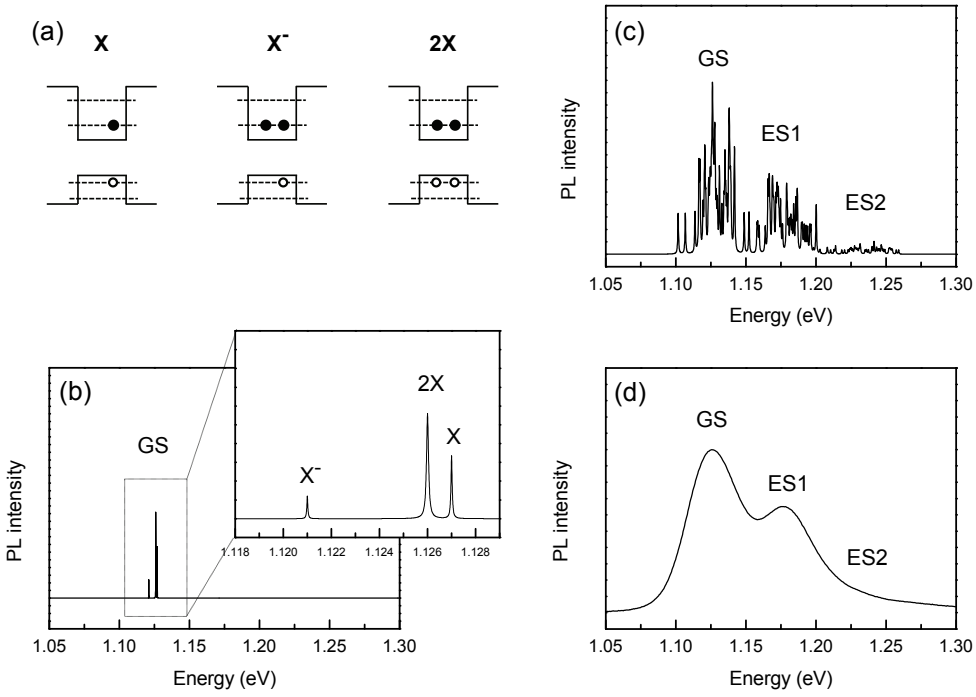

Figure 6.1. Schematic illustration of spontaneous emission by exciton recombination. (a) shows excitons formed by different ground state electron (●) and hole (○) configurations: single exciton (X), negatively charged exciton (X^-), and biexciton (2X). (b) is a simulated PL spectrum showing ground state (GS) exciton peaks of a single QD. (c) is a simulated PL spectrum showing GS and two lowest excited state (ES1 and ES2) exciton peaks of an ensemble of 100 QDs that have a Gaussian size distribution. (d) is a PL spectrum that shows emission from a macroscopic ensemble of QDs with Gaussian size distribution.

6.2 Carrier dynamics

The carrier dynamics in a three-state system consisting of the QD, the WL, and the GaAs matrix involve several processes in addition to radiative recombination in the QD. One prominent process at higher temperatures is non-radiative recombination in defects and other non-radiative recombination centres. Thus assuming that the oscillator strengths of two QD structures are similar, the PL intensity measured at room temperature can be exploited for relative analysis of

sample quality. In samples with site-controlled QDs, the non-radiative centres are most probably related to residual impurities from the NIL process and other regrowth related defects. In [P2] we compared the room temperature PL intensities of site-controlled QDCs and SAQDs and observed that the PL intensities of the QDCs are in the range from 11% to 24% compared with the SAQDs grown on an unprocessed GaAs subsrate. This relatively small difference in the room temperature PL intensities shows that the UV-NIL process causes only minor damage to the sample quality.

The carriers that have been captured by the QDs may also be emitted back to the WL. This process is thermally activated and its activation energy is related to the potential barrier between the QD states and the WL. The exact activation energy depends on the nature of the escape process, which may be either single carrier escape, exciton escape, or escape of uncorrelated electron-hole pairs [95–97]. In [P6] we studied the thermally activated carrier escape from site-controlled QDCs and SAQDs by temperature-dependent PL experiments and observed that QDCs and SAQDs have different predominant carrier escape processes: exciton escape for the SAQDs and either single carrier escape or escape of uncorrelated electron-hole for the QDCs. Furthermore, we observed that the small QDs formed on the sidewalls of the $[01\bar{1}]$-oriented grooves, which were discussed in Section 3.3, act as shallow carrier traps, which thermally release the carriers back to the WL at the temperature range from 20 K to 70 K. The activation energy of this thermally activated carrier transfer process [98] was determined as 11 meV by fitting a model to the temperature dependent intensity data. The details of the model are presented in [P6].

6.3 Polarization of photoluminescence emission

The polarization of the spontaneous emission from the recombination of electrons and holes in a QD depends on the shape of the electron and hole orbitals as well as the strain state of the QD. A lateral anisotropy of the QD shape gives rise to an in-plane optical anisotropy which is observed as different PL intensities for the polarizations along the [011] and $[01\bar{1}]$ directions. The difference of the in-plane and out-of-plane polarizations can be measured by collecting PL light from the side of the sample in so-called cleaved-edge geometry, which is illustrated in [P7] (Figure 1). Compressively strained QDs with low *AR* are typically in-plane polarized due to the

predominantly heavy hole like valence band states [99]. The polarization of the cleaved-edge PL can be quantified by the degree of polarization

$$DOP = \frac{I_{TM} - I_{TE}}{I_{TM} + I_{TE}} \times 100\%, \tag{6.2}$$

where I_{TM} and I_{TE} are the intensities of the out-of-plane and in-plane polarized PL emissions, respectively. I_{TM} and I_{TE} for the ground state transition were determined by fitting Gaussian peaks to the cleaved-edge PL spectra shown in Figure 6.2. The resulting experimental values of *DOP* for SAQDs (QD2) and QDCs (QD1) grown in [01 $\bar{1}$]-oriented grooves were found to be -59% and -19%, respectively [P7]. A theoretical estimation for *DOP* can be calculated from Eq. (6.2) by replacing the intensities with oscillator strengths calculated for different polarizations from Eq. (6.1). By doing this we obtain *DOP*=-21% for QD1 and *DOP*=-61% for QD2, which are in a remarkable agreement with the experimental values. Both QD1 and QD2 are in-plane polarized, but for QD1 the relative intensity of out-of-plane polarized emission is stronger than for QD2. This can be attributed to larger *AR* as well as the additional lateral confinement provided by the inverse-cone type composition gradient.

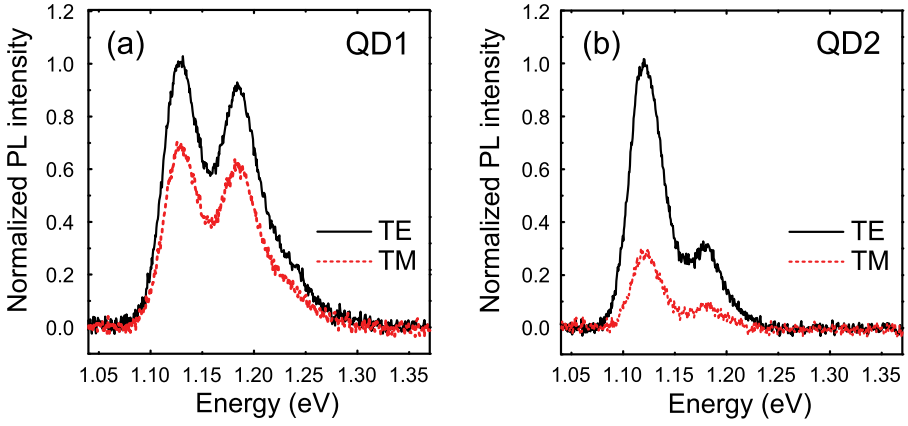

Figure 6.2. Cleaved-edge PL spectra for QD1 (a) and QD2 (b) measured at 10 K for vertical (TM) and horizontal (TE) electric field polarizations.

In [P2] we observed that in-plane optical anisotropy of QDCs grown in grooves with different orientations can be decomposed into two components: one which is along the $[01\bar{1}]$ direction and one which tends to align along the orientation of the groove. According to the DFTEM analysis of the QD morphology, the QDs grown in the grooves are elongated along the $[01\bar{1}]$ direction, regardless of the pattern orientation. Thus the component of the anisotropy that is aligned along the $[01\bar{1}]$ direction can be attributed to the shape elongation. The other component, which depends on the groove orientation, can be explained with the help of the quantum mechanical model described earlier in Chapter 5. As shown in Figure 5.3, the shear strain anisotropy arising from the influence of the groove on the shape of the bottom of the dot causes an anisotropy of the hole orbital. Such orbital shape causes an in-plane polarization along the direction of the groove. Another possible cause for the polarization along the groove is dot-to-dot coupling between the adjacent QDs. However, the hole orbital anisotropy shown in Figure 5.3 is large enough to fully explain the in-plane PL polarizations of QDCs with different orientations, which are shown in [P2] (Figure 3). The ability to tune the orientation of the polarization anisotropy by changing the groove direction is a unique property of the QDCs grown in the grooves. The following section presents two methods for modifying their in-plane polarization anisotropy.

6.4 Modification of photoluminescence properties

There are two very common methods for modifying the emission energy InAs QDs: Capping the QDs with a thin InGaAs layer can be exploited for red-shifting [100–102] and thermal annealing for blue-shifting [103–108] the emission of the QDs. In [P4] and P[5] we investigated the influence of these methods on the emission energy and in-plane polarization anisotropy of site-controlled QDCs grown in grooves. The main observations from these experiments are summarized in this chapter.

6.4.1 InGaAs capping

Capping the InAs QDs with a thin InGaAs layer has a strain relieving effect [101,102]. Thus such InGaAs cap layers are called strain reducing layers (SRL). Furthermore, InGaAs capping is known to increase the effective size of the QDs. In [P4] we investigated the influence of

$In_{0.1}Ga_{0.9}As$ thickness on the properties of site-controlled QDCs grown in [011]-, [01 $\bar{1}$]-, and [010]-oriented grooves. We observed that, similarly to SAQDs, the QDCs experience a red-shift of the ground state PL peak energy with increasing SRL thickness, which saturates once the SRL thickness is increased up to a certain level. This saturation point depends on the orientation of the groove pattern. Most rapid saturation was observed for the [011]-oriented QDCs and slowest saturation for the [01 $\bar{1}$]-oriented QDCs. The QDCs grown in the [010]-oriented grooves experience similar red-shift behavior as the SAQDs. This orientation-dependence of the PL red-shift can be explained by the anisotropy of the In migration during InGaAs capping, which controls the accumulation of an In-rich alloy on the of the QDs during the SRL growth.

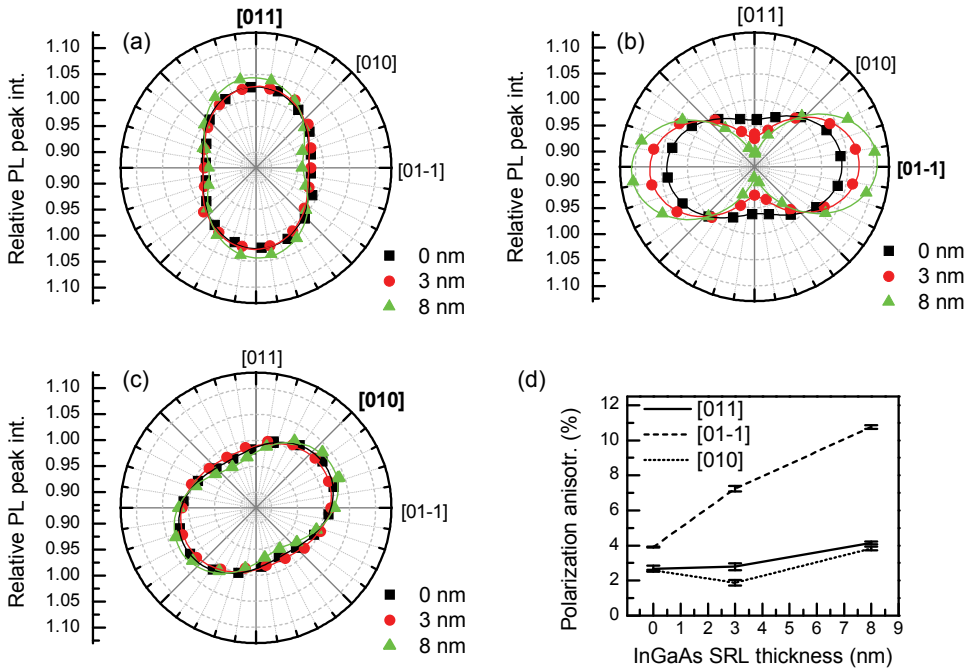

Figure 6.3. In-plane polarization of ground transition for QDCs capped with 0 nm, 3 nm, and 8 nm InGaAs layers. (a)–(c) represent [011]-, [01 $\bar{1}$]-, and [010]-oriented QDCs, respectively. (d) shows *DOP* as a function of InGaAs layer thickness for QDCs with different orientations.

As shown in Figure 6.3, InGaAs capping gives rise to only a very weak increase of the in-plane polarization anisotropy for [011]-and [010]-oriented QDCs. However, the [01 $\bar{1}$]-oriented QDCs exhibit a strong increase of polarization with increasing SRL thickness. Furthermore, the [01 $\bar{1}$]-oriented QDCs show signatures of interdot coupling which get more pronounced when the SRL grows thicker [P4]. The enhancement of coupling in the [01 $\bar{1}$]-oriented QDCs by InGaAs capping is consistent with the fact that they show significantly larger red-shift than SAQDs and the other QDC orientations [P4].

6.4.2 Thermal annealing

Annealing can be performed either in situ in the MBE chamber under protective arsenic flux [103,104] or ex situ in a rapid thermal annealing (RTA) apparatus [105–108]. In the latter case the surface of the sample can be protected for example with a GaAs proximity cap wafer or a thin dielectric layer in order to avoid As desorption that degrades the sample quality. In [P5] we performed the thermal annealing by RTA at 720 °C for site-controlled QDCs using proximity capping. The RTA treatment was conducted in 100 to 200 second steps and room temperature PL spectra were recorded after each step.

We observed that the blue-shift, which is caused by the reduction of the In composition in the QDs by thermally activated intermixing, is more rapid for the QDCs than for SAQDs. For the QDCs, the blue-shift of the ground state PL peak was 120 meV after the 1400s total annealing time, while at that point the SAQDs had experienced only 80 meV blue-shift. After an additional 200 second annealing step, also the SAQDs reached total blue-shift of 120 meV. The intermixing of In and Ga atoms over the QD-matrix interface is driven by the composition gradient as well as the elastic strain energy arising from the lattice mismatch. As discussed in Chapter 4, the QDs grown in the grooves are larger in size than the SAQDs after embedding in GaAs. The larger volume of strained InAs material (i.e. larger elastic energy) that causes the formation of the inverse-cone composition grading also increases the tendency for thermally activated intermixing in RTA. Furthermore, any residual impurities from the patterning process may promote defect-mediated diffusion in RTA, and thus lead to a more rapid blue-shift for the site-controlled QDCs than for SAQDs grown on an unprocessed GaAs wafer.

The polarization-resolved PL experiments carried out for QDCs before and after RTA (Figure 6.4) showed that the optical anisotropy arising from the elongation of the QD bases along the

[$01\bar{1}$] direction is reduced in the annealing process. Such behavior is expected since post-growth RTA is commonly used for reducing the fine structure splitting caused by the inherent lateral shape anisotropy of InAs/GaAs(100) SAQDs [109]. Interestingly, however, the part of the in-plane optical anisotropy along the orientation of the groove either increases or is unaffected by annealing, which may be related to the role of the non-planar WL to the intermixing process.

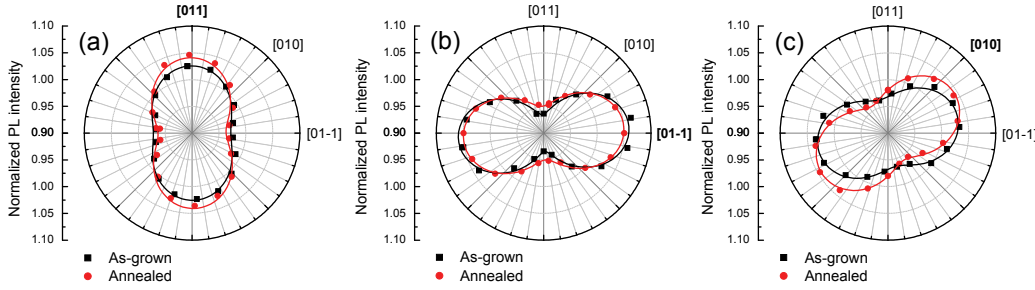

Figure 6.4. In-plane polarization of ground transition before and after annealing. (a)–(c) represent [011]-, [$01\bar{1}$]-, and [010]-oriented QDCs, respectively.

Chapter 7

7 Conclusions

The most important achievements of this thesis are the demonstration of a new nanomaterial system composed of site-controlled InAs QDCs grown in NIL-prepared grooves and a thorough investigation of their structural and optical properties. In particular, it was shown that QDCs with similar QD density and emission energy can be formed simultaneously in grooves with different orientations by proper control of the growth parameters and pattern morphology. Furthermore, it was shown that the site-controlled QDCs have high optical quality and that they exhibit an in-plane optical anisotropy. The orientation of the in-plane optical anisotropy depends on the orientation of the QDC and its magnitude can be adjusted by thermal annealing and InGaAs capping.

In more general perspective, this thesis revealed that the nanopattern on which the site-controlled QDs are grown has a strong influence on their structural properties, including the aspect ratio, strain profile, and composition profile. These properties are strongly cross-correlated and they all influence the electronic and optical characteristics of the QDs. The consequence of the findings is two-fold: (i) The morphology of the pattern has to be carefully considered in order to avoid unwanted optical anisotropies, but (ii) the morphology of the pattern can also be used as a design parameter for obtaining QDs with properties that are precisely suitable for a given application. For example, the growth of QDs in the grooves increases their oscillator strength of the vertically polarized spontaneous emission, which is the polarization component that can be coupled to surface plasmons in a metal film. This polarization property accompanied with the possibility of deterministic lateral positioning

makes the site-controlled QDCs potential building blocks of future plasmonic waveguides and networks.

The work on integration of site-controlled QDCs and plasmonic metal structures has already produced interesting unpublished results which are not included in this thesis. This work was started by modifying the NIL process and MBE growth in order to obtain QDCs with larger lateral separation, which enables single-QDC spectroscopy by micro-PL. The first test structures having QDCs with 1000 nm separation coupled to surface plasmons in a silver film are currently being investigated.

The parallel branch of research work that focuses on single InAs QDs grown on NIL patterns has moved towards formation of closely space QD ensembles for quantum dot cellular automata [110] as well as MBE growth of QDs in selectively-etched pyramidal pits on GaAs(111)B surface. The latter method is based on facet selective growth and so far it has been attained only by MOCVD [51]. The benefit of MBE in this respect is the ability to grow also planar layers on GaAs(111)B. The knowledge obtained from the experiments presented in this thesis will be valuable for understanding the facet formation during the MBE overgrowth of the pyramidal pits as well as the subsequent QD formation. This material system provides another potential platform for the integration of site-controlled III-V QDs and plasmonics as well as in situ formation of plasmonic structures by epitaxial growth of single-crystalline metal nanocrystals and nanowires directly on top of the QDs [111].

The site-controlled InAs QDCs also exhibit great potential as the gain medium in QD-based ultra-low threshold photonic crystal lasers. Research activities on this application are currently being planned. In this respect, however, there is still work to be done on the QD size uniformity.

To conclude, this thesis presents a new material system consisting of site-controlled InAs QDCs with different orientations as well as the ground work on the investigation of their material properties. The current level of technology is deemed as appropriate for development of advanced photonic devices.

Bibliography

[1] L. Goldstein, F. Glas, J. Y. Marzin, M. N. Charasse, and G. Le Roux, "Growth by molecular beam epitaxy and characterization of InAs/GaAs strained-layer superlattices", *Appl. Phys. Lett.* **47**, 1099 (1985).

[2] J. M. Moison, F. Houzay, F. Barthe, L. Leprince, E. Andre, and O. Vatel, "Self-organized growth of regular nanometer-scale InAs dots on GaAs", *Appl. Phys. Lett.* **64**, 196 (1994).

[3] A. Madhukar, Q. Xie, P. Chen, and A. Konkar, "Nature of strained InAs three-dimensional island formation and distribution on GaAs (100)", *Appl. Phys. Lett.* **64**, 2727 (1994).

[4] D. Leonard, M. Krishnamurthy, S. Fafard, J. L. Merz, and P. M. Petroff, "Molecular beam epitaxy growth of quantum dots from strained coherent uniform islands of InGaAs on GaAs", *Journal of Vacuum Science & Technology B* **12**, 1063 (1994).

[5] M. Grundmann, *Nano-Optoelectronics* (Springer, New York, 2002).

[6] A. Martí, E. Antolin, C. R. Stanley, C. D. Farmer, N. López, P. Diaz, E. Canovas, P. G. Linares, and A. Luque, "Production of photocurrent due to intermediate-to-conduction-band transitions: a demonstration of a key operating principle of the intermediate-band solar cell", *Phys. Rev. Lett.* **97**, 247701 (2006).

[7] O. Benson, C. Santori, M. Pelton, and Y. Yamamoto, "Regulated and entangled photons from a single quantum dot", *Phys. Rev. Lett.* **84**, 2513 (2000).

[8] D. Loss and D. P. DiVincenzo, "Quantum computation with quantum dots", *Physical Review A* **57**, 120 (1998).

[9] C. -. Wang, L. Y. Lin, and B. A. Parviz, "Modeling and simulation for a nano-photonic quantum dot waveguide fabricated by DNA-directed self-assembly", *Selected Topics in Quantum Electronics, IEEE Journal of* **11**, 500 (2005).

[10] S. Strauf, K. Hennessy, M. T. Rakher, Y. Choi, A. Badolato, L. C. Andreani, E. L. Hu, P. M. Petroff, and D. Bouwmeester, "Self-tuned quantum dot gain in photonic crystal lasers", *Phys. Rev. Lett.* **96**, 127404 (2006).

[11] M. Felici, P. Gallo, A. Mohan, B. Dwir, A. Rudra, and E. Kapon, "Site-Controlled InGaAs Quantum Dots with Tunable Emission Energy", *Small* **5**, 938 (2009).

[12] D. Dai, Y. Shi, S. He, L. Wosinski, and L. Thylen, "Gain enhancement in a hybrid plasmonic nano-waveguide with a low-index or high-index gain medium", *Optics Express* **19**, 12925 (2011).

[13] R. F. Oulton, "Plasmonics: Loss and gain", *Nature Photonics* **6**, 219 (2012).

[14] J. Tommila, A. Tukiainen, J. Viheriälä, A. Schramm, T. Hakkarainen, A. Aho, P. Stenberg, M. Dumitrescu, and M. Guina, "Nanoimprint lithography patterned GaAs templates for site-controlled InAs quantum dots", *J. Cryst. Growth* **323**, 183 (2011).

[15] J. Tommila, C. Strelow, A. Schramm, T. V. Hakkarainen, M. Dumitrescu, T. Kipp, and M. Guina, "The influence of temperature on the photoluminescence properties of single InAs quantum dots grown on patterned GaAs", *Nanoscale research letters* **7**, 1 (2012).

[16] J. Tommila, A. Schramm, T. V. Hakkarainen, M. Dumitrescu, and M. Guina, "Size-dependent properties of single InAs quantum dots grown in nanoimprint lithography patterned GaAs pits", *Nanotechnology* **24**, 235204 (2013).

[17] A. Schramm, J. Tommila, C. Strelow, T. V. Hakkarainen, A. Tukiainen, M. Dumitrescu, A. Mews, T. Kipp, and M. Guina, "Large array of single, site-controlled InAs quantum dots fabricated by UV-nanoimprint lithography and molecular beam epitaxy", *Nanotechnology* **23**, 175701 (2012).

[18] M. A. Herman and H. Sitter, *Molecular Beam Epitaxy – Fundamentals and Current Status* (Springler-Varlag, Berlin, 1989).

[19] R. F. C. Farrow, *Molecular Beam Epitaxy – Applications to Key Materials* (Noyes Publications, New Jersey, 1995).

[20] M. Henini, *Molecular Beam Epitaxy: From Research to Mass Production* (Elsevier, Oxford, 2012).

[21] V. A. Shchukin and D. Bimberg, "Spontaneous ordering of nanostructures on crystal surfaces", *Reviews of Modern Physics* **71**, 1125 (1999).

[22] J. W. Matthews and A. E. Blakeslee, "Defects in epitaxial multilayers: I. Misfit dislocations", *J. Cryst. Growth* **27**, 118 (1974).

[23] X. Wallart, O. Schuler, D. Deresmes, and F. Mollot, "Composition effect on the growth mode, strain relaxation, and critical thickness of tensile GaInP layers", *Appl. Phys. Lett.* **76**, 2080 (2000).

[24] C. Heyn, "Critical coverage for strain-induced formation of InAs quantum dots", *Physical Review B* **64**, 165306 (2001).

[25] S. Wang, T. G. Andersson, V. D. Kulakovskii, and J. Yao, "Critical layer thickness in InGaAs/GaAs quantum wells studied by photoluminescence and transmission electron microscopy", *Superlattices and Microstructures* **9**, 123 (1991).

[26] D. Heitmann, *Quantum Materials* (Springer Verlag, Berlin, 2010).

[27] K. H. Schmidt, G. Medeiros-Ribeiro, U. Kunze, G. Abstreiter, M. Hagn, and P. M. Petroff, "Size distribution of coherently strained InAs quantum dots", *J. Appl. Phys.* **84**, 4268 (1998).

[28] G. Costantini, A. Rastelli, C. Manzano, R. Songmuang, O. G. Schmidt, K. Kern, and H. von Kanel, "Universal shapes of self-organized semiconductor quantum dots: Striking similarities between InAs/GaAs(001) and Ge/Si(001)", *Appl. Phys. Lett.* **85**, 5673 (2004).

[29] M. C. Xu, Y. Temko, T. Suzuki, and K. Jacobi, "Shape transition of InAs quantum dots on GaAs (001)", *J. Appl. Phys.* **98**, 083525 (2005).

[30] R. Songmuang, S. Kiravittaya, and O. G. Schmidt, "Shape evolution of InAs quantum dots during overgrowth", *J. Cryst. Growth* **249**, 416 (2003).

[31] N. N. Ledentsov, V. A. Shchukin, M. Grundmann, N. Kirstaedter, J. Böhrer, O. Schmidt, D. Bimberg, V. M. Ustinov, A. Y. Egorov, and A. E. Zhukov, "Direct formation of vertically coupled quantum dots in Stranski-Krastanow growth", *Physical Review B* **54**, 8743 (1996).

[32] G. Costantini, A. Rastelli, C. Manzano, P. Acosta-Diaz, R. Songmuang, G. Katsaros, O. G. Schmidt, and K. Kern, "Interplay between thermodynamics and kinetics in the capping of InAs/GaAs (001) quantum dots", *Phys. Rev. Lett.* **96**, 226106 (2006).

[33] P. B. Joyce, T. J. Krzyzewski, G. R. Bell, B. A. Joyce, and T. S. Jones, "Composition of InAs quantum dots on GaAs (001): Direct evidence for (In, Ga) As alloying", *Physical Review B* **58**, R15981 (1998).

[34] I. Kegel, T. H. Metzger, A. Lorke, J. Peisl, J. Stangl, G. Bauer, J. M. García, and P. M. Petroff, "Nanometer-scale resolution of strain and interdiffusion in self-assembled InAs/GaAs quantum dots", *Phys. Rev. Lett.* **85**, 1694 (2000).

[35] C. Heyn, A. Bolz, T. Maltezopoulos, R. L. Johnson, and W. Hansen, "Intermixing in self-assembled InAs quantum dot formation", *J. Cryst. Growth* **278**, 46 (2005).

[36] P. D. Quinn, N. R. Wilson, S. A. Hatfield, C. F. McConville, G. R. Bell, T. C. Q. Noakes, P. Bailey, S. Al-Harthi, and F. Gard, "Composition profiles of InAs–GaAs quantum dots determined by medium-energy ion scattering", *Appl. Phys. Lett.* **87**, 153110 (2005).

[37] O. G. Schmidt, *Lateral Alignment of Epitaxial Quantum Dots* (Springer-Verlag, Berlin, 2007).

[38] D. J. Srolovitz, "On the stability of surfaces of stressed solids", *Acta Metallurgica* **37**, 621 (1989).

[39] J. Weermart and J. R. Weermart, *Elementary Dislocation Theory* (Oxford University Press, 1992).

[40] M. J. Matragrano, D. G. Ast, J. R. Shealy, and V. Krishnamoorthy, "Anisotropic strain relaxation of GaInP epitaxial layers in compression and tension", *J. Appl. Phys.* **79**, 8371 (1996).

[41] A. M. Andrews, R. LeSar, M. A. Kerner, J. S. Speck, A. E. Romanov, A. L. Kolesnikova, M. Bobeth, and W. Pompe, "Modeling crosshatch surface morphology in growing mismatched layers. Part II: Periodic boundary conditions and dislocation groups", *J. Appl. Phys.* **95**, 6032 (2004).

[42] C. Zhang, L. Tang, Y. Wang, Z. Wang, and B. Xu, "Influence of dislocation stress field on distribution of quantum dots", *Physica E: Low-dimensional Systems and Nanostructures* **33**, 130 (2006).

[43] K. M. Kim, Y. J. Park, Y. M. Park, C. K. Hyon, E. K. Kim, and J. H. Park, "Alignment of InAs quantum dots on a controllable strain-relaxed substrate using an InAs/GaAs superlattice", *J. Appl. Phys.* **92**, 5453 (2002).

[44] D. Pan, J. Xu, E. Towe, Q. Xu, and J. W. Hsu, "Self-organization of (In, Ga) As/GaAs quantum dots on relaxed (In, Ga) As films", *Appl. Phys. Lett.* **73**, 2164 (1998).

[45] K. Yamaguchi, K. Kawaguchi, and T. Kanto, "One-dimensional InAs quantum-dot chains grown on strain-controlled GaAs/InGaAs buffer layer by molecular beam epitaxy", *Japanese journal of applied physics* **41**, L996 (2002).

[46] H. Welsch, T. Kipp, C. Heyn, and W. Hansen, "Lateral self-arrangement of self-assembled InAs quantum dots by an intentional-induced dislocation network", *J. Cryst. Growth* **301**, 759 (2007).

[47] J. Martín-Sánchez, G. Muñoz-Matutano, J. Herranz, J. Canet-Ferrer, B. Alén, Y. González, P. Alonso-González, D. Fuster, L. González, and J. Martínez-Pastor, "Single photon emission from site-controlled InAs quantum dots grown on GaAs (001) patterned substrates", *ACS nano* **3**, 1513 (2009).

[48] C. Schneider, M. Straub, T. Sunner, A. Huggenberger, D. Wiener, S. Reitzenstein, M. Kamp, S. Hofling, and A. Forchel, "Lithographic alignment to site-controlled quantum dots for device integration", *Appl. Phys. Lett.* **92**, 183101 (2008).

[49] J. Skiba-Szymanska, A. Jamil, I. Farrer, M. B. Ward, C. A. Nicoll, D. J. P. Ellis, J. P. Griffiths, D. Anderson, G. A. C. Jones, and D. A. Ritchie, "Narrow emission linewidths of positioned InAs quantum dots grown on pre-patterned GaAs (100) substrates", *Nanotechnology* **22**, 065302 (2011).

[50] S. Kiravittaya, H. Heidemeyer, and O. G. Schmidt, "Growth of three-dimensional quantum dot crystals on patterned GaAs (001) substrates", *Physica E: Low-dimensional Systems and Nanostructures* **23**, 253 (2004).

[51] G. Biasiol and E. Kapon, "Mechanisms of self-ordering of quantum nanostructures grown on nonplanar surfaces", *Phys. Rev. Lett.* **81**, 2962 (1998).

[52] H. Lee, R. R. Lowe-Webb, W. Yang, and P. C. Sercel, "Formation of InAs/GaAs quantum dots by molecular beam epitaxy: Reversibility of the islanding transition", *Appl. Phys. Lett.* **71**, 2325 (1997).

[53] P. Atkinson, S. P. Bremner, D. Anderson, G. A. C. Jones, and D. A. Ritchie, "Molecular beam epitaxial growth of site-controlled InAs quantum dots on pre-patterned GaAs substrates", *Microelectron. J.* **37**, 1436 (2006).

[54] Y. Morishita, M. Ishiguro, S. Miura, and Y. Enmei, "Molecular-beam epitaxy of InAs on GaAs substrates with hole arrays patterned by focused ion beam", *J. Cryst. Growth* **237**, 1291 (2002).

[55] K. D. Jöns, P. Atkinson, M. Müller, M. Heldmaier, S. M. Ulrich, O. G. Schmidt, and P. Michler, "Triggered Indistinguishable Single Photons with Narrow Line Widths from Site-Controlled Quantum Dots", *Nano letters* **13**, 126 (2012).

[56] M. H. Baier, E. Pelucchi, E. Kapon, S. Varoutsis, M. Gallart, I. Robert-Philip, and I. Abram, "Single photon emission from site-controlled pyramidal quantum dots", *Appl. Phys. Lett.* **84**, 648 (2004).

[57] J. M. Kontio, J. Simonen, J. Tommila, and M. Pessa, "Arrays of metallic nanocones fabricated by UV-nanoimprint lithography", *Microelectronic Engineering* **87**, 1711 (2010).

[58] J. Viheriälä, J. Tommila, T. Leinonen, M. Dumitrescu, L. Toikkanen, T. Niemi, and M. Pessa, "Applications of UV-nanoimprint soft stamps in fabrication of single-frequency diode lasers", *Microelectronic Engineering* **86**, 321 (2009).

[59] J. Tommila, V. Polojärvi, A. Aho, A. Tukiainen, J. Viheriälä, J. Salmi, A. Schramm, J. M. Kontio, A. Turtiainen, and T. Niemi, "Nanostructured broadband antireflection coatings on AlInP fabricated by nanoimprint lithography", *Solar Energy Mater. Solar Cells* **94**, 1845 (2010).

[60] J. Tommila,"Nanoscale Architecture for Site-controlled Epitaxy and Antireflective Coatings", Ph.D. Thesis, Tampere University of Technology, 2013, http://URN.fi/URN:ISBN:978-952-15-3150-7.

[61] A. Kley, P. Ruggerone, and M. Scheffler, "Novel diffusion mechanism on the GaAs (001) surface: the role of adatom-dimer interaction", *Phys. Rev. Lett.* **79**, 5278 (1997).

[62] T. Shitara, D. D. Vvedensky, M. R. Wilby, J. Zhang, J. H. Neave, and B. A. Joyce, "Misorientation dependence of epitaxial growth on vicinal GaAs (001)", *Physical Review B* **46**, 6825 (1992).

[63] G. R. Bell, T. S. Jones, and B. A. Joyce, "Direct observation of anisotropic step activity on GaAs (001)", *Surf. Sci.* **429**, L492 (1999).

[64] N. Moll, A. Kley, E. Pehlke, and M. Scheffler, "GaAs equilibrium crystal shape from first principles", *Physical Review B* **54**, 8844 (1996).

[65] M. Rosini, M. C. Righi, P. Kratzer, and R. Magri, "Indium surface diffusion on InAs (2× 4) reconstructed wetting layers on GaAs (001)", *Physical Review B* **79**, 075302 (2009).

[66] J. Márquez, P. Kratzer, L. Geelhaar, K. Jacobi, and M. Scheffler, "Atomic structure of the stoichiometric gaas (114) surface", *Phys. Rev. Lett.* **86**, 115 (2001).

[67] R. Beanland, "Dark field transmission electron microscope images of III–V quantum dot structures", *Ultramicroscopy* **102**, 115 (2005).

[68] J. P. McCaffrey, M. D. Robertson, S. Fafard, Z. R. Wasilewski, E. M. Griswold, and L. D. Madsen, "Determination of the size, shape, and composition of indium-flushed self-assembled quantum dots by transmission electron microscopy", *J. Appl. Phys.* **88**, 2272 (2000).

[69] G. D. Lian, J. Yuan, L. M. Brown, G. H. Kim, and D. A. Ritchie, "Modification of InAs quantum dot structure by the growth of the capping layer", *Appl. Phys. Lett.* **73**, 49 (1998).

[70] M. V. Maximov, A. F. Tsatsulnikov, B. V. Volovik, D. A. Bedarev, A. Y. Egorov, A. E. Zhukov, A. R. Kovsh, N. A. Bert, V. M. Ustinov, and P. S. Kopev, "Optical and structural properties of InAs quantum dots in a GaAs matrix for a spectral range up to 1.7 μm", *Appl. Phys. Lett.* **75**, 2347 (1999).

[71] H. Blank, D. Litvinov, R. Schneider, D. Gerthsen, T. Passow, and K. Scheerschmidt, "Quantification of the In-distribution in embedded InGaAs quantum dots by transmission electron microscopy", *Crystal Research and Technology* **44**, 1083 (2009).

[72] F. Heinrichsdorff, A. Krost, M. Grundmann, D. Bimberg, A. Kosogov, and P. Werner, "Self-organization processes of InGaAs/GaAs quantum dots grown by metalorganic chemical vapor deposition", *Appl. Phys. Lett.* **68**, 3284 (1996).

[73] O. Flebbe, H. Eisele, T. Kalka, F. Heinrichsdorff, A. Krost, D. Bimberg, and M. Dahne-Prietsch, "Atomic structure of stacked InAs quantum dots grown by metal-organic chemical vapor deposition", *Journal of Vacuum Science & Technology B: Microelectronics and Nanometer Structures* **17**, 1639 (1999).

[74] H. Eisele, O. Flebbe, T. Kalka, C. Preinesberger, F. Heinrichsdorff, A. Krost, D. Bimberg, and M. Dahne-Prietsch, "Cross-sectional scanning-tunneling microscopy of stacked InAs quantum dots", *Appl. Phys. Lett.* **75**, 106 (1999).

[75] K. Ozasa, Y. Aoyagi, M. Iwaki, and H. Kurata, "Facets, indium distribution, and lattice distortion of InGaAs/GaAs quantum dots observed by three-dimensional scanning transmission electron microscope", *J. Appl. Phys.* **94**, 313 (2003).

[76] K. Du, Y. Rau, N. Y. Jin-Phillipp, and F. Phillipp, "Lattice distortion analysis directly from high resolution transmission electron microscopy images-the LADIA program package", *Cailiao Kexue Yu Jishu(Journal of Materials Science & Technology)(China)(USA)* **18**, 135 (2002).

[77] R. Bierwolf, M. Hohenstein, F. Phillipp, O. Brandt, G. E. Crook, and K. Ploog, "Direct measurement of local lattice distortions in strained layer structures by HREM", *Ultramicroscopy* **49**, 273 (1993).

[78] H. Chung, Y. Lai, C. Liu, Y. Lai, Y. Fang, and L. Hsu, "Correlation of In–Ga intermixing with band-tail states in InAs/GaAs quantum dots", *Appl. Phys. Lett.* **92**, 051903 (2008).

[79] M. A. Migliorato, A. G. Cullis, M. Fearn, and J. H. Jefferson, "Atomistic simulation of strain relaxation in In{x}Ga{1-x}As/GaAs quantum dots with nonuniform composition", *Physical Review B* **65**, 115316 (2002).

[80] G. R. Liu and Quek Jerry S.S., "A finite element study of the stress and strain fields of InAs quantum dots embedded in GaAs", *Semiconductor science and technology* **17**, 630 (2002).

[81] T. Benabbas, Y. Androussi, and A. Lefebvre, "A finite-element study of strain fields in vertically aligned InAs islands in GaAs", *J. Appl. Phys.* **86**, 1945 (1999).

[82] N. Liu, J. Tersoff, O. Baklenov, A. L. Holmes Jr, and C. K. Shih, "Nonuniform Composition Profile in In{0.5}Ga{0.5}As Alloy Quantum Dots", *Phys. Rev. Lett.* **84**, 334 (2000).

[83] C. G. Van de Walle, "Band lineups and deformation potentials in the model-solid theory", *Physical Review B* **39**, 1871 (1989).

[84] M. P. C. M. Krijn, "Heterojunction band offsets and effective masses in III-V quaternary alloys", *Semiconductor Science and Technology* **6**, 27 (1991).

[85] I. Vurgaftman, J. R. Meyer, and L. R. Ram-Mohan, "Band parameters for III–V compound semiconductors and their alloys", *J. Appl. Phys.* **89**, 5815 (2001).

[86] G. Bester and A. Zunger, "Cylindrically shaped zinc-blende semiconductor quantum dots do not have cylindrical symmetry: Atomistic symmetry, atomic relaxation, and piezoelectric effects", *Physical Review B* **71**, 045318 (2005).

[87] S. de Gironcoli, S. Baroni, and R. Resta, "Piezoelectric properties of III-V semiconductors from first-principles linear-response theory", *Phys. Rev. Lett.* **62**, 2853 (1989).

[88] J. A. Majewski, S. Birner, A. Trellakis, M. Sabathil, and P. Vogl, "Advances in the theory of electronic structure of semiconductors", *physica status solidi (c)* **1**, 2003 (2004).

[89] D. Grützmacher, T. Fromherz, C. Dais, J. Stangl, E. Müller, Y. Ekinci, H. H. Solak, H. Sigg, R. T. Lechner, and E. Wintersberger, "Three-dimensional Si/Ge quantum dot crystals", *Nano letters* **7**, 3150 (2007).

[90] T. Saito, H. Ebe, Y. Arakawa, T. Kakitsuka, and M. Sugawara, "Optical polarization in columnar InAs/GaAs quantum dots: 8-band k· p calculations", *Physical Review B* **77**, 195318 (2008).

[91] F. M. Peeters, A. Matulis, M. Helm, T. Fromherz, and W. Hilber, "Oscillator strength and sum rule for intersubband transitions in a superlattice", *Physical Review B* **48**, 12008 (1993).

[92] V. G. Stoleru and E. Towe, "Oscillator strength for intraband transitions in (In, Ga) As/GaAs quantum dots", *Appl. Phys. Lett.* **83**, 5026 (2003).

[93] W. Y. Liang, "Excitons", *Physics Education* **5**, 226 (1970).

[94] M. Bayer and A. Forchel, "Temperature dependence of the exciton homogeneous linewidth in In_ {0.60} Ga_ {0.40} As/GaAs self-assembled quantum dots", *Physical Review B* **65**, 041308 (2002).

[95] S. Sanguinetti, M. Henini, M. G. Alessi, M. Capizzi, P. l. Frigeri, and S. Franchi, "Carrier thermal escape and retrapping in self-assembled quantum dots", *Physical Review B* **60**, 8276 (1999).

[96] G. Gélinas, A. Lanacer, R. Leonelli, R. A. Masut, and P. J. Poole, "Carrier thermal escape in families of InAs/InP self-assembled quantum dots", *Physical Review B* **81**, 235426 (2010).

[97] W. Yang, R. R. Lowe-Webb, H. Lee, and P. C. Sercel, "Effect of carrier emission and retrapping on luminescence time decays in InAs/GaAs quantum dots", *Physical Review B* **56**, 13314 (1997).

[98] L. Brusaferri, S. Sanguinetti, E. Grilli, M. Guzzi, A. Bignazzi, F. Bogani, L. Carraresi, M. Colocci, A. Bosacchi, and P. Frigeri, "Thermally activated carrier transfer and luminescence line shape in self-organized InAs quantum dots", *Appl. Phys. Lett.* **69**, 3354 (1996).

[99] A. V. Koudinov, I. A. Akimov, Y. G. Kusrayev, and F. Henneberger, "Optical and magnetic anisotropies of the hole states in Stranski-Krastanov quantum dots", *Physical Review B* **70**, 241305 (2004).

[100] M. Hugues, M. Teisseire, J. -. Chauveau, B. Vinter, B. Damilano, J. -. Duboz, and J. Massies, "Optical determination of the effective wetting layer thickness and composition in InAs⁄Ga (In) As quantum dots", *Physical Review B* **76**, 075335 (2007).

[101] F. Guffarth, R. Heitz, A. Schliwa, O. Stier, N. N. Ledentsov, A. R. Kovsh, V. M. Ustinov, and D. Bimberg, "Strain engineering of self-organized InAs quantum dots", *Physical Review B* **64**, 085305 (2001).

[102] D. Litvinov, H. Blank, R. Schneider, D. Gerthsen, T. Vallaitis, J. Leuthold, T. Passow, A. Grau, H. Kalt, and C. Klingshirn, "Influence of InGaAs cap layers with different In concentration on the properties of InGaAs quantum dots", *J. Appl. Phys.* **103**, 083532 (2008).

[103] R. Leon, Y. Kim, C. Jagadish, M. Gal, J. Zou, and D. J. H. Cockayne, "Effects of interdiffusion on the luminescence of InGaAs/GaAs quantum dots", *Appl. Phys. Lett.* **69**, 1888 (1996).

[104] A. O. Kosogov, P. Werner, U. Gosele, N. N. Ledentsov, D. Bimberg, V. M. Ustinov, A. Y. Egorov, A. E. Zhukov, P. S. Kopev, and N. A. Bert, "Structural and optical properties of InAs–GaAs quantum dots subjected to high temperature annealing", *Appl. Phys. Lett.* **69**, 3072 (1996).

[105] S. Malik, C. Roberts, R. Murray, and M. Pate, "Tuning self-assembled InAs quantum dots by rapid thermal annealing", *Appl. Phys. Lett.* **71**, 1987 (1997).

[106] C. Lobo, R. Leon, S. Fafard, and P. G. Piva, "Intermixing induced changes in the radiative emission from III–V quantum dots", *Appl. Phys. Lett.* **72**, 2850 (1998).

[107] S. J. Xu, X. C. Wang, S. J. Chua, C. H. Wang, W. J. Fan, J. Jiang, and X. G. Xie, "Effects of rapid thermal annealing on structure and luminescence of self-assembled InAs/GaAs quantum dots", *Appl. Phys. Lett.* **72**, 3335 (1998).

[108] R. Leon, S. Fafard, P. G. Piva, S. Ruvimov, and Z. Liliental-Weber, "Tunable intersublevel transitions in self-forming semiconductor quantum dots", *Physical Review B* **58**, R4262 (1998).

[109] D. J. P. Ellis, R. M. Stevenson, R. J. Young, A. J. Shields, P. Atkinson, and D. A. Ritchie, "Control of fine-structure splitting of individual InAs quantum dots by rapid thermal annealing", *Appl. Phys. Lett.* **90**, 011907 (2007).

[110] F. Perez-Martinez, I. Farrer, D. Anderson, G. A. C. Jones, D. A. Ritchie, S. J. Chorley, and C. G. Smith, "Demonstration of a quantum cellular automata cell in a GaAs/AlGaAs heterostructure", *Appl. Phys. Lett.* **91**, 032102 (2007).

[111] A. Urbanczyk and R. Notzel, "Site-controlled Ag nanocrystals grown by molecular beam epitaxy—Towards plasmonic integration technology", *J. Appl. Phys.* **112**, 124302 (2012).

P1

Publication 1

T. V. Hakkarainen, A. Schramm, A. Tukiainen, R. Ahorinta, L. Toikkanen and M. Guina, “Lateral Ordering of InAs Quantum Dots on Crosshatch Patterned GaInP”, Nanoscale Research Letters, vol. 5, no. 12, pp. 1892-1896, 2010.

Nanoscale Res Lett (2010) 5:1892–1896
DOI 10.1007/s11671-010-9747-2

SPECIAL ISSUE ARTICLE

Lateral Ordering of InAs Quantum Dots on Cross-hatch Patterned GaInP

Teemu Hakkarainen · Andreas Schramm · Antti Tukiainen · Risto Ahorinta · Lauri Toikkanen · Mircea Guina

Received: 19 June 2010 / Accepted: 6 August 2010 / Published online: 20 August 2010

Abstract We report the use of partially relaxed tensile as well as compressively strained GaInP layers for lateral ordering of InAs quantum dots with the aid of misfit dislocation networks. The strained layers and the InAs QDs were characterized by means of atomic force microscopy, scanning electron microscopy, and X-ray reciprocal space mapping. The QD-ordering properties of compressive GaInP are found to be very similar with respect to the use of compressive GaInAs, while a significantly stronger ordering of QDs was observed on tensile GaInP. Furthermore, we observed a change of the major type of dislocation in GaInP layers as the growth temperature was modified.

Keywords Molecular beam epitaxy · III-V semiconductors · Quantum dots · Ordering · InAs · GaInP

Introduction

The fabrication of high-quality, coherently strained quantum dots (QDs) is necessary for numerous electronic and photonic applications. Self-assembled QDs obtained from the Stranski–Krastanov (SK) growth mode fulfill the quality requirements for fabrication of devices, such as QD-based laser diodes and detectors. A disadvantage of the self-organizing SK growth is that the QDs are randomly distributed. Ability to create ordered QD structures, i.e. deterministically positioned QDs, is essential for enabling new optical and electronic applications, such as single-photon emitters, single-electron transistors, or QD-based memory devices. One way to affect the distribution of SK QDs is to exploit the strain sensitivity of the growth process [1, 2], which can be utilized as a tool for ordering the QDs.

The strain field around misfit dislocations (MDs) in a partially relaxed compressively strained (CS) GaInAs layer grown on a GaAs substrate has been shown to be promising in ordering InAs QDs [3–6]. Nevertheless, GaInAs has a relatively low band gap difference with respect to InAs, GaInAs, or InP QDs, while a strong confinement of charge carriers would be desirable in most optical applications. As a solution, we here propose using partially relaxed GaInP layers, which not only have a higher band gap than GaInAs but also enable both compressively (CS) as well as tensile-strained (TS) growth on a GaAs substrate. Non-relaxed GaInP layers grown on GaAs substrates have been successfully used as templates for InP and InAs QDs [7, 8] and as a tool for engineering the properties of InAs QDs [9]. Furthermore, a strong ordering of InP QDs has been observed on partially relaxed CS-GaInP [10]. In this article, we present lateral ordering of InAs QDs on TS- and CS-GaInP layers and compare these two cases with CS-GaInAs. So far, it has been shown that the ordering of QDs can be achieved by exploiting the strain field of a MD [3–6] or surface morphology [11], but here we show that these two effects can be combined together in order to enhance ordering of QDs.

Experiment

A set of four QD samples was grown on GaAs(100) substrates by solid-source molecular beam epitaxy. All the QD samples were comprised a 60-nm thick partially relaxed, strained layer capped with a GaAs layer and covered with

T. Hakkarainen (✉) · A. Schramm · A. Tukiainen · R. Ahorinta · L. Toikkanen · M. Guina
Optoelectronics Research Centre, Tampere University of Technology, Korkeakoulunkatu 3, 33720 Tampere, Finland
e-mail: teemu.hakkarainen@tut.fi

InAs QDs. The materials of the strained layers investigated here are CS-$Ga_{0.85}In_{0.15}As$ (sample A), CS-$Ga_{0.38}In_{0.62}P$ (samples B and C), and TS-$Ga_{0.66}In_{0.34}P$ (sample D), all being 1% lattice mismatched to the GaAs substrate, the first two compounds being compressively and the third tensile-strained. The CS-$Ga_{0.85}In_{0.15}As$ and CS-$Ga_{0.66}In_{0.34}P$ layers in samples A and B, respectively, were grown at 520°C. The TS-$Ga_{0.66}In_{0.34}P$ layer in sample D was grown at a lower temperature of 430°C in order to avoid transition from 2D to 3D growth mode, which is typical for this material when grown at higher temperature [12]. For the sake of comparison, we also prepared a QD sample C with a CS-$Ga_{0.38}In_{0.62}P$ layer grown at 430°C. The strained layers in the QD samples were covered with 30-nm thick GaAs cap layers, which served as templates for 2.2 monolayers (ML) of InAs QDs grown with a growth rate of 0.02 ML/s. The GaAs cap layers and QDs were grown at 540°C. Furthermore, 60- and 80-nm thick TS-$Ga_{0.66}In_{0.34}P$ layers (samples E and F) without the GaAs cap layer and QDs were grown 430°C in order to determine the critical layer thickness for the formation of dislocations in this TS material. Further details of the samples are listed in Table 1.

For post-growth characterization, we used atomic force microscopy (AFM), scanning electron microscopy (SEM), and high-resolution X-ray diffractometry (HR-XRD). AFM was used for analyzing the surface morphology of the samples as well as for determination of the average heights (h_{QD}) and densities (ρ_{QD}) of the QDs. The lateral ordering of QDs on dislocations was investigated with SEM. HR-XRD reciprocal space maps (RSM) were measured around (004) and (113) reflections for both [011] and [0–11] sample orientations in order to determine the crystal quality, In composition (x_{In}) and relaxation state ($R_{[hkl]}$) of the strained layers.

Results and Discussion

Before discussing the lateral ordering of QDs on the MD networks induced by the TS- and CS-GaInP and -GaInAs layers, it is necessary to evaluate the critical thickness and the type of dislocations generated. The critical thickness for the TS-$Ga_{0.66}In_{0.34}P$ was estimated based on the SEM observations of the dislocation induced lines on the sample surfaces (not shown) and RSM results. The values of relaxation as well as major dislocation types for each sample are listed in Table 1. According to the RSM measurement, sample E was fully strained and no lines were observed in the SEM pictures. On the other hand, sample F showed a very low density of [0–11]-oriented β-dislocations indicating an early stage of strain relaxation. Thus, the critical thickness of TS-$Ga_{0.66}In_{0.34}P$ was estimated to be around 80 nm. The critical thicknesses of the CS layers were not determined in this study. However, according to Ref. [4], 50 nm is a sufficient layer thickness to produce a MD network in a $Ga_{0.85}In_{0.15}As$ layer grown at 520°C. Based on similar surface morphologies (Fig. 3a–c) and values of strain relaxation (Table 1), we assume that CS-$Ga_{0.38}In_{0.62}P$ and CS- $Ga_{0.85}In_{0.15}As$ layers investigated here have a critical thickness below 60 nm.

According to Table 1, the major dislocation type in CS-$Ga_{0.38}In_{0.62}P$ changes from α to β as the growth temperature is decreased from 520 to 430°C. The thickness of the TS-$Ga_{0.66}In_{0.34}P$ layer in sample D is lower than the critical value. Hence, the dislocations were actually generated after the GaInP layer growth either during the temperature ramp from 430 to 540°C or during the growth of the GaAs layer. The fact that samples D and F have different major dislocation types suggests that also TS-$Ga_{0.66}In_{0.34}P$ experiences a change of the major dislocation type as the temperature is increased. What makes this observation interesting is that α-dislocations have been assumed to be the predominant dislocation type in all cases due to their larger glide velocity [14].

The strain relaxation values on Table 1 show that the strained layers in all of the QD samples are at the early stage of strain relaxation. This is also observed in the RSM of sample D shown in Fig. 1. Both GaAs and GaInP peaks as well as satellite peaks are well observable, indicating good crystal quality and low strain relaxation. The RSMs

Table 1 Details of the investigated samples. x_{In} and $R_{[hkl]}$ were calculated from RSM peak data, and h_{QD} and ρ_{QD} were determined for 1 μm × 1 μm and 10 μm × 10 μm AFM images, respectively [13]. The major dislocation type was determined based on several 20 μm × 20 μm SEM pictures

Sample	Material	Strain	T_g (°C)	X_{In}	$R_{[011]}$ (%)	$R_{[01\text{-}1]}$ (%)	h_{QD} (nm)	ρ_{QD} (cm^{-2})	Maj. Dislocation type
A	GaInAs	CS	520	0.142	1.60	1.40	13	5.0×10^9	α[0–11]
B	GaInP	CS	520	0.618	1.50	1.60	14	5.1×10^9	α[0–11]
C	GaInP	CS	430	0.617	1.70	1.60	13	5.6×10^9	β[011]
D	GaInP	TS	430	0.354	2.60	1.90	16	4.2×10^9	α[011]
E	GaInP	TS	430	0.34	0.00	0.00	No QDs	No QDs	No dislocations
F	GaInP	TS	430	–	–	–	No QDs	No QDs	β[0–11]

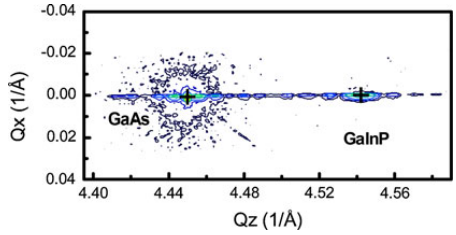

Fig. 1 XRD reciprocal space map measured from a 60-nm $Ga_{0.66}In_{0.34}P$/GaAs layer (Sample D) around (004) reflection in [011] direction

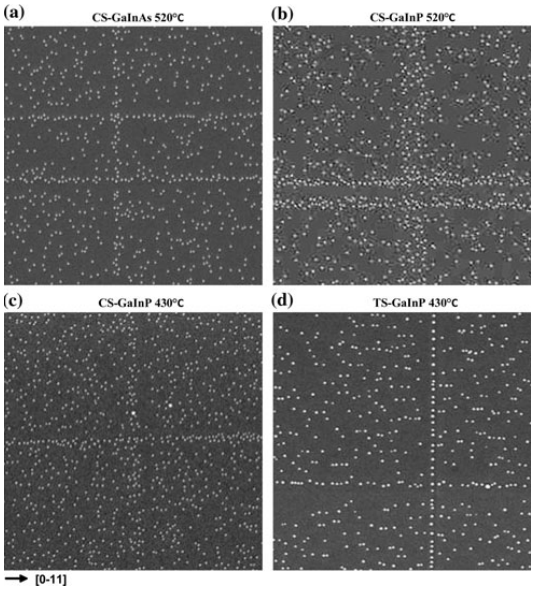

Fig. 2 SEM pictures (3.5 μm × 3.5 μm) of QD chains on 60-nm partially relaxed GaInP and GaInAs layers. Figures **a**–**d** correspond to samples A–D, respectively. The layer material and growth temperature of each sample are indicated in the figure

of the other samples (not presented here) showed similar features.

Figure 2 shows SEM pictures illustrating the ordering of QDs on CS and TS layers. On the CS layers (Fig. 2a–c), the QDs are gathered on MDs, but the ordering is relatively weak. However, on the TS layer (Fig. 2d), the QD accumulation on the MDs differs with respect to the CS layers. On TS layers, the QDs on the MDs are ordered in narrow single-dot wide chains. Furthermore, according to the quantitative data extracted from the AFM pictures and summarized in Table 1, the height and density of the QDs depend on the properties of the strained layer below them; compared to the TS-$Ga_{0.66}In_{0.34}P$, the QDs on the CS samples are larger and less dense. This can be explained by

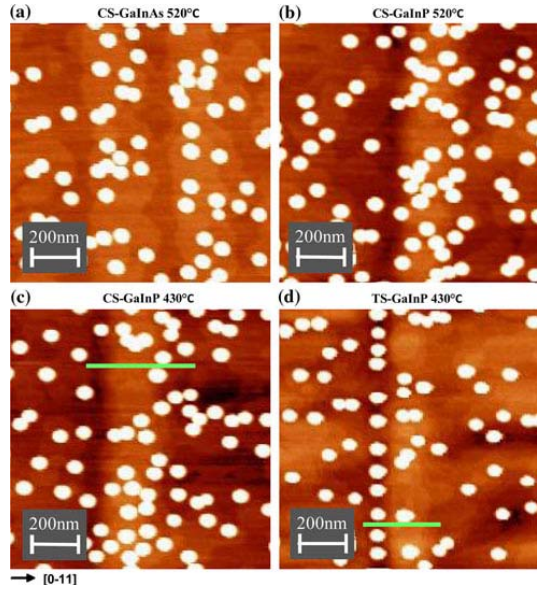

Fig. 3 AFM pictures of QDs on MDs. Figures **a**–**d** correspond to samples A–D, respectively. The color height scale in each image is 5 nm

a reduction of the critical InAs coverage for QD formation due to the compressive strain of the underlying $Ga_{0.38}In_{0.62}P$ or $Ga_{0.85}In_{0.15}As$ layer.

In order to interpret the differences of QD accumulations on MDs on TS and CS layers, we analyzed the surface morphology around the QD chains by AFM. The AFM images in Fig. 3, show a clear difference between compressive and tensile strain; the QDs on CS layers are gathered on ridges (Fig. 3a–c), which is consistent with Ref. [2] and [10], while on the TS-$Ga_{0.66}In_{0.34}P$ (Fig. 3d) the narrow QD chains are formed in grooves.

We try to explain the observed differences in ordering by calculating the stress field on the film surface above a MD for both CS and TS layers. The magnitude of the Burgers vector of a mixed 60° MD is $b = \|b\| = a/\sqrt{2}$, where a is the lattice constant [15]. The edge component of **b** can be decomposed into parts parallel and perpendicular to the layer/substrate interface: $b_{\text{edge}} = b_{\|} + b_{\perp}$. The magnitudes of the in-plane and out-of-plane components of the Burgers vector are

$$b_{\|} = \|b_{\|}\| = \frac{b}{2}, \tag{1a}$$

$$b_{\perp} = \|\mathbf{b}_{\perp}\| = \frac{b}{\sqrt{2}}. \tag{1b}$$

The formation of MDs at the layer/substrate interface induces a local stress field that affects the QD nucleation at

the sample surface. The tangential stress component of pure edge dislocation lying at the distance h below the surface is

$$\sigma_{xx}^{MD} = \frac{4G}{\pi(1-\nu)} \times \frac{hx\left(hb_{\perp} - xb_{\parallel}\right)}{\left(x^2+h^2\right)^2}, \quad (2)$$

in which G is the shear modulus, ν is the Poisson's ratio, and x is the lateral distance from the MD. Figure 4 shows strain profiles calculated with Eq. (2) for a MD in TS and CS layers using values for G and ν indicated in Table 2 and a layer thickness h of 90 nm. The in-plane and out-of-plane components of the Burgers vector were assumed to be $b_{\parallel} = -b/2$, $b_{\perp} = -b/\sqrt{2}$ for the CS layers and $b_{\parallel} = b/2$, $b_{\perp} = -b/\sqrt{2}$ for the TS layer.

In both the CS (Fig. 4a) and the TS layer (Fig. 4b), positive and negative maxima of the stress are formed on the adjacent sides of the MD. This local strain fluctuation affects the growth of the strained layer and GaAs capping layer. In Ref. [2], the authors suggested that the surface corrugation above a MD in an un-capped CS-GaInAs layer is caused by formation of In-rich alloy on the tensile part of the stress field of the MD (Fig. 4a). The growth of InAs QDs is also favored in this area of the MD due to their larger lattice constant; hence, the QDs are accumulated on the ridge. The growth of a GaAs cap may also affect the surface morphology. GaAs will most probably avoid the In-rich ridge, which experiences local tensile stress [2] and favor the Ga-rich grooves. The correlation between the stress field of a MD and surface profile for a CS-GaInP is shown in Fig. 4a. It appears that after growth of the GaAs cap the surface corrugation is formed by a ridge and a groove located above the tensile and compressive sides of the MD, respectively. In sample D, the surface corrugation is formed solely during the GaAs layer growth because the MDs are formed after the growth of the strained layer. The compressive stress of a MD locally compensates the tensile strain of the GaInP layer on the right side of the dislocation (Fig. 4b). Therefore, this area is favored by GaAs and a ridge is formed. Correspondingly, GaAs tends to avoid the tensile side of the MD, which becomes a groove. Thus, the groove is formed above the tensile side of the dislocation (Fig. 4b), not above the compressive side as in the CS-GaInP layer. The InAs QDs, however, accumulate on the tensile part of the dislocation. Thus, the ordering of QDs on TS-GaInP is guided not only by the strain field of the dislocation but also by the shape of the groove, while on the CS-GaInP and CS-GaInAs layers, the QDs accumulate on the ridges solely due to stress field of the MDs.

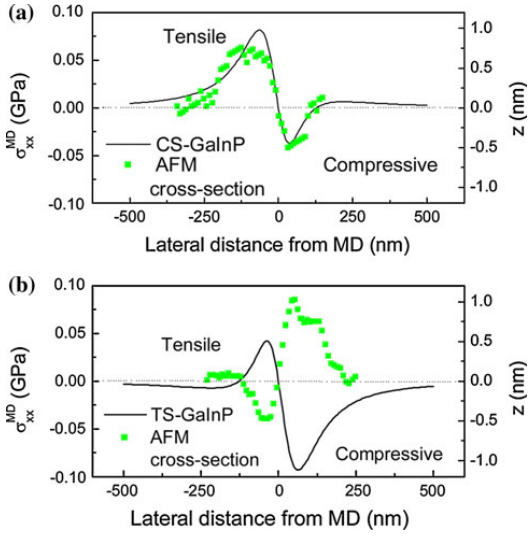

Fig. 4 Tangential stress component above a misfit dislocation calculated for **a** CS-GaInP and **b** for TS-GaInP layers. The AFM cross-sections in (**a**) and (**b**) are measured along the lines in Fig. 3c and d, respectively

Table 2 Elastic properties of TS-GaInP and CS-GaInP. Elastic constants C_{11} and C_{12} are calculated with Vegard's law using values from Ref. [16] for binary compounds. The Poisson's ratio is $\nu = C_{12}/(C_{11} + C_{12})$, and the Shear modulus is $G = (C_{11} - C_{12})/2$

Material	x_{In}	C_{11} (GPa)	C_{12} (GPa)	ν	G (GPa)
TS-GaInP	0.34	127.1	60	0.321	33.55
CS-GaInP	0.62	116.1	58.4	0.335	28.86

Conclusions

It was shown that misfit dislocation networks obtained from partially relaxed CS- and TS-GaInP layers can be utilized for lateral ordering of InAs QDs. The strongest QD ordering was observed on TS-GaInP, because of the accumulation of QDs on narrow grooves that are formed during the growth of the GaAs cap layer. The MDs on CS-GaInP and CS-GaInAs layers, in which QDs are mainly gathered on ridges, were shown to have similar QD ordering properties including line distribution and direction as well as QD height and density. Concluding, GaInP is a good candidate for replacing GaInAs in order to align QDs on MD networks and when a material of a higher band gap is required.

Acknowledgments We acknowledge financial support from Finnish National Graduate School in Materials Physics, Academy of Finland project DAUNTLESS (decision number 123951) Jenny and Antti Wihuri Foundation, and Finnish Foundation for Technology Promotion.

References

1. J. Tersoff, C. Teichert, M.G. Lagally, Phys. Rev. Lett. **76**, 1675 (1996)
2. K. Yamaguchi, E. Waki, H. Hasegawa, Jpn. J. Appl. Phys. **36**, L871 (1997)
3. C.L. Zhang, Z.G. Wang, F.A. Zhao, B. Xu, P. Jin, J. Cryst. Growth **265**, 60 (2004)
4. C.L. Zhang, B. Xu, Z.G. Wang, P. Jin, F.A. Zhao, Physica E **25**, 592 (2005)
5. Chunling Zhang, Lei Tang, Yuanli Wang, Zhanguo Wang, Bo Xu, Physica E **33**, 130 (2006)
6. K. Yamaguchi, K. Kawaguchi, T. Kanto, Jpn. J. Appl. Phys. **41**, 996 (2002)
7. H.N. Carlsson, W. Seifert, A. Petersson, P. Castrillo, M.E. Pistol, L. Samuelson, Appl. Phys. Lett. **65**, 3093 (1994)
8. H. Amanai, S. Nagao, H. Sakaki, J. Cryst. Growth **227**, 1089 (2001)
9. T. Sengoku, R. Suzuki, K. Nemoto, S. Tanabe, F. Koyama, T. Miyamoto, Jpn. J. Appl. Phys. **48**, 070203 (2009)
10. K. Häusler, K. Eberl, F. Noll, A. Trampert, Phys. Rev. B **54**, 4913 (1996)
11. H. Heidemeyer, C. Müller, O.G. Schmidt, Physica E **23**, 237 (2004)
12. X. Wallart, O. Schuler, D. Deresmes, F. Mollot, Appl. Phys. Lett. **76**, 2080 (2000)
13. I. Horcas, R. Fernandez, J.M. Gomez-Rodriguez, J. Colchero, J. Gomez-Herrero, A.M. Baro, Rev. Sci. Instrum. **78**, 013705 (2007)
14. M.J. Matragrano, D.G. Ast, J.R. Shealy, V. Krishnamoorthy, J. Appl. Phys. **79**, 8371 (1996)
15. A.M. Andrews, R. LeSar, M.A. Kerner, J.S. Speck, A.E. Romanov, A.L. Kolesnikova, M. Bobeth, W. Pompe, J. Appl. Phys. **95**, 6032 (2004)
16. I. Vurgaftman, J.R. Meyer, L.R. Ram-Mohan, J. Appl. Phys. **89**, 5815 (2001)

Publication 2

P2

T. V. Hakkarainen, J. Tommila, A. Schramm, A. Tukiainen, R. Ahorinta, M. Dumitrescu, and M. Guina, ” Structural and optical properties of InAs quantum dot chains grown on nanoimprint lithography structured GaAs with different pattern orientations”, Applied Physics Letters, vol. 97, issue 17, 173107, 2010.

Structural and optical properties of InAs quantum dot chains grown on nanoimprint lithography structured GaAs with different pattern orientations

T. V. Hakkarainen,[a] J. Tommila, A. Schramm, A. Tukiainen, R. Ahorinta, M. Dumitrescu, and M. Guina
Optoelectronics Research Centre, Tampere University of Technology, P.O. Box 692, FIN-33101 Tampere, Finland

(Received 29 September 2010; accepted 8 October 2010; published online 27 October 2010)

We use large-scale UV nanoimprint lithography prepatterned GaAs substrates for site-controlled growth of InAs quantum dot chains by molecular beam epitaxy. We demonstrate simultaneous fabrication of quantum dot chains with high optical quality along four different crystal orientations, [011], [01$\bar{1}$], [010], and [001]. We show that the [01$\bar{1}$], [010], and [001]-oriented quantum dot chains not only have similar morphology but also experience similar in-plane optical anisotropy, which tends to align along the axis of the quantum dot chain. Our optical and structural results show that InAs quantum dot chains could be a potential platform for nanophotonic waveguiding and integrated circuits. © *2010 American Institute of Physics*. [doi:10.1063/1.3506903]

High-quality, coherently strained quantum dots (QDs) are required for numerous electronic and photonic applications.[1] Self-assembled InAs QDs (SAQD) obtained using the Stranski–Krastanov (SK) growth mode fulfill the quality requirements for the fabrication of photonic devices such as QD-based laser diodes or detectors. A disadvantage of the self-organizing SK growth is that the QDs are randomly distributed. The ability to fabricate QDs on predetermined locations, i.e., site-controlled growth, is essential for enabling optical applications, such as separately addressable QDs for single-photon emitter to be used in future quantum computing devices,[2] or quantum dot chains (QDCs) for nanophotonic waveguides and integrated circuits.[3] So far, the deterministic positioning of InAs QDCs has been achieved mainly by using e-beam lithography patterning[4] or cleaved-edge overgrowth.[5] Furthermore, spontaneously assembled In(Ga)As QDCs have been achieved by InGaAs/GaAs superlattice growth[6] and by exploiting the strain fluctuations in dislocation patterned templates.[7] As an alternative method for the fabrication of site-controlled InAs QDCs, we propose nanoimprint lithography (NIL), which is able to produce sub 10 nm linewidths[8] with high throughput[9] and enables fast processing of large wafer areas.[10] Soft UV-nanoimprint lithography (UV-NIL) is a modification of NIL utilizing soft stamp and UV curable resists and has been used for the fabrication of arrays of high optical quality InAs QDs.[11]

In this paper, we report room temperature (RT) photoluminescence (PL) emission from deterministically positioned QDCs grown by molecular beam epitaxy (MBE) on UV-NIL processed groove patterns. Scanning electron microscope (SEM), atomic force microscope (AFM), and PL investigations show that this technique enables the simultaneous growth of high optical quality QDCs along four different crystal directions, [011], [01$\bar{1}$], [010], and [001]. We observe highly ordered QDCs with an in-plane optical anisotropy on [01$\bar{1}$], [010], and [001]-oriented patterns.

The investigated samples were prepared in three stages. In the first stage, a 100 nm GaAs buffer, a 100 nm AlGaAs cladding layer, and a 100 nm GaAs were deposited at 590 °C on 2″ n-GaAs(100) quarter substrates by MBE. Then the samples were *ex situ* patterned by UV-NIL. Four 10 mm × 10 mm groove patterns with different line orientations were processed on each sample. The grooves were 90 nm wide, 30 nm deep, and had a period of 180 nm. In the final stage, the patterned surface was covered with a 60 nm GaAs regrowth buffer at 490 °C and 2.2 monolayers of InAs for QD formation at 515 °C. In sample A, the QDs were left uncovered, while in sample B the QDs were covered with a 20 nm GaAs layer grown at 515 °C followed by a 50 nm GaAs, a 50 nm AlGaAs layer, and a 20 nm GaAs capping layer. Samples A and B had a nonpatterned area in the middle; the SAQDs grown in this region were used as a reference (RefA). In order to determine the effects of the patterning process on the optical properties of the QDs, we prepared a second reference sample (RefB) having the same layer structure and growth conditions as sample B but without being exposed to the UV-NIL process. AFM was used for investigating the lateral ordering of QDs on the patterned surface as well as for analyzing the surface morphology of the patterns before and after the regrowth.[12] The density of QDs on each sample was estimated from 3 μm × 3 μm SEM pictures. Optical characterization was performed by RT-PL using excitation at 532 nm. Furthermore, polarization-resolved PL was measured at 30 K using excitation at 480 nm.

Figures 1(a)–1(d) show the AFM pictures of QDCs grown on groove patterns oriented along [011], [01$\bar{1}$], [010], and [001] directions. The initially 30 nm deep grooves are still clearly visible after the growth of the 60 nm GaAs regrowth buffer, and site-controlled QDCs are observed in the grooves of each pattern. The density of the QDs on each pattern as well as on RefA it is around 1.4×10^{10} cm^{-2}, while in RefB it is 1.9×10^{10} cm^{-2}. A strong lateral ordering of QDs is observed on the [01$\bar{1}$], [010], and [001] patterns [Figs. 1(b)–1(d)] on which all QDs are placed in the grooves forming closely spaced QDCs. On the [011] pattern shown in Fig. 1(a), QDs have additionally nucleated on the ridges. The AFM pictures also reveal that the use of UV-NIL patterned

[a]Electronic mail: teemu.hakkarainen@tut.fi.

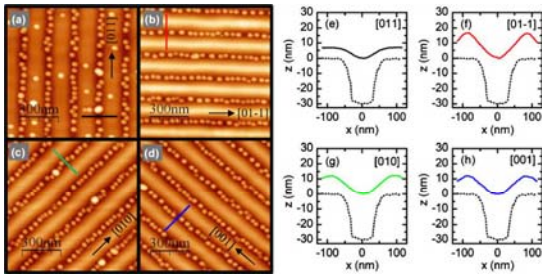

FIG. 1. (Color online) AFM pictures of QDCs grown on UV-NIL processed groove patterns (period 180 nm, depth 30 nm) oriented along different crystallographic directions. Figures 1(a)–1(d) show QDCs on patterns oriented along [011], [01$\bar{1}$], [010], and [001] directions, respectively. The color scale in (a)–(d) is 26 nm. The AFM line scans in (e)–(h) are taken along the colored lines in Figs. 1(a)–1(d), respectively. The dotted line in each plot shows the profile of the groove before the regrowth. The linescans are offset for clarity.

GaAs surface as a template enables the simultaneous growth of QDCs oriented along [011], [01$\bar{1}$], [010], and [001] directions.

Figures 1(e)–1(h) show AFM line scans taken perpendicular to the groove from Figs. 1(a)–1(d), respectively. After the growth of the 60 nm regrowth buffer, the [011]-oriented grooves, shown in Fig. 1(e), are 7 nm deep and a flat (100) plateau has formed between the grooves. This plateau is absent in the [01$\bar{1}$], [010], and [001]-oriented grooves, which have depths of 18 nm, 12 nm, and 12 nm, respectively. The formation of plateaus between the grooves oriented in [011] explains the nucleation of QDs on the ridges. Moreover, the similarities in the morphology of the QDCs formed on [01$\bar{1}$], [010], and [001] patterns is caused by similar groove morphologies. The evolution of the groove shape in the regrowth is dictated by the strong diffusion of Ga atoms in the [01$\bar{1}$] direction,[13] which causes the filling of the [011]-oriented grooves. The formation of steep grooves along the [01$\bar{1}$], [010], and [001] directions is probably enabled by facetting.

Figure 2 shows RT-PL spectra measured from the QDCs

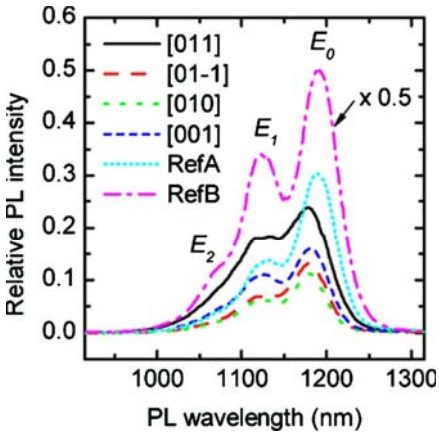

FIG. 2. (Color online) RT-PL spectra of QD chains grown on NIL processed line patterns oriented along [011], [01$\bar{1}$], [010], and [001] directions and of SAQDs on RefA and RefB.

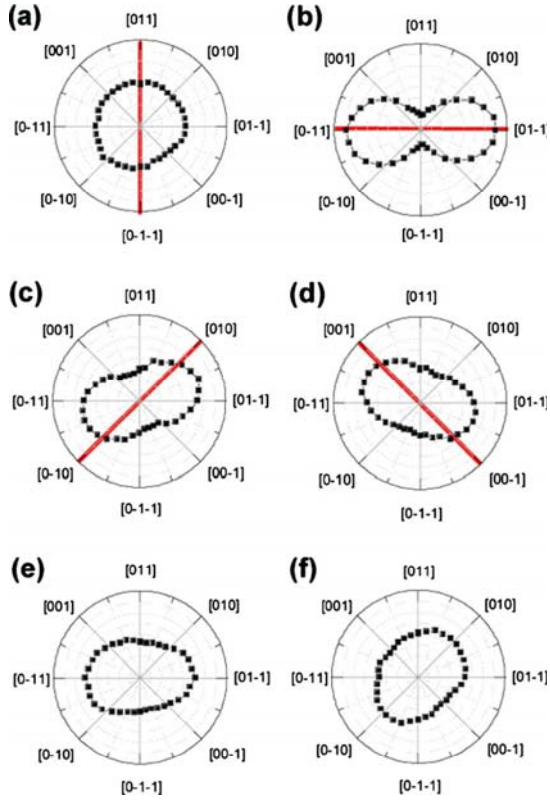

FIG. 3. (Color online) Polar plots of PL intensity as a function of electric field polarization with respect to the crystallographic directions measured at 30 K. The plots in (a)–(d) are from QD chains oriented along [011], [01$\bar{1}$], [010], and [001] directions, respectively. The plot (e) is for SAQDs on RefA and plot (f) for SAQDs on RefB. The orientation of the QD chain is designated by the thick line. The radial axis of the polar plots represents relative PL intensity from 0.9 to 1.1.

as well as from the SAQDs grown on planar surfaces (RefA and RefB). All samples show three transitions (E_0, E_1, E_2). The highest PL intensity was observed from sample RefB, which was grown on an unprocessed epiready GaAs substrate. Compared with RefB, the PL intensity of the SAQDs on a processed surface (RefA) is 30% and for the QDCs it ranges from 11% to 24%, indicating a good optical quality of the samples after the UV-NIL process. It should be noted that only chemical cleaning was used for the investigated samples prior to the regrowth. Even better relative PL intensities have been reported from site-controlled InAs QDs grown on hydrogen-cleaned NIL pattern.[11] The ground state PL peak (E_0) wavelengths for the SAQDs and QDCs are similar, 1190 nm and around 1180 nm, respectively. The 10 nm blueshift observed in the PL peak wavelength of the QDCs compared with the SAQDs may be attributed to differences in QD sizes

In Fig. 3 we present the polarization dependency of the PL emission from the QDCs and SAQDs plotted as E_0 peak intensity versus electric field orientation. According to Fig. 3(a), the PL emission from the [011]-oriented QDCs is unpolarized, while the emission from [01$\bar{1}$]-oriented QDCs, shown in Fig. 3(b), is polarized along the QDC direction. As

shown in Figs. 3(c) and 3(d), the PL emission from the [010]- and [001]-oriented QDCs is maximized in the direction which lays at half-way between the axis of the QDC and $[01\bar{1}]$ crystal direction. The SAQDs grown on processed (RefA) and unprocessed (RefB) substrates [Figs. 3(e) and 3(f)] show polarized emission with PL intensity maxima in $[01\bar{1}]$ and [010] directions, respectively.

We first discuss the polarization dependencies of the SAQDs in RefA and RefB, because it will help us to understand the results from the QDCs. According to Figs. 3(e) and 3(f), the SAQDs grown on nonpatterned processed and unprocessed GaAs surfaces exhibit an in-plane optical anisotropy with the PL intensity maximum along $[01\bar{1}]$ and [010] directions, respectively. The optical anisotropy in SAQDs is attributed to anisotropic shape elongation evolving during the capping process. In particular, the highest PL intensity is observed along the direction of the elongation.[14,15] An elongation along both $[01\bar{1}]$ (Refs. 16 and 17) and [011] (Ref. 18) directions have been reported for GaAs capped InAs QDs depending on the growth conditions. However, the different orientations of the PL intensity maximum in Figs. 3(e) and 3(f) indicate that the shape evolution of SAQDs during the capping process is dictated not only by the growth conditions but also by the properties of the surface. On the other hand, it has been shown that surface patterning does not influence the QD shape evolution.[19] We can therefore assume that individual QDs in the QDCs [Figs. 3(a)–3(d)] are elongated along $[01\bar{1}]$ direction just like the SAQDs grown on the processed surface [Fig. 3(e)]. Thus, the in-plane optical anisotropy can be decomposed into two components; one that is caused by the QD shape elongation along $[01\bar{1}]$ direction and one which is oriented along the QDC. The enhanced PL intensity along the QDC axis is likely caused by dot-to-dot quantum mechanical coupling or the formation of a one-dimensional wetting[20] or postwetting layer.[21] In the [011]-oriented QDCs [Fig. 3(a)] the above-mentioned two components cancel out each other, while in the $[01\bar{1}]$-oriented QDCs Fig. 3(b) they add up and produce high polarization anisotropy. In the [010]- and [001]-oriented QDCs [Figs. 3(c) and 3(d)] the shape elongation causes the rotation of the PL maximum from the direction of the QDC toward the $[01\bar{1}]$ crystal direction.

In conclusion, we have presented the simultaneous growth of [011]-, $[01\bar{1}]$-, [010]-, and [001]-oriented QDCs on large-scale UV-NIL patterned GaAs. Though only chemical cleaning is used after the UV-NIL process, the QDCs showed intense RT-PL indicating high optical quality. The QDCs exhibit an in-plane optical anisotropy, which tends to align along the QDC axis. Furthermore, we have shown that the QDCs oriented along the $[01\bar{1}]$, [010] and [001] directions not only have similar morphology but also experience similar optical anisotropy, which makes them a potential building block of future nanophotonic networks.

The research was carried out within the Academy of Finland project DAUNTLESS (decision number 123951). T. Hakkarainen acknowledges financial support from Finnish National Graduate School in Materials Physics, Jenny and Antti Wihuri Foundation, and Finnish Foundation for Technology Promotion. J. Tommila acknowledges the National Graduate School in Nanoscience (NGS-NANO) and the Pirkanmaa Regional Fund of the Finnish Cultural Foundation for the financial support.

[1] *Nano-Optoelectronics*, edited by M. Grundmann (Springer, New York, 2002).
[2] A. Mohan, M. Felici, P. Gallo, B. Dwir, A. Rudra, J. Faist, and E. Kapon, Nat. Photonics **4**, 302 (2010).
[3] C.-J. Wang, L. Y. Lin, and B. A. Parviz, IEEE J. Sel. Top. Quantum Electron. **11**, 500 (2005).
[4] H. Heidemeyer, C. Müller, and O. G. Schmidt, Physica E (Amsterdam) **23**, 237 (2004).
[5] G. Schedelbeck, W. Wegscheider, M. Bichler, and G. Abstreiter, Science **278**, 1792 (1997).
[6] Z. M. Wang, K. Holmes, Yu. I. Mazur, and G. J. Salamo, Appl. Phys. Lett. **84**, 1931 (2004).
[7] T. V. Hakkarainen, A. Schramm, R. Ahorinta, L. Toikkanen, and M. Guina, Nanoscale Res. Lett. (in press), doi: 10.1007/s11671-010-9747-2.
[8] J. F. Hua, Y. Sun, A. Gaur, M. A. Meitl, L. Bilhaut, L. Rotkina, J. Wang, P. Geil, M. Shim, J. A. Rogers, and A. Shim, Nano Lett. **4**, 2467 (2004).
[9] S. Y. Chou, P. R. Krauss, and P. J. Renstrom, J. Vac. Sci. Technol. B **14**, 4129 (1996).
[10] B. Heidari, I. Maximov, E.-L. Sarwe, and L. Montelius, J. Vac. Sci. Technol. B **17**, 2961 (1999).
[11] C.-C. Cheng, K. Meneou, and K. Y. Cheng, Appl. Phys. Lett. **95**, 173108 (2009).
[12] I. Horcas, R. Fernandez, J. M. Gomez-Rodriguez, J. Colchero, J. Gomez-Herrero, and A. M. Baro, Rev. Sci. Instrum. **78**, 013705 (2007).
[13] H.-C. Kan, R. Ankam, S. Shah, K. M. Micholsky, T. Tadayyon-Eslami, L. Calhoun, and R. J. Phaneuf, Phys. Rev. B **73**, 195410 (2006).
[14] H. Saito, K. Nishi, S. Sugou, and Y. Sugimoto, Appl. Phys. Lett. **71**, 590 (1997).
[15] Y. Nabetani, T. Ishikawa, S. Noda, and A. Sakaki, J. Appl. Phys. **76**, 347 (1994).
[16] R. Songmuang, S. Kiravittaya, and O. G. Schmidt, J. Cryst. Growth **249**, 416 (2003).
[17] P. B. Joyce, T. J. Krzyzewski, G. R. Bell, and T. S. Jones, Appl. Phys. Lett. **79**, 3615 (2001).
[18] G. Costantini, A. Rastelli, C. Manzano, R. Songmuang, O. G. Schmidt, K. Kern, and H. von Känel, Appl. Phys. Lett. **85**, 5673 (2004).
[19] S. Kiravittaya, A. Rastelli, and O. G. Schmidt, Appl. Phys. Lett. **87**, 243112 (2005).
[20] X. Wang, Zh. M. Wang, B. Liang, G. J. Salamo, and C.-K. Shih, Nano Lett. **6**, 1847 (2006).
[21] Zh. M. Wang, Y. I. Mazur, J. L. Shultz, G. J. Salamo, T. D. Mishima, and M. B. Johnson, J. Appl. Phys. **99**, 033705 (2006).

Publication 3

P3

T. V. Hakkarainen, J. Tommila, A. Schramm, A. Tukiainen, R. Ahorinta, M. Dumitrescu, and M. Guina, “Structural characterization of InAs quantum dot chains grown by molecular beam epitaxy on nanoimprint lithography patterned GaAs(100)”, Nanotechnology 22, 295604, 2011.

Nanotechnology **22** (2011) 295604 (7pp) doi:10.1088/0957-4484/22/29/295604

Structural characterization of InAs quantum dot chains grown by molecular beam epitaxy on nanoimprint lithography patterned GaAs(100)

T V Hakkarainen, J Tommila, A Schramm, A Tukiainen, R Ahorinta, M Dumitrescu and M Guina

Optoelectronics Research Centre, Tampere University of Technology, PO Box 692, FIN-33101 Tampere, Finland

E-mail: teemu.hakkarainen@tut.fi

Received 28 March 2011, in final form 28 April 2011
Published 17 June 2011
Online at stacks.iop.org/Nano/22/295604

Abstract

We combine nanoimprint lithography and molecular beam epitaxy for the site-controlled growth of InAs quantum dot chains on GaAs(100) substrates. We study the influence of quantum dot growth temperature and regrowth buffer thickness on the formation of the quantum dot chains. In particular, we show that by carefully tuning the growth conditions we can achieve equal quantum dot densities and photoluminescence ground state peak wavelengths for quantum dot chains grown on patterns oriented along the [011], [01$\bar{1}$], [011] and [001] directions. Furthermore, we identify the crystal facets that form the sidewalls of the grooves in the differently oriented patterns after capping and show that the existence of (411)A sidewalls causes reduction of the QD density as well as sidewall roughening.

(Some figures in this article are in colour only in the electronic version)

1. Introduction

Quantum dots (QDs) have attracted a great deal of research interest during the past two decades owing to numerous electronic and photonic applications [1]. The self-assembled InAs/GaAs QD system (SAQD) obtained by using the Stranski–Krastanov (SK) growth mode fulfills the requirements (i.e. homogeneity, density and quality) for the fabrication of important photonic devices, such as laser diodes or detectors. Nevertheless, more recent applications, such as single-photon emitters [2] or nanophotonic waveguides [3], require fabrication of QDs on pre-determined locations. This site-controlled growth mode may target either formation of a single dot or quantum dot chains (QDC). The traditional methods used so far for the positioning of InAs QDCs include the use of patterning by e-beam lithography patterning [4], cleaved-edge overgrowth [5] or selective-area growth [6]. Spontaneously assembled In(Ga)As QDCs have been achieved by InGaAs/GaAs superlattice growth [7] and by exploiting the strain fluctuations in dislocation patterned templates [8]. As an alternative method for the fabrication of site-controlled InAs QDCs, we use a combination of UV-nanoimprint lithography (UV-NIL) and molecular beam epitaxy (MBE). We have shown that this technique enables the simultaneous growth of high optical quality QDCs along four different crystal directions, [011], [01$\bar{1}$], [010] and [001] [9].

The formation of InAs QDs on patterned GaAs is strongly influenced by the surface morphology. In particular, the diffusion of indium atoms on patterned surfaces is determined not only by growth conditions but also by the nature of the crystal facets that form the pattern. While the evolution of the surface morphology of GaAs micropatterns has been thoroughly investigated [10–12], faceting of the grooves having a width below 100 nm has been less studied. In this paper, we analyze the effect of varying the thickness of the buffer grown prior to the QD formation on the density and lateral ordering of InAs QDCs oriented along [011], [01$\bar{1}$], [010] and [001]. In the same context, we analyze the influence of the QD growth temperature. In particular, we show that QDs formed in grooves with different orientations

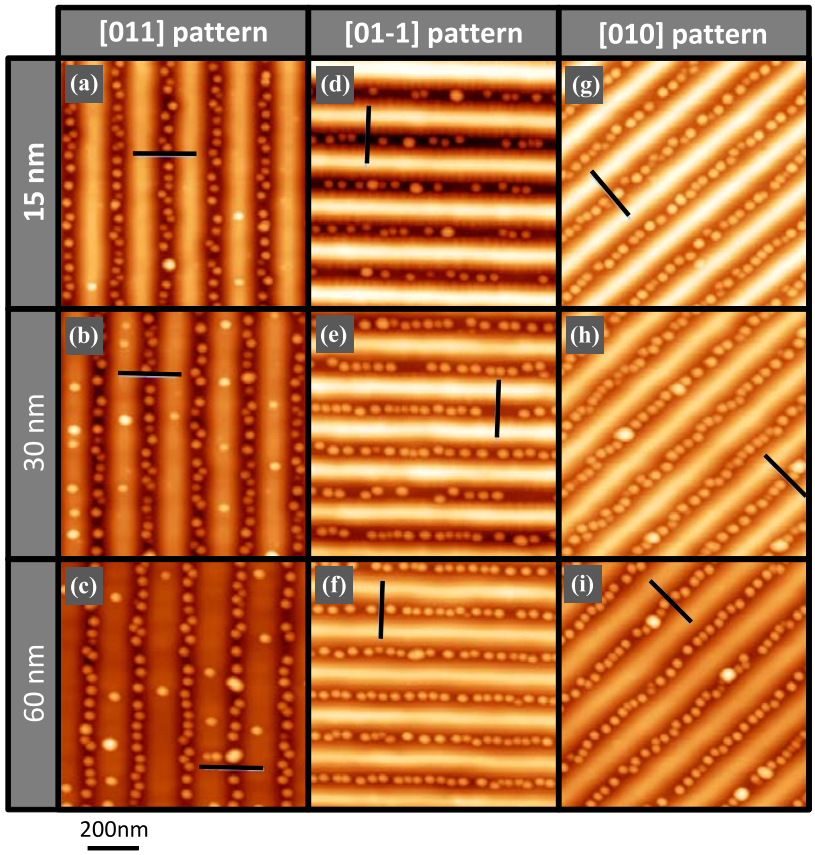

Figure 1. AFM pictures of QDCs grown on RGBs with different thicknesses. In (a)–(c) [011]-oriented QDCs, in (d)–(f) [01$\bar{1}$]-oriented QDCs, and in (g)-(i) [010]-oriented QDCs. The height scale in (a)–(i) is 35 nm.

can exhibit equal densities and similar photoluminescence (PL) peak wavelengths only by a precise adjustment of the growth parameters. Furthermore, we use an atomic force microscopy (AFM)-based facet analysis to identify the dominating facets for each groove orientation and to investigate the effect of different growth parameters on faceting.

2. Experiment

The investigated samples were prepared in three stages. In the first stage, a 100 nm GaAs buffer, a 100 nm AlGaAs layer and a 100 nm GaAs layer were deposited at 590 °C on n-GaAs(100) substrates by MBE. Then the samples were *ex situ* patterned by UV-NIL. Four 10 mm × 10 mm groove patterns with different line orientations were processed on each sample. The grooves were 90 nm wide, 30 nm deep and had a period of 180 nm. The orientations of the grooves were [011], [01$\bar{1}$], [010] and [001]. The UV-NIL process and chemical cleaning are discussed in detail in [13]. For a first set of samples, the patterned surface was covered with a 15, 30 or 60 nm thick GaAs regrowth buffer (RGB) at 490 °C. After the buffer growth 2.2 ML of InAs was deposited at 515 °C to form QDs. For a second set of samples the thickness of the RGB was fixed to 60 nm and the QD growth temperature was varied; we used temperatures of 505, 515 and 525 °C. AFM was used for investigating the lateral ordering of the QDs as well as for analyzing the morphology of the patterned surface [14]. The density of QDs on each sample was estimated from 3 μm × 3 μm scanning electron microscopy images. Room temperature PL was used for analyzing electronic properties of the QDCs. The results for the [001]-oriented patterns are not discussed in this analysis because they are identical to those corresponding to the [010] direction due to the crystallographic symmetry.

3. Experimental results

3.1. Regrowth buffer thickness

First, we investigated the effect of the RGB thickness on the formation of QDCs with different orientations. Figure 1 shows the AFM micrographs of the QDCs grown at 515 °C on 15, 30 and 60 nm thick RGBs. AFM pictures verify the formation of ordered QDCs for all orientations, i.e. [011], [01$\bar{1}$] and [010], and all RGB thicknesses. As shown in figures 1(a)–(c),

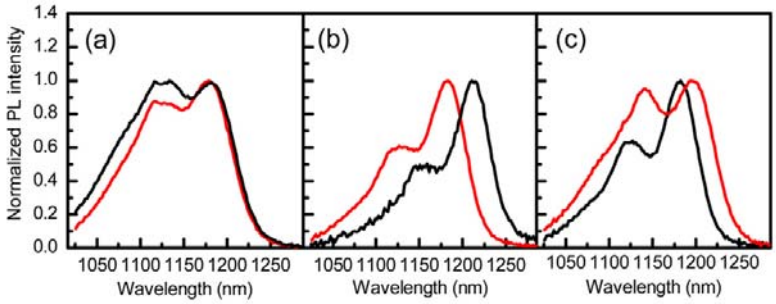

Figure 2. Room temperature PL spectra for QDC grown at 515 °C on 15 nm (black line) and on 60 nm (red line) RGBs. (a)–(c) correspond to [011]-, [01$\bar{1}$]- and [010]-oriented QDCs, respectively.

Table 1. QD densities for samples with different orientation and RGB thicknesses.

	Pattern orientation		
RGB thickness (nm)	[011] ($\times 10^{10}$ cm^{-2})	[01$\bar{1}$] ($\times 10^{10}$ cm^{-2})	[010] ($\times 10^{10}$ cm^{-2})
15	1.2	0.6	1.3
30	1.3	1.0	1.3
60	1.3	1.2	1.3

Table 2. QD densities for samples with different pattern orientation and QD growth temperatures.

	Pattern orientation		
Growth T (°C)	[011] ($\times 10^{10}$ cm^{-2})	[01$\bar{1}$] ($\times 10^{10}$ cm^{-2})	[010] ($\times 10^{10}$ cm^{-2})
505	2.9	1.6	1.9
515	1.3	1.2	1.3
525	0.9	0.7	0.9

QDs form also on the ridges of the [011]-oriented pattern and the density of these additional QDs increases with increasing RGB thickness. According to figure 1(d), the QD density on 15 nm RGB is clearly lower for the [01$\bar{1}$] pattern than for the [011] pattern. Furthermore, figure 1(d) shows roughness on the groove sidewalls. As the RGB thickness is increased to 30 nm (figure 1(e)), the roughness on the [01$\bar{1}$] pattern gets less pronounced on the groove sidewalls and the QD density increases, but is still lower than on the [011] pattern. Finally, for 60 nm RGB (figure 1(f)) the roughness on the sidewalls of the [01$\bar{1}$] pattern is further reduced and the QD density matches the density on the [011] pattern. Similar AFM pictures for the [010] pattern are shown in figures 1(g)–(i), which reveals that the QD density and ordering seem to be independent of the RGB thickness for the [010] pattern orientation. The QD densities for each groove orientation and RGB thickness are listed in table 1. The average height of the uncapped QDs on all patterns shown in figures 1(a)–(i) is about 12 nm, regardless of the groove orientation of the sidewall morphology. This indicates that the QD formation at the bottom of the groove is not affected by the sidewalls.

Figure 2 shows room temperature PL spectra for QDCs grown at 515 °C on 15 and 60 nm thick RGBs. For 15 nm RGB the ground state peak wavelengths of the [011]-, [0$\bar{1}$1]- and [010]-oriented QDCs (figures 1(a), (d) and (g)) are 1183 nm, 1212 nm and 1295 nm, respectively. Once the RGB thickness is increased to 60 nm (figures 1(c), (f) and (i)), the QDC ground state emission peaks at 1181 nm, regardless of the groove orientation.

3.2. Quantum dot growth temperature

Figure 3 shows AFM pictures of QDCs grown at temperatures of 505, 515 and 525 °C on [011], [01$\bar{1}$] and [010] patterns covered with a 60 nm thick RGB. A similar temperature dependence of the QDC formation is observed for all pattern orientations; a high density of small QDs is formed at 505 °C and with increasing growth temperatures the QD density decreases and the QD size increases. The average height of the QDs grown at temperatures of 505 °C, 515 °C and 525 °C is 7 nm, 12 nm and 13 nm, respectively. The formation of QDs on the ridges is most prominent on the [011]-oriented pattern (figures 3(a)–(c)), while no QDs are observed on the ridges of the [01$\bar{1}$]-oriented pattern at any of the growth temperatures used (figures 3(d)–(f)). On the [010]-oriented pattern, QDs are formed on the ridges only at 505 °C (figure 3(g)). Furthermore, figure 3(f) shows that, in the case of the 60 nm RGB, [01$\bar{1}$]-oriented grooves only exhibit sidewall roughening after QD growth at 525 °C. Similar roughening was observed for this pattern orientation for the RGB thicknesses of 15 and 30 nm when the QDs were grown at 525 °C (figures 1(e)–(f)). The QD densities for each groove orientation and growth temperature are listed in table 2.

Figure 4 shows room temperature PL spectra for QDCs grown at different temperatures on 60 nm thick RGBs. According to figures 4(a)–(c), the QDCs grown at the temperatures of 515 °C and 525 °C have ground state peak wavelengths of 1181 nm and 1200 nm, respectively, regardless of the groove orientation. The shift of the PL peak wavelength

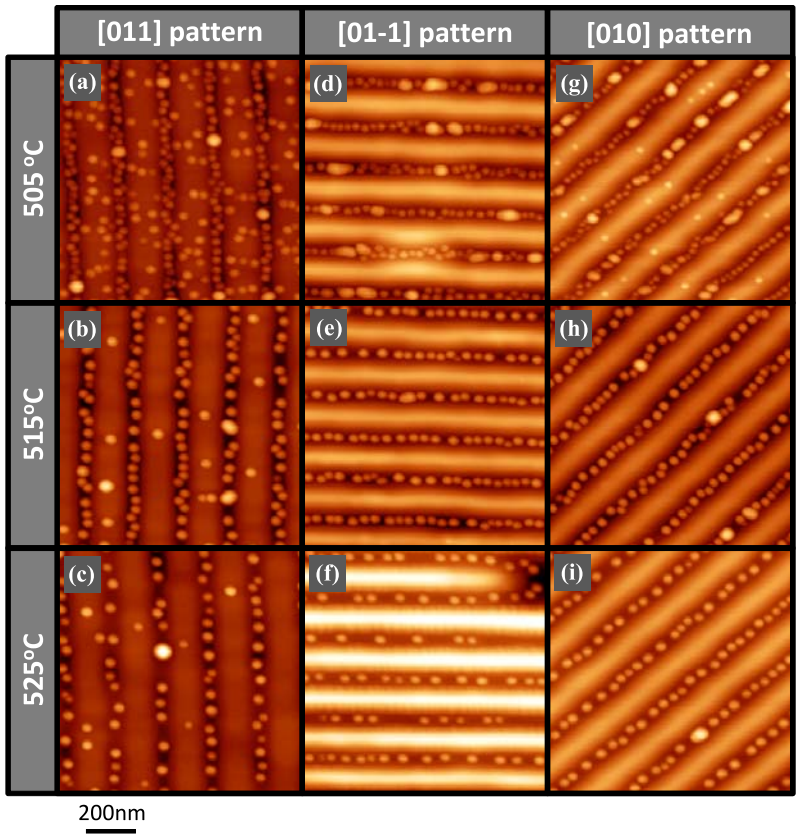

Figure 3. AFM pictures of QDCs grown at different temperatures. In (a)–(c) [011]-oriented QDCs, in (d)–(f) [01$\bar{1}$]-oriented QDCs and in (g)-(i) [010]-oriented QDCs. The height scale in (a)–(i) is 35 nm.

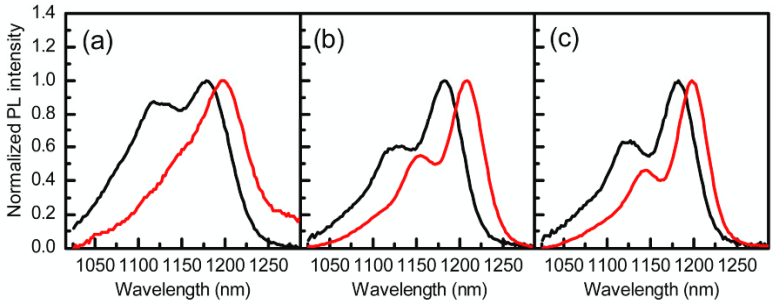

Figure 4. Room temperature PL spectra for QDC grown on 60 nm thick RGBs at 515 °C (black line) and at 525 °C (red line). (a)–(c) correspond to [011]-, [01$\bar{1}$]- and [010]-oriented QDCs, respectively.

is consistent with the increase of the height of the uncapped QDs (figure 3) as a function of the QD growth temperature.

3.3. Facet analysis

In order to explain the differences in the QD densities on differently oriented patterns we have analyzed the evolution of the groove morphology as a function of the RGB thickness. Figure 5 shows AFM line scans taken across the [011]-, [01$\bar{1}$]- and [010]-oriented grooves before the regrowth and after covering them with 15, 30 and 60 nm thick RGBs. As shown in figure 3(a), the initially 30 nm deep grooves in the [011]-oriented pattern fill rapidly as the RGB thickness

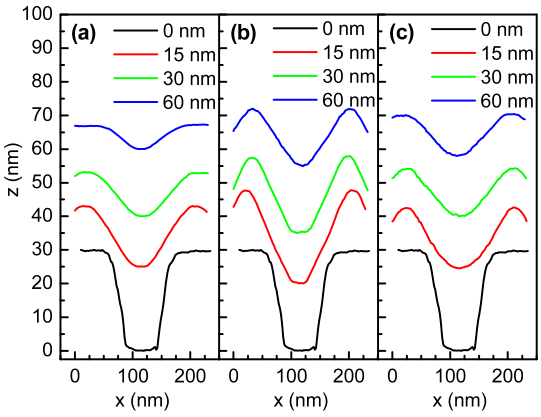

Figure 5. AFM line scans taken from figures 1(a)–(i) along the black lines. (a)–(c) show cross sections of [011]-, [01$\bar{1}$]- and [010]-oriented patterns, respectively. The curves are offset vertically for the sake of clarity.

increases leading to a reduction of the groove depth and sidewall slope. After covering them with a 60 nm RGB the groove depth is 7 nm and (100) plateaus are observed on the ridges of the pattern. The cross section of the [01$\bar{1}$]-oriented pattern (figure 5(b)) shows much clearer faceting with steeper sidewalls than in the [011]-oriented grooves in figure 5(a). Consequently, [01$\bar{1}$]-oriented grooves are 16 nm deep after covering with a 60 nm RGB. Figure 5(b) also shows that the facet angle is the same for 15 and 30 nm RGBs and it decreases as the RGB thickness is increased to 60 nm, which indicates a change of the sidewall facet planes. Figure 5(c) shows that the depth of the [010]-oriented grooves after covering with 60 nm RGB is 12 nm. In this case, a change of the facet angle is observed when the RGB thickness is increased from 15 to 30 nm, while no change is observed with an increase from 30 to 60 nm. The evolution of the groove shape at the regrowth step is dictated by a preferred diffusion of Ga atoms in the [01$\bar{1}$] direction [15], which causes the filling of the [011]-oriented grooves much faster than the [01$\bar{1}$]- or [010]-oriented grooves. The morphological evolution of the [010]-oriented pattern during the GaAs capping process is an intermediate form of the [011] and [01$\bar{1}$] orientations because it is at 45° angle with respect to both of them.

In order to identify the facet planes that form the groove sidewalls in patterns with different orientations, we have performed a facet analysis for the AFM pictures (figures 1 and 2). Figure 6 shows the facet angle distribution as a function of RGB thickness for [011]-, [01$\bar{1}$]- and [010]-oriented grooves. As shown in figure 6(a), the sidewalls of the [011]-oriented grooves are composed of (611)B facets for the RGB thicknesses of 15 and 30 nm. The small peak at 0° is originated from the (100) plateaus on the pattern ridges. After covering the [011]-oriented pattern with a 60 nm thick RGB, the facet distribution is dominated by (100) plateaus, and therefore it is impossible to identify the sidewall facets. The existence of the (100) plateaus in the [011] explains the formation of the additional QDs on the pattern ridges as shown in figures 1(a)–(c) and 3(a)–(c). In the case of the [01$\bar{1}$]-oriented grooves (figure 6(b)), the facet analysis reveals that, after being capped with 15 or 30 nm RGB, the (411)A facets are dominating. In the latter case, (611)A facets begin to appear and dominate as the RGB thickness is increased to 60 nm. The change of the dominating facets in the [0$\bar{1}$1]-oriented grooves as the RGB thickness is increased from 30 to 60 nm is also evident from the AFM line scans shown in figure 5(b). Note that in figure 6(b) the peaks at 0° result from the bottom of the grooves, not from the ridges. Furthermore, the existence of (411)A facets in the [01$\bar{1}$]-oriented grooves is accompanied by the roughening of the groove sidewalls and a low QD density, shown in figures 1(d) and (e), compared with the [011]-and [010]-oriented QDCs grown at the same growth conditions. As shown in figure 6(c), the sidewalls of the [010]-oriented pattern are formed by {410} facets when the RGB thickness is 15 nm, while the {510} facets dominate when the RGB thickness is increased to 30 or 60 nm. This change of the facet angle was also observed in the AFM line scans shown in figure 5(c). A minor contribution to the signal from the (100) ridges appears when the RGB thickness is increased to 60 nm. The formation of the additional QDs on the ridges (figure 3(g)) is associated with the existence of (100) plateaus. Thus, QDs appear on the ridge only if the top of the ridge is formed by a (100) plane. The insets in figures 6(a)–(c) illustrate the two-dimensional facet angle distributions for an RGB thickness of 60 nm. The broad background in the insets is caused by the QDs.

Figure 7 shows the facet angle distributions as a function of QD growth temperature for the [011]-, [01$\bar{1}$]- and [010]-oriented patterns covered with 60 nm RGB. No change is

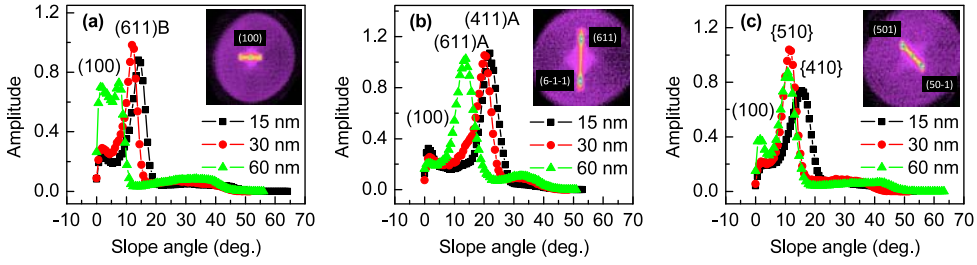

Figure 6. Facet analysis for the AFM pictures shown in figures 1(a)–(i). The curves in (a)–(c) show surface slope angle distributions after capping the NIL patterned surface with 15, 30 and 60 nm of GaAs for [011]-, [01$\bar{1}$]- and [010]-oriented grooves, respectively. The insets show two-dimensional angle distributions after capping with 60 nm of GaAs. The QD growth temperature in each sample was 515 °C.

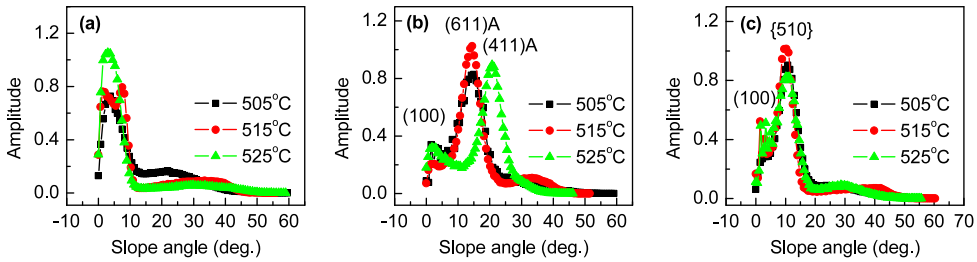

Figure 7. Facet analysis for the AFM pictures shown in figures 2(a)-(i). The curves in (a)–(c) show surface slope angle distributions after QD growth at 505 °C, 515 °C and 525 °C for [011]-, [01$\bar{1}$]- and [010]-oriented grooves, respectively. The RGB thickness in each sample was 60 nm.

observed for the facets of the [011]- and [010]-oriented patterns (figures 7(a) and (c)). However, the sidewall facets of the [01$\bar{1}$]-oriented grooves change from (611)A to (411)A as the QD growth temperature is increased from 515 to 525 °C. This indicates that the morphology of the groove pattern changes when the substrate temperature is increased after the RGB growth. The existence of the (411)A sidewalls is also in this case accompanied by the sidewall roughening and a low QD density (figure 3(f)).

4. Discussion

As shown in figures 1 and 3, well-defined QDCs were obtained in the grooves of all patterns for all growth parameters used. However, additional QDs accumulate on the ridges of the [011] pattern at all tested growth parameters. On the [010] pattern these additional QDs appear only when QDs are grown at 505 °C on a 60 nm thick RGB. On the [01$\bar{1}$] pattern QDs form only in the grooves for all tested growth conditions. According to tables 1 and 2, the QD densities on [011]-, [01$\bar{1}$]- and [010]-oriented grooves are similar only when QDs are grown at 515 °C on a 60 nm thick RGB. The ground state peak wavelengths of the PL spectra shown in figure 2 for QDCs grown at 515 °C on 15 and 60 nm RGBs are only partly consistent with the heights of the uncapped QDs on the corresponding patterns. The [011]-, [01$\bar{1}$]- and [010]-oriented QDCs grown on the 60 nm thick RGBs have similar heights and peak wavelengths. However, the QDCs with different orientations grown on the 15 nm RGBs have different peak wavelengths although the QD sizes are similar. Furthermore, the peak wavelength is redshifted for QDCs that are grown in deeper grooves. This discrepancy indicates that the groove morphology has an influence on either the QD composition or intermixing during the capping process although the sizes of the uncapped dots are similar.

According to figure 3, the size of the QDs grown on 60 nm RGBs increases with the increasing growth temperature, which causes the PL redshift shown in figure 4. The amount of redshift is similar for all pattern orientations. At the QD growth temperature of 505 °C we observe an accumulation of QDs on the ridges of the [011]-oriented pattern (figure 3(a)) and to a lesser extent on the [010]-oriented pattern (figure 1(g)). The formation of the additional QDs on the ridges accounts for the differences in the QD densities for different pattern orientations; in this case the QD densities at the bottom of the grooves are similar. With all other tested growth conditions the QD densities on the [011] and [010] patterns are equal and slightly larger than on the [01$\bar{1}$] pattern. We attribute the varying QD densities on the differently oriented patterns to the anisotropic diffusion of In atoms on the GaAs surface. Indium atoms exhibit a larger activation energy, and thus a larger diffusion length, on the GaAs(100) surface for migration in the [011] direction than in the [01$\bar{1}$] direction [16]. This impedes In diffusion from the ridges to grooves on the [01$\bar{1}$]-oriented pattern. However, this approach assumes a planar (100) surface and thus does not necessarily apply for the migration of In atoms on a patterned substrate. Moreover, as shown in figures 1(d), (e) and 3(f), the low QD density in the grooves of the [01$\bar{1}$] pattern is accompanied by the roughening of the groove sidewalls.

The AFM facet analysis (figures 6 and 7) revealed that the sidewall angle of the grooves decreased with increasing RGB thickness. This observation was also confirmed by the AFM line scans shown in figure 5. Furthermore, according to figure 7(b), the dominating facet of the grooves covered with a 60 nm thick RGB changes from (611)A to (411)A as the QD growth temperature is increased from 515 to 525 °C. We attribute this morphological change to minimization of the surface energy. The temperature ramp to 525 °C before QDC growth provides enough thermal energy for transformation of sidewall facets to (411)A, which has a surface energy comparable to low index GaAs surfaces [17]. As shown in figures 1(d), (e) and 3(f), the existence of (411)A facets is accompanied by roughening of the groove sidewalls. We suggest that In adatoms accumulate on the (411)A plane and crystallize as small InAs mounds, which is observed as sidewall roughening and leads to a lower QD density at the bottom of the grooves. This conclusion is supported by earlier findings by Kitada *et al* which showed that on patterned GaAs(100) surface with (411)A sidewalls, the migration of In adatoms is stronger upwards than downwards on the (411)A facet [18]. Furthermore, it has been shown that, under As-rich conditions, (411)A plane forms a nanoscale rough surface composed of (311)A and (511)A microfacets [19], which might launch the accumulation of In atoms on the groove sidewalls. Finally, it should be noted that the AFM-based facet analysis is not absolutely accurate for nanoscale patterns. Therefore, the determined sidewall angle may deviate

approximately 1° from the actual angle. Because of this experimental error, we cannot exclude the possibility of the occurrence of vicinal (100) surfaces, characterized by a high density of monolayer steps formed at the sidewalls. This kind of surface has been shown to be a favorable accumulation site for In atoms on shallow-patterned GaAs(100) [20]. However, the deviation of the sidewall angles, extracted from the facet analysis, is small enough to allow an unambiguous facet identification.

5. Conclusions

We studied the effects of QD growth temperature and RGB thickness on the formation of ordered QDCs on [011]-, [01$\bar{1}$]-, [010]-and [001]-oriented groove patterns. We demonstrated that equal QD densities can be obtained on patterns with different orientations by carefully tuning the growth parameters. Furthermore, we showed that the formation of grooves with (411)A sidewalls in the [01$\bar{1}$]-oriented pattern causes a reduction in the QD density and sidewall roughening. This was explained by the accumulation of In adatoms on the (411)A facets.

Acknowledgments

The research was carried out within the Academy of Finland project DAUNTLESS (decision no. 123951). TVH acknowledges financial support from the Finnish National Graduate School in Materials Physics, the Jenny and Antti Wihuri Foundation, and the Finnish Foundation for Technology Promotion. JT acknowledges the National Graduate School in Nanoscience (NGS-NANO) and the Pirkanmaa Regional Fund of the Finnish Cultural Foundation for the financial support. AS acknowledges funding from the Academy of Finland within project 138940.

References

[1] Grundmann M (ed) 2002 *Nano-Optoelectronics* (Berlin: Springer)

[2] Mohan A, Felici M, Gallo P, Dwir B, Rudra A, Faist J and Kapon E 2010 *Nat. Photon.* **4** 302

[3] Wang C-J, Lin L Y and Parviz B A 2005 *IEEE J. Sel. Top. Quantum Electron.* **11** 500

[4] Heydemeyer H, Müller C and Schmidt O G 2004 *Physica* E **23** 237

[5] Schedelbeck G, Wegscheider W, Bichler M and Abstreiter G 1997 *Science* **278** 1792

[6] Lee S C, Dawson L R, Malloy K J and Bruecka S R J 2001 *Appl. Phys. Lett.* **79** 2630

[7] Wang Z M, Holmes K, Mazur Y I and Salamo G J 2004 *Appl. Phys. Lett.* **84** 1931

[8] Hakkarainen T V, Schramm A, Tukiainen A, Ahorinta R, Toikkanen L and Guina M 2010 *Nanoscale Res. Lett.* **5** 1892

[9] Hakkarainen T V, Tommila J, Schramm A, Tukiainen A, Ahorinta R, Dumitrescu M and Guina M 2010 *Appl. Phys. Lett.* **97** 173107

[10] Braun W, Kaganer V M, Trampert A, Schönherr H-P, Gong Q, Nötzel R, Däweritz L and Ploog K H 2001 *J. Cryst. Growth* **227/228** 51

[11] Tadayyon-Eslami T, Kan H-C, Calhoun L C and Phaneuf R J 2006 *Phys. Rev. Lett.* **97** 126101

[12] Jones A K, Ballestad A, Li T, Whitwick M, Rottler J and Tiedje T 2009 *Phys. Rev.* B **79** 205419

[13] Tommila J, Tukiainen A, Viheriälä F, Schramm A, Hakkarainen T, Aho A, Stenberg P, Dumitrescu M and Guina M 2010 *J. Cryst. Growth* at press doi:10.1016/j.jcrysgro.2010.11.165

[14] Horcas I, Fernandez R, Gomez-Rodriguez J M, Colchero J, Gomez-Herrero J and Baro A M 2007 *Rev. Sci. Instrum.* **78** 013705

[15] Saito H, Nishi K, Sugou S and Sugimoto Y 1997 *Appl. Phys. Lett.* **71** 590

[16] Rosini M, Righi M C, Kratzer P and Magri R 2009 *Phys. Rev.* B **79** 075302

[17] Márquez J, Kratzer P, Geelhaar L, Jacobi K and Scheffler M 2001 *Phys. Rev. Lett.* **86** 115–8

[18] Kitada T, Wakejima A, Tomita N, Shimomura S, Adachi A, Sano N and Hiyamizu S 1995 *J. Cryst. Growth* **150** 487

[19] Hiroshi Y, Takumi Y and Yoshiji H 1995 *Japan. J. Appl. Phys.* **34** L1490–3

[20] Wang Zh M, Lee J H, Liang B L, Black W T, Kunets Vas P, Mazur Yu I and Salamo G J 2006 *Appl. Phys. Lett.* **88** 233102

Publication 4

T. V. Hakkarainen, A. Schramm, J. Tommila, and M. Guina, ”The effect of InGaAs strain reducing layer on the optical properties of InAs quantum dot chains grown on patterned GaAs(100)”, Journal of Applied Physics, vol 111, issue 1, 014306, 2012.

P4

The effect of InGaAs strain-reducing layer on the optical properties of InAs quantum dot chains grown on patterned GaAs(100)

T. V. Hakkarainen,[a] A. Schramm, J. Tommila, and M. Guina
Optoelectronics Research Centre, Tampere University of Technology, P.O. Box 692, FIN-33101 Tampere, Finland

(Received 17 October 2011; accepted 8 December 2011; published online 5 January 2012)

We report the influence of InGaAs strain-reducing layers on the optical properties of quantum dot chains grown on groove patterns oriented along the [011], [01-1], and [010] directions. The site-controlled InAs quantum dot chains were grown by molecular beam epitaxy on GaAs(100) substrates patterned by nanoimprint lithography. The InGaAs capping causes a redshift of photoluminescence, which depends on the groove orientations. Based on the analysis of the surface morphology before and after capping, we attribute this to variation of composition and effective thickness of the InGaAs layer in grooves with different orientations. Furthermore, we analyze the effect of the InGaAs cap thickness on the in-plane polarization anisotropy of the photoluminescence emission and show that the [01-1]-oriented quantum dot chains experience a significant increase of polarization anisotropy with increasing InGaAs cap thickness. The increase of polarization anisotropy is attributed to enhanced interdot coupling due to a reduction of the barrier height and piezoelectronic potential. © *2012 American Institute of Physics*.
[doi:10.1063/1.3675271]

I. INTRODUCTION

Self-assembled InAs/GaAs QDs (SAQD) obtained by the Stranski–Krastanov (SK) growth mode provide the homogeneity, density, and quality required for the fabrication of important photonic devices, such as laser diodes or detectors. However, more recent applications, such as single-photon emitters[1] or nanophotonics waveguides[2] require deterministic positioning of QDs. This site-controlled SK growth may target either to the formation of single-dot arrays, QD molecules, or quantum dot chains (QDC). The QD nucleation sites are typically defined by E-beam lithography,[3] focused ion beam implantation,[4] or Interference lithography.[5] Recently, we have shown that the combination of UV-nanoimprint lithography (UV-NIL) and molecular beam epitaxy (MBE) also is an effective method for the fabrication of site-controlled InAs single dots and QDCs.[6–8] However, site-controlled epitaxy of QDs introduces new parameters during the fabrication and thus, requires a precise optimization of growth conditions in order to achieve QD nucleation only in the pre-determined locations. This might lead to less freedom in adjusting other QD properties, such as emission wavelength.

In this paper we study the effect of $In_{0.1}Ga_{0.9}As$ capping on the optical properties of [011]-, [01-1]-, and [010]-oriented InAs QDCs in groove-like patterns fabricated on GaAs(100) using MBE and UV-NIL. Capping InAs/GaAs QDs with an InGaAs strain-reducing layer (SRL) is a well-known method for redshifting the emission wavelength of SAQDs grown on planar surface.[9–11] However, as far as we know, there are no reports on using InGaAs capping on QDs grown on a prepatterned substrates. In particular, for the QDCs it is worth understanding the influence of the anisotropic InGaAs SRL growth on the optical properties of QDs grown on grooves with different orientations.

II. EXPERIMENT

The investigated samples were prepared in three stages. The first stage was MBE growth of the lower part of the heterostructure; a 100 nm GaAs buffer, a 100 nm AlGaAs carrier confinement layer, and a 100 nm GaAs layer were deposited at 590 °C on 2″ n-GaAs(100) quarter substrates. In the second stage, the samples were ex situ patterned by UV-NIL. Four 10×10 mm^2 patterns with different groove orientations were processed on each quarter substrate. The grooves having a width, depth, and period of 90 nm, 20 nm, and 180 nm, respectively, were transferred onto the GaAs surface by dry etching. The details of the UV-NIL process and chemical cleaning prior to the regrowth are discussed in Ref. 7. In the final stage, the upper part of the heterostructure was grown by MBE. First, the chemically cleaned patterned templates were heat treated under arsenic background at 590 °C for 5 min. Then, the patterned surface was covered with a 60 nm GaAs regrowth buffer (RGB) at 490 °C and 2.2 monolayers InAs QDs grown at 515 °C. The QDs were capped with an $In_{0.1}Ga_{0.9}As$ SRL and a 20 nm GaAs layer at the same temperature. The thickness of the InGaAs SRL was 0 nm, 3 nm, or 8 nm, depending on the sample. After capping, the samples were heated to 590 °C for the growth of a 50 nm GaAs layer, a 50 nm AlGaAs carrier confinement layer, and a 20 nm GaAs capping layer. The samples with the above-mentioned layer structure were used for optical investigations. The SAQDs formed on a planar non-patterned area in the middle of each sample were used as a reference for the analysis of the optical properties of the QDCs Furthermore, we prepared

[a]Author to whom correspondence should be addressed. Electronic mail: teemu.hakkarainen@tut.fi.

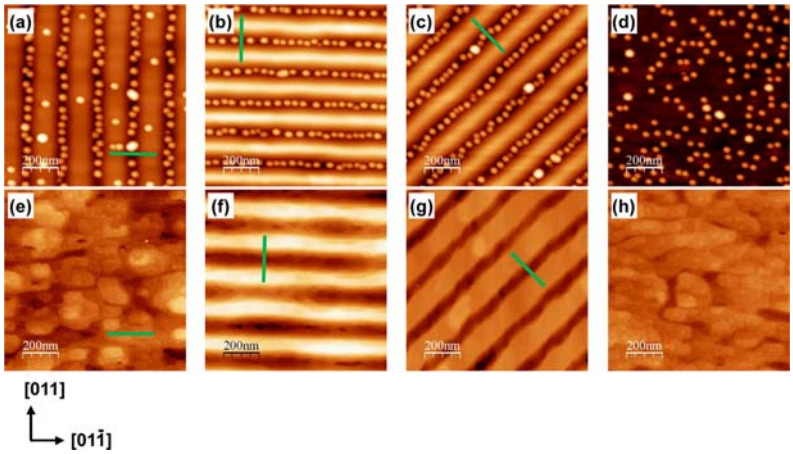

FIG. 1. (Color online) AFM pictures of [011]-, [01-1]-, and [010]-oriented QDCs and SAQDs in (a)–(d), respectively. (e)–(h) show the [011]-, [01-1]-, and [010]-oriented QDCs and SAQDs capped by 3 nm of InGaAs. The height scale in is 27 nm (a)–(d), 15 nm in (f) and (g), and 5 nm in (e) and (h).

a sample with uncapped QDs and samples with QDs covered only by 3 nm InGaAs or GaAs layer in order to study the evolution of the patterned surface in the capping process. The surface morphology of the uncapped QD samples and samples with QDs covered only with the 3 nm InGaAs or GaAs layers were investigated by atomic force microscopy (AFM).[12] Optical characterization was performed by room temperature PL (RT-PL) using excitation at 532 nm. Furthermore, the in-plane polarization anisotropy of the QDCs was analyzed by means of polarization-resolved PL measured at 30 K using excitation at 488 nm.

III. RESULTS AND DISCUSSION

Figure 1 presents AFM pictures of QDCs and SAQDs before and after capping with a 3 nm InGaAs SRL. As shown in Figs. 1(a)–1(c), the depth and shape of the grooves after RGB growth depends on their orientation; [011]-oriented grooves being the shallowest and [01-1]-oriented grooves the deepest. Lateral ordering of QDs in the bottom of the grooves is observed on all patterns. As shown in Fig. 1(a), a small number of QDs nucleate also on the ridges of the [011]-oriented pattern. The average height of the uncapped QDs shown in Figs. 1(a)–1(d) was found to be 12 nm for the SAQDs and for the QDCs with different orientations. The height of the additional QDs accumulated on the ridges of the [011]-oriented groove pattern exhibited average height of 10 nm. Furthermore, AFM analysis of the SAQDs grown on the planar area and QDCs grown in the grooves with different orientations showed similar lateral QD dimensions with a slight elongation along the [01-1] direction. However, the exact lateral size of the QDs could not be estimated from the AFM pictures due error caused by the AFM tip. The structural properties of QDCs grown on grooves with different orientations are discussed in detail elsewhere.[8] Figures 1(e)–1(h) illustrate the surfaces shown in Figs. 1(a)–1(d), respectively, after capping with 3 nm of InGaAs. The [011]-oriented grooves, shown in Fig. 1(e), are fully covered after capping with a 3 nm InGaAs SRL with a hardly visible underlying nanopattern, while the [01-1]- and [010]-oriented grooves (Figs. 1(f) and 1(g)) are still clearly visible after capping. The capped SAQDs, shown in Fig. 1(h), exhibit a typical morphology with [01-1]-elongated islands.[10] The surface morphology after capping with 3 nm GaAs layers (not shown) is similar to Figs. 1(e)–1(h) with the exception that pits are formed in the cap at the locations of the QDs. This is a typical feature for InAs QDs during GaAs capping due the increase of the Ga adatoms surface energy in the strain field of the InAs QDs.[14]

AFM line scans across the grooves after QD growth and after capping with 3 nm InGaAs or GaAs layers are shown in Fig. 2. The dashed line in Fig. 2(a), corresponding to the InGaAs capped [011]-oriented grooves, was placed vertically so that it is located 3 nm above the solid line when looking at the planar ridge of the pattern. Then we calculated the integral area between the solid and dashed curves, which is proportional to the volume of the SRL and QDs. The average QD size and density were similar in all samples. The line scans of all other capped surfaces were offset so that the volume of the capping layer and QDs matched the InGaAs capped [011]-oriented QDCs. A representative QD is added to each line scan to illustrate the depth and filling of the grooves with respect to the QD height. It should be noted that the QD width in Figs. 2(a)–2(c) is affected by the AFM scanning along the [0-11] direction. As shown in Fig. 2(a),

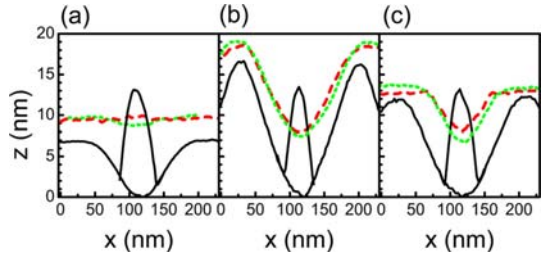

FIG. 2. (Color online) AFM line scans taken along the lines shown in Fig. 1. (a)–(c) represent [011]-, [01-1]-, and [010]-oriented grooves, respectively. The solid lines show the surface morphologies before capping and the dashed and dotted lines after capping with 3 nm InGaAs and GaAs layers, respectively. A line scan of a representative QD is added to each graph for illustrational purposes.

the InGaAs SRL forms a quantum wire-like structure on top of the [011]-oriented QDCs, while the SRL grows much more uniformly on the [01-1]-oriented QDCs. The capping behavior of the [010]-oriented QDCs is an intermediate form of the [011] and [01-1] orientations. It is obvious from Figs. 2(a)–2(c) that the cap layer thickness in the bottom of the grooves depends on their orientation. The anisotropic capping is due to the anisotropic adatom migration, which is stronger in the [01-1] than in the [011] direction, and the differences in the initial groove morphology.[13] Figures 2(a)–2(c) also show that, regardless of the groove orientation, the grooves are slightly deeper after GaAs capping than after InGaAs capping because the Ga adatoms tend to avoid the proximity of the InAs QDCs while In adatoms accumulate around and above the QDCs.[14]

Figure 3 presents normalized room temperature PL spectra for QDCs and SAQDs with InGaAs SRL thicknesses ranging from 0 nm to 8 nm. The insets show the GS peak shifts with respect to the InGaAs SRL thickness (t_{SRL}) normalized to the value corresponding to $t_{SRL} = 0$ nm. PL maps (not shown) revealed around 10 meV variations of GS peak energies over the 10×10 mm^2 patterns due to a temperature gradient during the growth. Therefore, the locations for the room temperature PL measurement were carefully chosen from around the center of the sample where the four patterns intersect with the planar reference area and similar growth conditions are provided for each pattern. This enabled accurate analysis of the effect of SRL thickness on the GS peak position for SAQDs and for QDCs with different orientation regardless of the non-uniformity. The [011]-oriented QDCs (Fig. 3(a)) experience a 16 meV redshift with $t_{SRL} = 3$ nm and a reduced redshift of 6 meV for $t_{SRL} = 8$ nm. The [01-1]-oriented QDCs (Fig. 3(b)) exhibit a 17 meV and 27 meV redshifts for $t_{SRL} = 3$ nm and $t_{SRL} = 8$ nm, respectively. Both the [010]-oriented QDCs (Fig. 3(c)) and SAQDs (Fig. 3(d)), show a redshift of 25 meV for $t_{SRL} = 3$ nm, while a slightly smaller redshift of 20 meV is observed in both samples for $t_{SRL} = 8$ nm. The [011]-, [01-1]-, and [010]-oriented QDCs and SAQDs seem to exhibit a saturating redshift with increasing t_{SRL}. For all other samples except [01-1]-oriented QDCs, the redshift is slightly reduced when t_{SRL} is increased to 8 nm. The PL results in Figs. 3(a)–3(c) are consistent with the observations from of the AFM line scans shown in Figs. 2(a)–2(c): The effective t_{SRL} in the grooves depends on their orientation. Thus, the GS PL peak shift, due to an increasing t_{SRL}, is different for each groove orientations. Furthermore, the InGaAs capping seems to have similar effects on the emission energy of the [010]-oriented QDCs and SAQDs, which suggests that these two totally different QD structures are capped in a similar manner. However, it should be noted that it is not only the effective t_{SRL} that affects the peak shift for QDCs with different orientations. We should also consider the accumulation of In atoms due to compressive strain of the QDs which causes decomposition of the SRL into In-rich and Ga-rich InGaAs alloys in the grooves and on the ridges, respectively. The decomposition is controlled by the adatom migration which is much stronger in the [01-1] than in the [011] direction. The In accumulation driven by anisotropic migration causes the formation of [01-1]-elongated islands above InGaAs-capped SAQDs (Fig. 1(h)).[14] In QDCs, the In accumulation is stronger if the QDC is aligned perpendicular to the preferential adatom migration direction, while it is weaker for parallel orientation. Therefore, we expect the In-content of the SRL around the QDCs to be higher for the [011] than for the [01-1] orientation leading to the different peak shifts with increasing t_{SRL}. In conclusion, the saturation of the redshift with increasing t_{SRL} is more rapid for the [011]- than for the [01-1]-oriented QDCs due to larger effective t_{SRL} and higher In content above the QDCs. The [010]-oriented QDCs are in 45° angle with respect to the preferential adatom migration direction, and therefore the formation of the In-rich alloy around the QDCs should be more or less similar to the case of SAQDs on a planar surface, which leads to similar PL peak shift as shown in Figs. 3(c) and 3(d). The anisotropic adatom diffusion during capping would explain the differences in the rapidness of the saturation of the redshift for SAQDs and QDCs with different orientations. Nevertheless, if the [011]-oriented QDCs have the highest In content of the SRL above the QDs they should also show the largest redshift, which is not the case in Fig. 3. We cannot, however, see the full trend of redshift from three data points, and therefore it is possible that the [011]-oriented QDCs experience their maximum redshift for $t_{SRL} < 3$ nm.

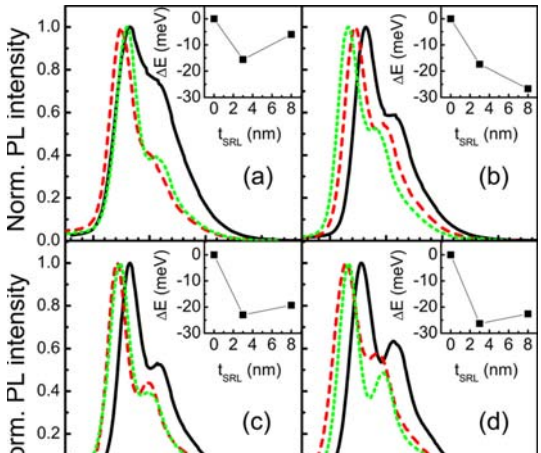

FIG. 3. (Color online) Room temperature PL spectra for [011]-, [01-1]-, and [010]-oriented QDCs and SAQDs in (a)–(d), respectively. The solid line represents QDs with 0 nm, the dashed line QDs with 3 nm, and the dotted line QDs with 8 nm InGaAs SRL. The inset in each graph shows the the GS peak shift (ΔE) with respect to the InGaAs SRL thickness (t_{SRL}).

In order to investigate the effect of SRL on the optical anisotropy we performed polarization-resolved PL measurement for the InGaAs-capped QDCs. In Ref. 6 we studied the in-plane polarization anisotropy of GS PL emission for GaAs-capped QDCs with different orientations and showed that it can be described by the interplay of *intrinsic* and *extrinsic* components. The intrinsic polarization anisotropy is

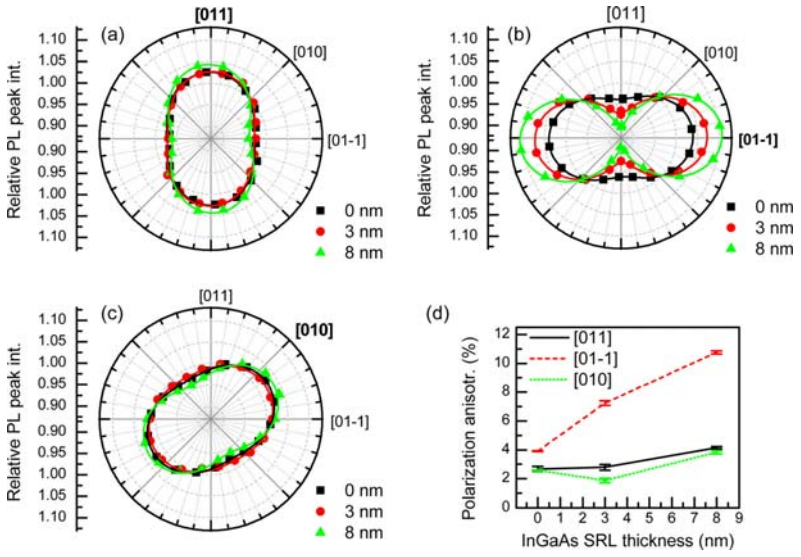

FIG. 4. (Color online) Ground state PL polarization for QDCs capped with 0 nm, 3 nm, and 8 nm SRLs. (a)–(c) represent [011]-, [01-1]-, and [010]-oriented QDCs, respectively. The solid lines represent sinusoidal fit curves. The graph in (d) shows the polarization anisotropy that is calculated from the minima and maxima of the fit curves, as a function of the InGaAs cap thickness for each QDC orientation.

caused by a typical slight QD shape elongation in the [01-1] direction. The extrinsic anisotropy, which tends to align along the QDC axis, can be caused by lateral interdot coupling and/or an anisotropic potential environment due to existence of a one-dimensional wetting layer.[3] Figures 4(a)–4(c) present the polarization anisotropy for the [011]-, [01-1]-, and [010]-oriented QDCs with respect to the SRL thickness. As shown in Fig. 4(a), the GS PL emission of the [011]-oriented QDCs is polarized along the QDC axis. The optical anisotropy is not affected by introduction of a 3 nm SRL, while a small increase of polarization is observed for the 8 nm SRL. For the [01-1]-oriented QDCs (Fig. 4(b)), we observe a significant increase of the polarization along the QDC axis with increasing SRL thickness. As shown in Fig. 4(c), also the [010]-oriented QDCs exhibit a small increase of polarization anisotropy when capped with 3 or 8 nm InGaAs SRLs. However, polarization anisotropy of the [010]-oriented QDCs is not oriented along the QDC axis because of the interplay of the intrinsic and extrinsic effects: The intrinsic anisotropy causes polarization in the [01-1] and the extrinsic anisotropy in the [010] direction. As a result, we observe optical anisotropy that is aligned in between the direction of the QD shape elongation and the QDC axis. The results of Figs. 4(a)–4(c) are summed up in Fig. 4(d) which shows the polarization anisotropy as a function SRL thickness.

As shown in Fig. 4, the effect of InGaAs-capping on the polarization anisotropy is much stronger for [01-1]-oriented QDCs than for the other two QDC orientations. In [01-1]-oriented QDCs, the increase of optical anisotropy in the [01-1] direction can be caused by either intrinsic or extrinsic effects. The InAs QD height is strongly reduced during capping with GaAs, while they tend to preserve their shape during InGaAs capping.[14] Considering this, it is unlikely that InGaAs capping would increase the intrinsic anisotropy so significantly. Therefore, the strong increase of the polarization anisotropy by InGaAs capping is most probably due to the extrinsic effects. As shown in Fig. 2, the growth of InGaAs SRL on the grooves is highly non-uniform especially on the [011]-oriented grooves where it forms a quantum-wire-like low bandgap channels along the QDC orientation. This anisotropic potential environment around the QDs could cause an expansion of the carrier wave functions along the QDC axis enhancing the oscillator strength, and consequently, an increase of the polarization anisotropy along the QDC chain. However, since the [011]-oriented QDCs are not much affected by InGaAs capping, this cannot explain the strong increase of optical anisotropy for the [01-1]-oriented QDCs. On the other hand, InGaAs capping reduces the QD confinement which may increase the lateral interdot coupling. From Fig. 1 we know that the average QD center-to-center distance in the [01-1]-oriented QDCs is clearly smaller than in the [011]- and [010]-oriented QDCs. Moreover, the shape elongation in the [01-1] direction will reduce the QD side-to-side distance in the [01-1]-oriented QDCs. Therefore, we expect the probability for interdot coupling to be higher for the [01-1] orientation than for the other two QDC orientations and it is even increased by surrounding the QDs with a low bandgap InGaAs barrier. Furthermore, the piezoelectric potential should be taken into account when discussing the carrier wave functions in strained InAs QDs.[15] The piezoelectric potential has positive (negative) maxima on the side of the QD in the [01-1] ([011]) direction. This fundamental property of strained QDs may limit electronic coupling in the [0-11]-oriented QDCs by forming a potential barrier in between the neighboring QDs along the chain. The introduction of an InGaAs SRL reduces the piezoelectric potential which explains the increase of optical anisotropy of the [01-1]-oriented QDCs with increasing SRL thickness. So far, evidence of lateral coupling has been reported for InAs quantum dot molecules[16] and strain-ordered InGaAs multilayer QDCs.[17] There are also numerous reports of vertical coupling of stacked InAs QDs.[18–20]

In order to get further evidence for the above-mentioned conclusions we have investigated the polarization anisotropy as a function of PL energy for the [01-1]-oriented QDCs with different SRL thicknesses. Figure 5 presents the PL spectra for polarizations parallel and perpendicular to the [01-1]-oriented QDCs (Figs. 5(a), 5(c), and 5(e)) as well as the optical anisotropy spectra calculated from the PL curves (Figs. 5(b), 5(d), and 5(f)). It should be noted that the peak positions in Figs. 5(a)–5(c) are not comparable with Fig. 3(b). A careful selection of the measurement location was not possible in the low temperature PL measurements and therefore the emission energies in Fig. 5 are affected by the non-uniformity over the large area pattern. Nevertheless, no detectable variations of the optical anisotropy were detected over the pattern area. The GaAs capped QDCs (Fig. 5(a) and 5(b)) exhibit a constant anisotropy at the GS PL peak energy, while there is a peak in the anisotropy on the high energy side of the first excited state (ES1). The introduction of a 3 nm InGaAs SRL (Fig. 5(c) and 5(d)) increases the GS PL anisotropy and a polaraization anisotropy peak begins to appear on the low energy side of the GS peak in Fig. 5(d). Furthermore, an anisotropy peak is still observed on the high energy side of the ES1 PL peak in Fig. 5(d). Finally, with an 8 nm SRL (Figs. 5(e) and 5(f)) we see a clear peak in the anisotropy (Fig. 5(f)) on the low energy side of the GS transition and the anisotropy peak around the ES1 PL energy has increased and shifted on the low energy side of the ES1 PL transition.

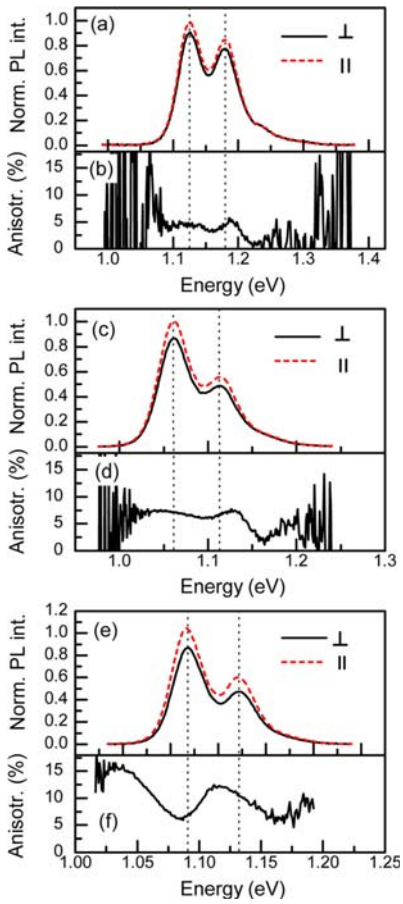

FIG. 5. (Color online) PL spectra measured from the [01-1]-oriented QDCs at 30 K for polarizations parallel and perpendicular to the QDC axis. In (a), (c), and (e) [01-1]-oriented QDCs capped with 0 nm, 3 nm, and 8 nm InGaAs SRLs, respectively. (b), (d), and (f) present the polarization anisotropy as a function of PL energy calculated from the spectra in (a), (c), and (e), respectively.

Bhattacharyya *et al*. have studied the effect of the QD shape elongation on the polarization anisotropy of InAs SAQDs.[21] According to their simulations, the polarization of the GS and ES PL emission is caused by a polarization-dependency of the oscillator strength due to the QD size asymmetry. A local maximum of the polarization anisotropy that is slightly offset from the ES1 PL peak energy is caused by an energy splitting of the *p* [011] and *p* [01-1] orbitals. However, the peak in the polarization anisotropy on the low energy side of GS PL peak observed in Fig. 5(d) and more strongly in Fig. 5(f) suggests energy splitting also in the GS. The energy splitting of the GS cannot be explained by an intrinsic polarization anisotropy. On the other hand, it is well known that the *s* state as well as the excited states split into bonding and antibonding states when two atoms or quantum dots bond to form a molecule. According to several theoretical[20,22] and experimental[23–25] reports, similar energy level splitting due to electronic coupling occurs also in the InAs/GaAs QD system. The observation of ground state splitting in the anisotropy spectrum would require that the oscillator strengths of the transitions corresponding to the bonding and antibonding states have different polarization-dependencies. Polarization anisotropy spectra similar to Fig. 5(f) with anisotropy peaking on the low energy side of the GS PL peak has been observed in a multilayer stack of vertically coupled InAs QDs by Yu *et al*.[26] who explain it by the fact that part of the QDs are coupled also in the lateral direction. These laterally coupled QDs exhibit stronger polarization anisotropy and lower transition energy than the rest of the QD population. This is probable also in the [0-11]-oriented QDCs since only part of the QDs in the chains have small enough nearest neighbor distance to allow lateral coupling. Therefore, we attribute the changes in the polarization anisotropy spectra of the [01-1]-oriented QDCs with increasing SRL thickness to enhanced interdot coupling between a part of QDs in the population. According to Refs. 18 and 19 electronic coupling in vertically stacked QDs results in a redshift and spectral narrowing of PL emission due to a delocalization of the carrier wave functions. In the case of InGaAs capped QDCs, the spectral narrowing caused by the electronic coupling is very difficult to detect because the coupling is enhanced by increasing the SRL thickness, which itself has an effect on the PL linewidths.[27] However, the contribution of the electronic coupling to the redshift would explain why the [01-1]-oriented QDCs experience the larges redshift of the investigated samples when capped with an 8 nm InGaAs layer.

IV. CONCLUSION

We have shown that the PL emission energy of InAs QDCs grown on a patterned GaAs(100) surface experience a redshift during $In_{0.1}Ga_{0.9}As$ capping. The amount of redshift is different for the [011]-, [01-1]-, and [010]-oriented QDCs because the effective thickness and composition of the SRL above the QDCs depends on their orientation with respect to the preferential adatom migration direction. Compared to SAQDs, the [011]-oriented QDCs were more sensitive, while the [01-1]-oriented QDCs were less sensitive to variation of the SRL thickness. The [010]-oriented QDCs, which are oriented in a 45° angle to the preferential adatom migration direction, behave similarly to the SAQDs during InGaAs capping. Furthermore, we showed that the [01-1]-oriented QDCs exhibit a strong increase of the polarization anisotropy with increasing SRL thickness, while the introduction of a SRL had only a marginal effect for the other QDC orientations. The strong increase of polarization anisotropy is attributed to enhanced interdot coupling due to a reduction of the barrier height and piezoelectronic potential.

ACKNOWLEDGMENTS

The authors thank Mr. Risto Ahorinta for the AFM pictures. The authors acknowledge financial support from Academy of Finland projects DAUNTLESS (decision number 123951) and DROPLET (decision number 138940). T.V. Hakkarainen acknowledges financial support from Finnish National Graduate School in Materials Physics, J. Tommila acknowledges the National Graduate School in Nanoscience (NGS-NANO) and the Pirkanmaa Regional Fund of the Finnish Cultural Foundation for the financial support.

[1]A. Mohan, M. Felici, P. Gallo, B. Dwir, A. Rudra, J. Faist, and E. Kapon, Nat. Photon. **4**, 302 (2010).
[2]C.-J. Wang, L. Y. Lin, and B. A. Parviz, IEEE J. Sel. Top. Quantum Electron. **11**, 500 (2005).
[3]S. Kiravittaya, H. Heidemeyer, and O. G. Schmidt, Physica E **23**, 253 (2004).
[4]M. Mehta, D. Reuter, A. Melnikov, A. D. Wieck, and A. Remhof, Appl. Phys. Lett. **91**, 123108 (2007).
[5]P. Alonso-González, L. González, Y. González, D. Fuster, I. Fernández-Martínez, J. Martín-Sánchez, and L. Abelmann, Nanotechnology **18**, 355302 (2007).
[6]T. V. Hakkarainen, J. Tommila, A. Schramm, A. Tukiainen, R. Ahorinta, M. Dumitrescu, and M. Guina, Appl. Phys. Lett. **97**, 173107 (2010).
[7]J. Tommila, A. Tukiainen, J. Viheriälä, A. Schramm, T. Hakkarainen, A. Aho, P. Stenberg, M. Dumitrescu, and M. Guina, J. Cryst. Growth **323**, 183 (2011).
[8]T. V. Hakkarainen, J. Tommila, A. Schramm, A. Tukiainen, R. Ahorinta, M. Dumitrescu, and M. Guina, Nanotechnology **22**, 295604 (2011).
[9]M. Hugues, M. Teisseire, J. -M. Chauveau, B. Vinter, B. Damilano, J. -Y. Duboz, and J. Massies, Phys. Rev. B **76**, 075335 (2007).
[10]F. Guffarth, R. Heitz, A. Schliwa, O. Stier, N. N. Ledentsov, A. R. Kovsh, V. M. Ustinov, and D. Bimberg, Phys. Rev. B **64**, 085305 (2001).
[11]D. Litvinov, H. Blank, R. Schneider, D. Gerthsen, T. Vallaitis, J. Leuthold, T. Passow, A. Grau, H. Kalt, C. Klingshirn, and M. Hetterich, J. Appl. Phys. **103**, 083532 (2008).
[12]I. Horcas, R. Fernandez, J. M. Gomez-Rodriguez, J. Colchero, J. Gomez-Herrero, and A. M. Baro, Rev. Sci. Instrum. **78**, 013705 (2007).
[13]H.-C. Kan, R. Ankam, S. Shah, K. M. Micholsky, T. Tadayyon-Eslami, L. Calhoun, and R. J. Phaneuf, Phys. Rev. B **73**, 195410 (2006).
[14]R. Songmuang, S. Kiravittaya, and O. G. Schmidt, J. Cryst. Growth **249**, 416 (2003).
[15]P. Moon, E. Yoon, W. Sheng, and J.-P. Leburton, Phys. Rev. B **79**, 125325 (2009).
[16]I. Shtrichman, C. Metzner, B. D. Gerardot, W. V. Schoenfeld, and P. M. Petroff, Phys. Rev. B **65**, 081303 (2002).
[17]Y. I. Mazur, V. G. Dorogan, E. Marega, Jr., G. G. Tarasov, D. F. Cesar, V. Lopez-Richard, G. E. Marques, and G. J. Salamo, Appl. Phys. Lett. **94**, 123112 (2009).
[18]G. S. Solomon, J. A. Trezza, A. F. Marshall, and J. S. Harris Jr., Phys. Rev. Lett. **76**, 952 (1996).
[19]N. N. Ledentsov, V. A. Shchukin, M. Grundmann, N. Kirstaedter, J. Böhrer, O. Schmidt, D. Bimberg, V. M. Ustinov, A. Yu. Egorov, A. E. Zhukov, P. S. Kop'ev, S. V. Zaitsev, N. Yu. Gordeev, Z. I. Alferov, A. I. Borokov, A. O. Kosogov, S. S. Ruvimov, P. Werner, U. Gösele, and J. Heydenreich, Phys. Rev. B **54**, 8743 (1996).
[20]L. R. C. Fonseca, J. L. Jimenez, and J. P. Leburton, Phys. Rev. B **58**, 9955 (1998).
[21]J. Bhattacharyya, S. Ghosh, S. Malzer, G. H. Döhler, and B. M. Arora, Appl. Phys. Lett. **87**, 212101 (2005).
[22]W. Jaskólski, M. Zieliński, G. W. Bryant, and J. Aizpurua, Phys. Rev. B **74**, 195339 (2006).
[23]G. Ortner, M. Bayer, A. Larionov, V. B. Timofeev, A. Forchel, Y. B. Lyanda-Geller, T. L. Reineche, P. Hawrylak, S. Fafard, and Z. Wasilewski, Phys. Rev. Lett. **90**, 086404 (2003).
[24]M. Bayer, P. Hawrylak, K. Hinzer, S. Fafard, M. Korkusinski, Z. R. Wasilewski, O. Stern, and A. Forchel, Science **291**, 451 (2001).
[25]G. Schedelbeck, W. Wegscheider, M. Bichler, and G. Abstreiter, Science **278**, 1792 (1997).
[26]P. Yu, W. Langbein, K. Leosson, J. M. Hvam, N. N. Ledentsov, D. Bimberg, V. M. Ustinov, A. Y. Egorov, A. E. Zhukov, A. F. Tsatsul'nikov, and Y. G. Musikhin, Phys. Rev. B **60**, 16680 (1999).
[27]S. Tonomura and K. Yamaguchia, J. Appl. Phys. **104**, 054909 (2008).

Publication 5

T. V. Hakkarainen, V. Polojärvi, A Schramm, J Tommila, and M Guina,"The Influence of Post-growth Annealing on the Optical Properties of InAs Quantum Dot Chains Grown on Pre-patterned GaAs(100)", Nanotechnology, vol 23, 115702, 2012.

Nanotechnology **23** (2012) 115702 (6pp) doi:10.1088/0957-4484/23/11/115702

The influence of post-growth annealing on the optical properties of InAs quantum dot chains grown on pre-patterned GaAs(100)

T V Hakkarainen, V Polojärvi, A Schramm, J Tommila and M Guina

Optoelectronics Research Centre, Tampere University of Technology, PO Box 692, FIN-33101 Tampere, Finland

E-mail: teemu.hakkarainen@tut.fi

Received 8 December 2011
Published 28 February 2012
Online at stacks.iop.org/Nano/23/115702

Abstract

We report on the effect of post-growth thermal annealing of [011]-, [01$\bar{1}$]-, and [010]-oriented quantum dot chains grown by molecular beam epitaxy on GaAs(100) substrates patterned by UV-nanoimprint lithography. We show that the quantum dot chains experience a blueshift of the photoluminescence energy, spectral narrowing, and a reduction of the intersubband energy separation during annealing. The photoluminescence blueshift is more rapid for the quantum dot chains than for self-assembled quantum dots that were used as a reference. Furthermore, we studied polarization resolved photoluminescence and observed that annealing reduces the intrinsic optical anisotropy of the quantum dot chains and the self-assembled quantum dots.

(Some figures may appear in colour only in the online journal)

1. Introduction

Thermal annealing has been widely used for improving material quality and for modifying the properties of semiconductor nanostructures, such as quantum wells (QW) [1] and quantum dots (QDs) [2]. Several studies have been reported on thermal annealing of self-assembled InAs/GaAs quantum dots (SAQDs) obtained by the Stranski–Krastanov (SK) growth mode [3–9]. These experiments have revealed that group III intermixing in the QD–matrix interface during thermal annealing leads to blueshift and narrowing of the optical emission as well as a reduction of the intersubband energy separation. These properties have allowed us to exploit thermal annealing, for example, for tuning the response of QD photodetectors that utilize ensembles of self-assembled QDs [10]. Furthermore, it has been demonstrated that post-growth RTA can be used to reduce the fine structure splitting in InAs SAQDs [11–13].

More recent QD related applications, such as entangled-photon emitters [14] or nanophotonic waveguides [15] require a deterministic positioning of QDs with precisely adjusted optical properties. Recently, we have shown that formation of site-controlled InAs single dots and quantum dot chains (QDCs) can be obtained by a combination of UV-nanoimprint lithography (UV-NIL) and molecular beam epitaxy (MBE) [16–18]. A precise optimization of growth conditions is necessary in the site-controlled epitaxy of QDs in order to achieve QD nucleation only in the pre-determined locations. This might lead to less freedom in precise adjustment of other QD properties, such as the emission wavelength, which is often required for specific applications. Different growth procedures such as high temperature capping [19] or indium flushing [20] have been used for blueshifting the emission of site-controlled QDs. This paper focuses on post-growth rapid thermal annealing (RTA) which is a potential method not only for modifying the spectral properties of site-controlled QDs but also for reducing the defects caused by the lithography process and subsequent growth on a non-planar surface. So far, only *in situ* annealing experiments, showing a reduction of exciton linewidths, have been reported on site-controlled QDs [21].

In particular, we study the influence of post-growth RTA on the optical properties of [011]-, [01$\bar{1}$]-, and [010]-oriented QDCs grown by MBE on UV-NIL patterned GaAs(100)

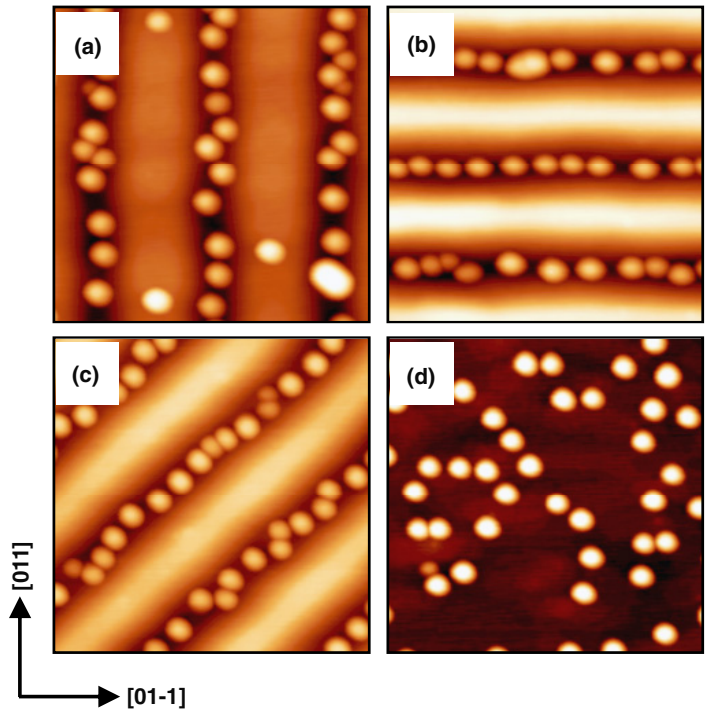

Figure 1. AFM pictures of [011]-, [01$\bar{1}$]-, and [010]-oriented QDCs and SAQDs in (a)–(d), respectively. The size of the pictures is 500 nm × 500 nm. The height scale is 20 nm in (a)–(c) and 12 nm in (d).

surfaces. We use room temperature, low temperature, and polarization resolved photoluminescence (PL) experiments for analyzing the effect of annealing on the optical properties of the QDCs and the surrounding GaAs matrix.

2. Experiment

The investigated samples were prepared by a three-stage procedure combining MBE and UV-NIL. First, a 100 nm GaAs buffer, a 100 nm AlGaAs cladding layer, and a 100 nm GaAs were deposited at 590 °C on quarters of 2″ n-GaAs(100) substrates by MBE. Then, the samples were *ex situ* patterned by UV-NIL. Four 10 mm × 10 mm groove patterns oriented along the [011], [01$\bar{1}$], [010], and [001] directions were processed on each sample. The grooves were 90 nm wide, 30 nm deep, and had a period of 180 nm. In the final stage, the patterned surface was covered with a 60 nm GaAs regrowth buffer at 490 °C before the deposition of 2.2 ML of InAs for the QDC formation at 515 °C. The QDCs were covered with a 20 nm GaAs layer grown at 515 °C. Subsequently, the sample temperature was increased to 590 °C for the growth of a 50 nm GaAs, a 50 nm AlGaAs layer, and a 20 nm GaAs capping layer. As a reference for the QDCs, we prepared also a SAQD sample on an unprocessed n-GaAs(100) substrate. The layer structure and growth conditions of the QDC and SAQD samples were identical. Furthermore, a sample with uncapped QDs was prepared for structural analysis of QDCs and SAQDs by atomic force microscopy (AFM). The UV-NIL process and chemical cleaning prior to regrowth are discussed in detail in [17]. The samples with [011]-, [01$\bar{1}$]-, and [010]-oriented QDCs are from now on referred to as QDC[011], QDC[01$\bar{1}$], and QDC[010], respectively.

The RTA process was performed for 2 × 2 mm^2 pieces of QDC[011], QDC[01$\bar{1}$], QDC[010], and SAQD reference sample. The samples were proximity-capped [22] and annealed on a silicon wafer, face up in N_2 atmosphere at a temperature of 720 °C. The temperature was controlled by an optical pyrometer. The annealing was performed in a sequence of 100 and 200 s steps. Room temperature PL (RT-PL) was measured from as-grown samples and after each annealing step using excitation at 532 nm and detection with an InGaAs photodiode. Furthermore, PL emission from the GaAs matrix and wetting layer was measured with a CCD detector before and after the annealing procedure. In order to further analyze the effect of RTA on the optical properties of the QDCs and SAQDs, we also measured low temperature PL (LT-PL) and polarization resolved PL (PR-PL) from each sample piece before and after the annealing sequence. The LT-PL and PR-PL measurement was performed at 30 K in a closed-cycle cryostat using excitation at 488 nm and detection with an InGaAs photodiode.

3. Results and discussion

The AFM pictures in figure 1 show the surface morphology of the uncapped QDCs and SAQDs. The QDCs grown in the

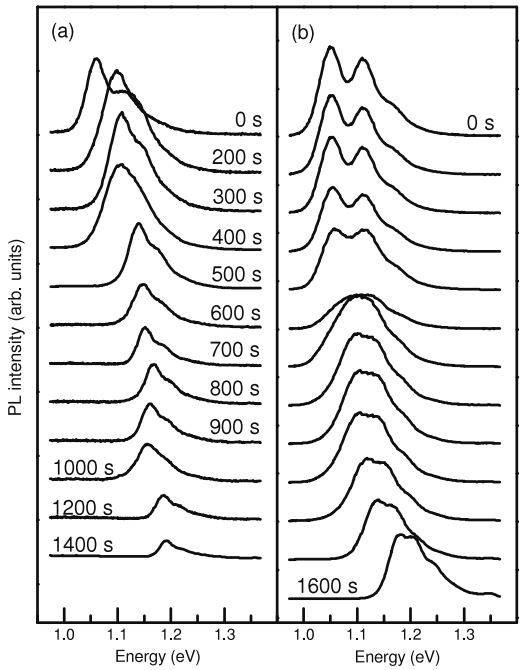

Figure 2. The evolution of RT-PL during post-growth RTA at 720 °C. (a) and (b) represent [01$\bar{1}$]-oriented QDCs and SAQDs samples, respectively.

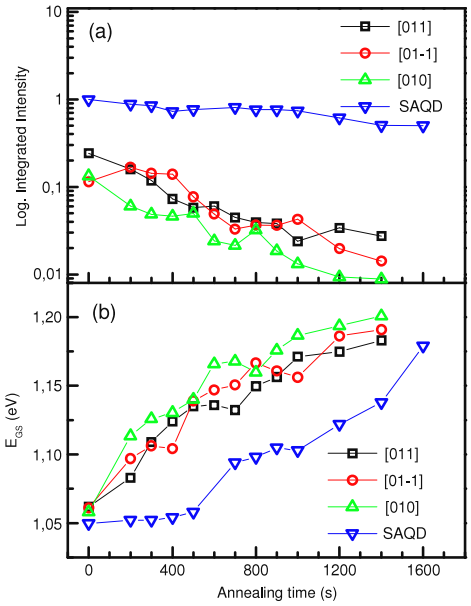

Figure 3. The evolution of PL properties of [011]-, [01$\bar{1}$]-, and [010]-oriented QDCs and SAQDs during post-growth RTA at 720 °C. (a) shows integrated PL intensity and (b) GS peak energy (E_{GS}) as a function of annealing time.

[011]-, [01$\bar{1}$]-, and [010]-oriented grooves are illustrated in figures 1(a)–(c) and the reference SAQDs in (d). The average QD height and density in the QDC and SAQD samples are 12 nm and about 1.3×10^{10} cm^{-2}. The structural and optical properties of the QDCs are reported in [16] and [18].

Figure 2 shows RT-PL spectra measured from the QDC [1] and SAQD reference samples before annealing and after each annealing step. The RT-PL intensity of the as-grown QDCs is 11–24% compared with the reference SAQDs [16]. The evolution of RT-PL during annealing is not shown for QDC[011] and QDC[010] because the results are similar to those of QDC[01$\bar{1}$]. Both samples (figure 2) show blueshift of the RT-PL emission with increasing annealing time. The ground state (GS) peak intensity of QDC[01$\bar{1}$] (figure 2(a)) increases during the first annealing steps. Further increase of annealing time causes a constant decrease of the GS peak intensity. As shown in figure 2(b), the SAQDs experience a constant decrease of the peak intensity during the whole annealing sequence. The evolution of integrated intensity and GS peak energy E_{GS} during the annealing sequence for all samples are illustrated in figure 3. The QDC samples and the SAQDs experience, as a general trend, a decay of the integrated intensity with increasing annealing time (figure 3(a)), but the decay is more rapid for the QDCs than for the SAQDs. All QDC samples show more or less similar sublinear blueshift of E_{GS} with increasing annealing time (as shown in figure 3(b)); E_{GS} increases rapidly in the beginning and starts to saturate towards the end of the annealing sequence. The E_{GS} of the QDCs after annealing at 720 °C for 1400 s is approximately 1.19 eV, which corresponds to a blueshift of 130 meV compared with the as-grown samples. Contrary to the QDCs, the SAQDs experience a superlinear increase of E_{GS} with increasing annealing time, resulting in a total blueshift of only 90 meV within 1400 s annealing. After 1400 s annealing the blueshift of the SAQDs is far from saturation, so we decided to perform one more 200 s annealing step for them to see if the E_{GS} of the SAQDs approaches that of the QDCs. As shown in figure 3(c), the total blueshift for the SAQDs reaches 120 meV after the additional annealing step.

The different annealing behavior of the QDCs and SAQDs can be understood in terms of defect mediated diffusion: due to the lithography process and subsequent MBE growth on a non-planar surface the QDC samples are expected to possess a higher density of point defects than the SAQD sample which causes a more a rapid intermixing at the QD–matrix interface. As a result, the blueshift of E_{GS} is more rapid for the QDCs than for the SAQDs in the beginning of the annealing sequence. Furthermore, the confinement of the holes and electrons in the QDs is reduced with increasing E_{GS}. This in turn causes the reduction of the RT-PL intensity for both QDCs and SAQDs.

In order to study the effect of annealing on the properties of GaAs matrices in the QDC and SAQD samples, we measured the RT-PL emission around the GaAs bandgap. Figures 4(a) and (b) show the wetting layer (WL) and GaAs RT-PL emission for the QDC[01$\bar{1}$] and SAQD samples before and after the annealing sequence. Corresponding spectra for QDC[011] and QDC[010] are not shown because the

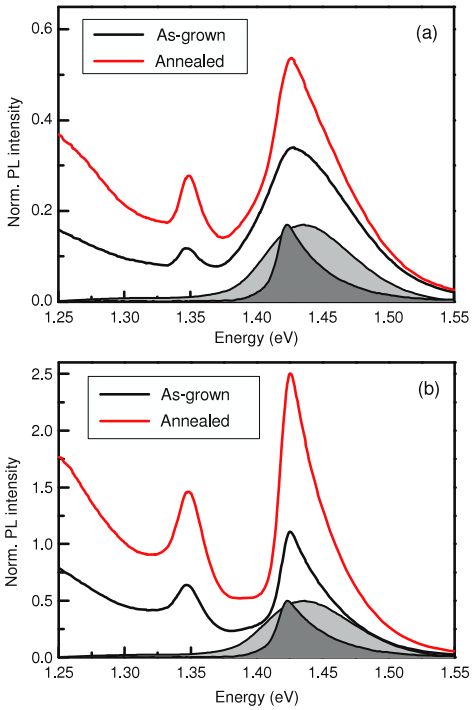

Figure 4. RT-PL spectra showing WL and GaAs emission from the QDC[01$\bar{1}$] and SAQD samples in (a) and (b), respectively. The spectra in (a) and (b) are normalized to the GaAs peak of the as-grown SAQDs. The light and dark gray peaks illustrate PL emission from n-GaAs substrate and MBE grown undoped GaAs, respectively.

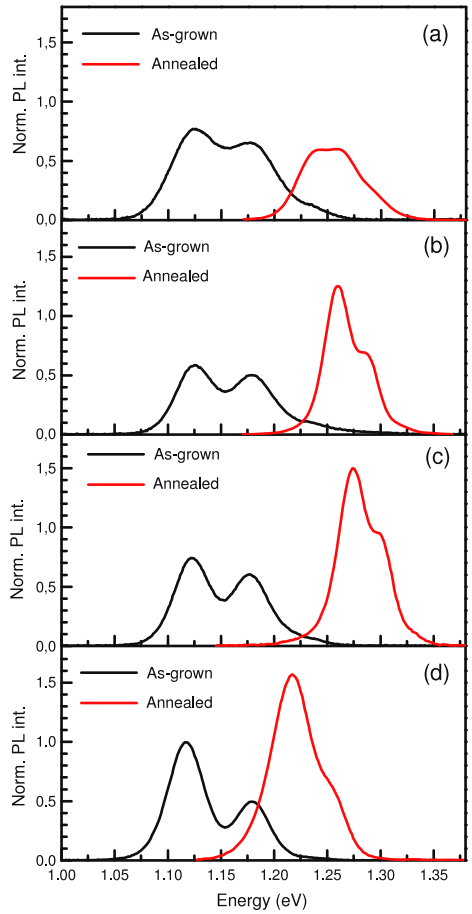

Figure 5. LT-PL spectra measured at 30 K before and after annealing. (a)–(d) represent QDC[011], QDC[01$\bar{1}$], QDC[010], and SAQD samples, respectively.

results are similar to those of QDC[01$\bar{1}$]. Both figures 4(a) and (b) show the same main features: the PL signal of the highest excited QD states on the low energy side of the spectra, the WL peak at 1.34 eV, and the GaAs peak at 1.43 eV. The intensities of all three contributions increase during annealing. The increased RT-PL from the QDs above 1.25 eV can be attributed to the blueshift of the QD spectrum. The increase in the WL intensity can be attributed either to reduced carrier confinement of the QDs due to QD–matrix intermixing and/or improvement of the matrix quality, i.e. annealing of the defects in the bulk and at the interfaces reducing non-radiative recombination. Therefore, the influence of annealing on the GaAs matrix PL requires careful consideration. As shown in figure 4(a), the GaAs peak measured from the as-grown QDC[01$\bar{1}$] sample is broad. After annealing it is narrower, more intense, and slightly redshifted. In order to explain these changes, we consider the contributions from both the undoped GaAs matrix and the underlying n-GaAs substrate. The light gray and dark gray peaks in figure 4(a) show RT-PL emission measured from a bare n-GaAs substrate and from an undoped MBE grown GaAs layer. A comparison of the shapes of these peaks with the GaAs peaks of the as-grown and annealed QDC[01$\bar{1}$] shows that most of the GaAs peak intensity measured from the as-grown QDC[0-11] originates from the n-doped substrate. The annealed sample shows a narrowed and slightly redshifted GaAs peak which suggests increased contribution from the undoped GaAs matrix. A quantitative analysis was performed by fitting a linear combination of the light gray and dark gray curves to the spectra measured from the as-grown and annealed QDC[01$\bar{1}$] samples. Approximately 23% of the GaAs peak intensity measured from the as-grown QDC[01$\bar{1}$] originates from the undoped GaAs matrix and 77% from the n-GaAs substrate. The corresponding figures for the annealed QDC[01$\bar{1}$] are 50% and 50%. This yields a 3.5-fold increase of the GaAs matrix contribution upon annealing, indicating a reduction of non-radiative defects in the matrix. The GaAs peaks of both as-grown and annealed SAQD samples are dominated by the emission from the undoped GaAs matrix, and therefore annealing has no clear influence on the peak shape or position. A comparison of peak intensities shows the SAQDs experience a 2.5-fold increase of the GaAs matrix PL in annealing. Compared to the SAQD reference sample, the

QDC samples experience a larger increase of GaAs matrix PL upon annealing, indicating a more pronounced reduction of non-radiative defects in the matrix.

The well-known effects of post-growth RTA on the optical properties of InAs SAQDs include blueshift, spectral narrowing, reduction of intersubband energy separation, and increase of low temperature PL intensity [5, 23]. The room temperature PL spectra (figure 2) showed a clear blueshift for both QDC samples and for the SAQD reference sample. In order to assess the other effects of annealing on the optical properties of QDCs we also measured low temperature PL spectra from as-grown and annealed QDC and SAQD samples. The results are shown in figure 5. The GS peak intensity of the as-grown QDC samples is approximately 60% compared with the SAQD reference. The annealed QDC[011], shown in figure 5(a), exhibits slightly reduced LT-PL intensity, while the LT-PL intensity of QDC[01$\bar{1}$], QDC[010], and SAQDs increases upon annealing. Furthermore, the LT-PL spectra in figures 5(a)–(d) show that annealing causes blueshift, spectral narrowing, and reduction of intersubband energy separation in all samples investigated. The low LT-PL intensity of the annealed QDC[011] could be due to a reduced number of the optically active QDs after the annealing process. This is supported by the fact that the spectrum of the annealed QDC[011] is more saturated than the spectra of annealed QDC[01$\bar{1}$], QDC[010], or SAQD, although all investigated samples have similar QD densities [13]. Excluding the reduction of LT-PL intensity in the QDC[011], the effect of post-growth RTA on the LT-PL emission from the QDC samples is similar to what has been reported for SAQDs [5, 23].

In order to investigate the effect of annealing on the optical anisotropy we performed polarization resolved PL measurement for the as-grown and annealed QDCs and SAQDs. The in-plane polarization anisotropy of GS PL emission can be described by an interplay of intrinsic and extrinsic components [16]. The intrinsic polarization anisotropy is caused by the typical slight QD shape elongation in the [01$\bar{1}$] direction [24] and piezoelectric asymmetry [25] between the [011] and [01$\bar{1}$] directions. The extrinsic anisotropy, which tends to align along the QDC axis, can be caused by lateral interdot coupling [26] and/or an anisotropic potential environment, for example, due to the existence of a one-dimensional wetting layer [27]. Figure 6 shows the GS peak optical anisotropy for the as-grown and annealed QDCs and SAQDs. The as-grown QDC[011] (figure 6(a)) exhibits optical anisotropy that is oriented along the QDC axis. The optical anisotropy of QDC[011] increases during annealing. Compared with the as-grown QDC[011], the optical anisotropy of the as-grown QDC[01$\bar{1}$] (figure 6(b)) is larger because both intrinsic and extrinsic components are oriented along the [01$\bar{1}$] direction. However, the optical anisotropy of QDC[01$\bar{1}$] decreases upon annealing. As shown in figure 6(c), the as-grown QDC[010] shows an optical anisotropy aligned in between the [010] and [01$\bar{1}$] directions. This is caused by the interplay of intrinsic and extrinsic components that are oriented along the [01$\bar{1}$] and [010] directions, respectively. The annealed QDC[010] shows a slightly increased anisotropy that has rotated towards the [010] directions. The SAQDs (figure 6(d)) show a slight anisotropy along the [01$\bar{1}$] direction which is reduced upon annealing.

The effect of annealing on the optical anisotropy of the QDCs and SAQDs can be understood in terms of a reduction of the intrinsic anisotropy. In the case of QDC[011] the reduction of the intrinsic anisotropy causes an increase in the overall anisotropy because it is oriented perpendicular to the QDC axis. For the QDC[01$\bar{1}$] we observe an opposite effect because the intrinsic anisotropy is oriented along the QDC axis. In QDC[010], the contribution of the extrinsic anisotropy along the [010] direction is emphasized as the intrinsic anisotropy along the [01$\bar{1}$] direction decreases, and therefore we observe the rotation of the optical anisotropy towards the [010] direction. However, the increase of the overall optical anisotropy, in addition to the rotation of the polarization, observed for QDC[010] indicates that the extrinsic component has also increased during annealing. It should be noted that annealing may have increased the extrinsic anisotropy in QDC[011] and QDC[01$\bar{1}$] as well, but it cannot be assessed from figure 6 because the extrinsic and intrinsic components are aligned parallel/perpendicular to each other. The reduction of the intrinsic anisotropy in post-growth RTA can be attributed to two effects: (i) a reduction of the elastic strain due to the QD–matrix intermixing during post-growth RTA [28], and (ii) a decrease of the relative QD size anisotropy due to a uniform increase of the QD size in all directions [4], the latter of which may also increase interdot coupling in QDCs enhancing the extrinsic anisotropy.

4. Conclusions

We have shown that [011]-, [01$\bar{1}$]-, and [010]-oriented QDCs grown by MBE on UV-NIL patterned GaAs(100) experience a blueshift of PL emission, spectral narrowing, a reduction of intersubband energy separation, and an increase in LT-PL intensity in post-growth RTA. These features were shown to be similar in QDCs and SAQDs grown on unprocessed substrates. However, the blueshift is more rapid for the QDCs than for the SAQDs, indicating more pronounced QD–matrix intermixing during the annealing process. This is attributed to a higher density of defects in the GaAs matrix due to the patterning process and subsequent growth on a non-planar surface. Furthermore, we have shown that the RT-PL intensity of the GaAs matrix in the QDC samples experiences a 3.5-fold increase, compared to a 2.5-fold increase for the SAQD reference sample during annealing which suggests a more pronounced reduction of non-radiative defects in the QD surroundings. PR-PL measurements revealed that the intrinsic optical anisotropy of both QDCs and SAQDs decreases upon annealing, which is attributed to a reduction of elastic strain and QD size anisotropy.

Acknowledgments

The authors thank Mr Risto Ahorinta for the AFM pictures and the financial support from the Academy of

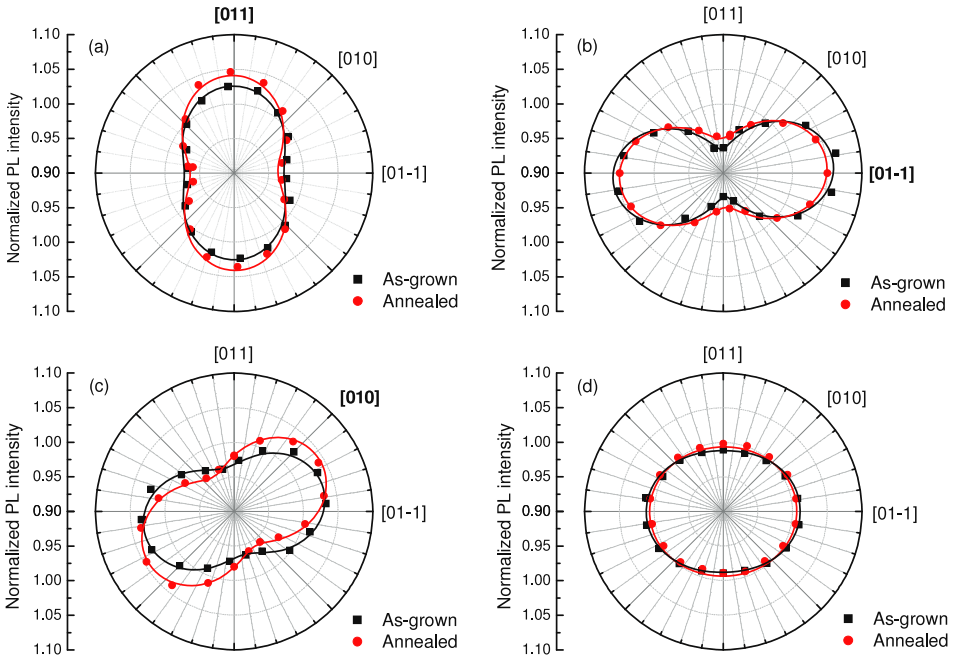

Figure 6. Ground state PL polarization measured at 30 K before and after RTA for QDC[011] (a), QDC[01$\bar{1}$] (b), QDC[010] (c), and SAQDs (d).

Finland projects DAUNTLESS (decision number 123951) and DROPLET (decision number 138940). T V Hakkarainen acknowledges financial support from the Finnish National Graduate School in Materials Physics, J Tommila acknowledges the National Graduate School in Nanoscience (NGS-NANO) and the Pirkanmaa Regional Fund of the Finnish Cultural Foundation for the financial support.

References

[1] Zory P S (ed) 1993 *Quantum Well Lasers* (New York: Academic)
[2] Grundmann M (ed) 2002 *Nano-Optoelectronics* (Berlin: Springer)
[3] Leon R, Kim Y, Jagadish C, Gal M, Zou J and Cockayne D J H 1996 *Appl. Phys. Lett.* **69** 1888
[4] Kosogov A O *et al* 1996 *Appl. Phys. Lett.* **69** 3072
[5] Malik S, Roberts C, Murray C and Pate M 1997 *Appl. Phys. Lett.* **71** 1987
[6] Lobo C, Leon R, Fafard S and Piva P G 1998 *Appl. Phys. Lett.* **72** 2850
[7] Xu S J, Wang X C, Chua S J, Wang C H, Fan W J, Jiang J and Xie X G 1998 *Appl. Phys. Lett.* **72** 3335
[8] Leon R, Fafard S, Piva P G, Ruvimov S and Liliental-Weber Z 1998 *Phys. Rev.* B **58** R4262
[9] Fafard S, Wasilewski Z R, Allen C Ni, Picard D, Spanner M, McCaffrey J P and Piva P G 1999 *Phys. Rev.* B **59** 15368
[10] Aivaliotis P, Zibik E A, Wilson L R, Cockburn J W, Hopkinson M and Airey R J 2007 *Appl. Phys. Lett.* **91** 143502
[11] Ellis D J P, Stevenson R M, Young R J, Shields A J, Atkinson P and Ritchie D A 2007 *Appl. Phys. Lett.* **90** 011907
[12] Seguin R *et al* 2006 *Appl. Phys. Lett.* **89** 263109
[13] Langbein W, Borri P, Woggon U, Stavarache V, Reuter D and Wieck A D 2004 *Phys. Rev.* B **69** 161301(R)
[14] Mohan A, Felici M, Gallo P, Dwir B, Rudra A, Faist J and Kapon E 2010 *Nature Photon.* **4** 302
[15] Wang C-J, Lin L Y and Parviz B A 2005 *IEEE J. Sel. Top. Quantum Electron.* **11** 500
[16] Hakkarainen T V, Tommila J, Schramm A, Tukiainen A, Ahorinta R, Dumitrescu M and Guina M 2010 *Appl. Phys. Lett.* **97** 173107
[17] Tommila J, Tukiainen A, Viheriälä J, Schramm A, Hakkarainen T, Aho A, Stenberg P, Dumitrescu M and Guina M 2011 *J. Cryst. Growth* **323** 183
[18] Hakkarainen T V, Tommila J, Schramm A, Tukiainen A, Ahorinta R, Dumitrescu M and Guina M 2011 *Nanotechnology* **22** 295604
[19] Yamaguchi K, Saito Y and Ohtsubo R 2002 *Appl. Surf. Sci.* **190** 212
[20] Sasakura H, Kayamori S, Adachi S and Muto S 2007 *J. Appl. Phys.* **102** 013515
[21] Helfrich M *et al* 2011 *J. Cryst. Growth* **323** 187
[22] Babinski A, Jasinski J, Bozek R, Szepielow A and Baranowski J 2001 *Appl. Phys. Lett.* **79** 2576
[23] Hsu T M, Lan Y S, Chang W H, Yeh N T and Chyi J I 2000 *Appl. Phys. Lett.* **76** 691
[24] Songmuang R, Kiravittaya S and Schmidt O G 2003 *J. Cryst. Growth* **249** 416
[25] Bester G, Zunger A, Wu X and Vanderbilt D 2006 *Phys. Rev.* B **74** 081305
[26] Moon P, Yoon E, Sheng W and Leburton J-P 2009 *Phys. Rev.* B **79** 125325
[27] Wang X, Wang Zh M, Liang B, Salamo G J and Shih C-K 2006 *Nano Lett.* **6** 1847
[28] Santoprete R, Kratzer P, Scheffler M, Capaz R B and Koiller B 2007 *J. Appl. Phys.* **102** 023711

Publication 6

T. V. Hakkarainen, A. Schramm, E. Luna, J. Tommila, M. Guina, "Temperature dependence of photoluminescence for site-controlled InAs/GaAs quantum dot chains", Journal of Crystal growth, vol 378, pp. 470-474, 2013.

Available online at http://dx.doi.org/10.1016/j.jcrysgro.2012.12.099

P6

Temperature dependence of photoluminescence for site-controlled InAs/GaAs quantum dot chains

T. V. Hakkarainen[a,*], A. Schramm[a], E. Luna[b], J. Tommila[a], M. Guina[a]

[a]*Optoelectronics Research Centre, Tampere University of Technology, Tampere, Finland.*

[b]*Paul-Drude-Institut für Festkörperelektronik, Berlin, Germany*

Abstract

We study the temperature dependence of the photoluminescence (PL) from InAs quantum dot chains (QDC) grown by MBE on [011]- and [01 $\bar{1}$]-oriented UV nanoimprint lithography processed groove patterns. We observe an increase of PL intensity from the [01 $\bar{1}$]-oriented QDCs within the temperature range from 20-70 K, which is attributed to thermally activated carrier transport from small quantum dots accumulated on the sidewalls of the [01 $\bar{1}$]-oriented grooves to the quantum dots at the bottom of the groove. We utilize a rate equation model to quantitatively analyze the carrier transfer mechanism. Furthermore, we show that the defect related carrier loss mechanism, which accounts for weak PL quenching at low temperatures, is similar for QDCs and self-assembled quantum dots (SAQD) that were used as a reference. The carrier loss mechanism that causes the rapid quenching of SAQD PL at high temperatures is identified as exciton escape, while for the QDCs it is either single carrier escape or escape of uncorrelated electron-hole pairs. This result reveals a significant difference in the carrier dynamics of site-controlled QDCs and SAQDs.

Keywords

A1. Nanostructures; A1. Low dimensional structures; A3. Molecular beam epitaxy; B2. Semiconducting III-V materials

*Corresponding author

Address: Optoelectronics Research Centre, Tampere University of Technology,

Korkeakoulunkatu 3, 33720 Tampere, Finland

Email address: Teemu.Hakkarainen@tut.fi

Telephone: +358401981056

1. Introduction

Lateral ordering of InAs/GaAs quantum dots (QDs) [1] is beneficial for several emerging applications, such as entangled-photon emitters [2] or nanophotonic waveguides [3], in which a precise positioning of the QDs with respect to the surrounding structure is required. The positioning of InAs/GaAs QDs can be achieved by the *site-controlled Stranski-Krastanov growth*, in which the nucleation sites of the QDs are most commonly defined by E-beam lithography [4], focused ion beam implantation [5], or interference lithography [6]. More recently, we have shown that

molecular beam epitaxy (MBE) combined with UV nanoimprint lithography (UV-NIL) is a precise and cost-effective tool for the deterministic positioning of InAs QDs as quantum dot chains (QDCs) [7,8] and as arrays of single quantum dots [9,10].

In this paper we focus on the temperature dependency of the photoluminescence (PL) from $[01\bar{1}]$- and [011]-oriented InAs QDCs grown by MBE on UV-NIL prepared groove patterns. Such experiments have been widely used for identifying the carrier escape and PL quenching mechanisms of self-assembled quantum dots (SAQD) [11,12] as well as for studying carrier transfer between different QD families in bimodal [13] or bilayer [14] QD distributions. The purpose of the work presented in this paper is to determine the influence of the site-controlled growth on PL quenching mechanisms as well as to study the thermally activated carrier transfer between QDCs and small QDs accumulated on the sidewalls of the $[01\bar{1}]$-oriented grooves.

2. Experiment

The preparation of the investigated sample involved a three-stage procedure. First, a 100 nm GaAs buffer, a 100 nm AlGaAs carrier confinement layer, and a 100 nm GaAs were deposited at 590°C on n-GaAs(100) substrate by MBE. In the second step the sample was ex situ patterned by UV-NIL [9]. The lithography pattern consisted of 90 nm wide and 30 nm deep grooves with a period of 180 nm. The orientation of the grooves was along the $[01\bar{1}]$ direction on one side of the pattern and along the [011] direction on the other. Chemical cleaning and oxide removal was performed for the sample after the patterning process [9]. In the regrowth step, the patterned surface was first covered with a 60 nm GaAs regrowth buffer at 490°C followed by deposition of 2.2 monolayers of InAs at 515°C for QDC formation. The QDCs were capped with a 20 nm GaAs layer at 515°C. After that, the sample temperature was elevated to 590°C for the growth of 50 nm GaAs, a 50 nm AlGaAs layer, followed by a 20 nm GaAs capping layer. The growth rates for GaAs, AlGaAs, and InAs were 0.6 μm/h, 1.2 μm/h, and 0.05 μm/h, respectively. From now on the QDCs grown on the $[01\bar{1}]$- and [011]-oriented grooves are referred to as QDC$[01\bar{1}]$ and QDC[011], respectively. For reference purposes we prepared also a sample with SAQDs grown on unprocessed n-GaAs substrate. This reference sample had the same layer structure and growth conditions as the QDC sample.

Transmission electron microscopy (TEM) investigations were carried out for GaAs-capped QDCs and SAQDs using a Jeol JEM 3010 microscope operating at 300 kV, equipped with a GATAN slow-scan charge-coupled device camera. Cross-sectional TEM foils were prepared in the [011] and $[01\bar{1}]$ projections, using mechanical thinning followed by Ar-ion milling. The temperature-dependent PL (TD-PL) measurement was carried out in a closed–cycle He-cryostat at the temperature range from 20K to 300K. The sample was excited with the 488 nm line of an Ar-ion laser. The TD-PL measurements were carried out with excitation powers of 5e-5 W, 5e-4 W, and 5e-3 W focused on a 300 μm spot. The

PL signal was detected with a 0.5 m monochromator and a Peltier-cooled InGaAs detector. Micro-photoluminescence (μPL) spectra were measured in a closed-cycle cryostat cooled down to 5 K. The sample was excited through a microscope objective (NA=0.82) by the 405 nm line of a GaN diode laser. The μPL signal was collected with the same objective and detected with a 0.75 m spectrometer and Peltier-cooled CCD camera. The lateral resolution of the μPL setup is approximately 500 nm.

3. Results and Discussion

Figure 1(a) and (b) show cross-sectional dark field TEM (DFTEM) micrographs of QDC[01$\bar{1}$] and QDC[011], respectively. The DFTEM micrographs were obtained using the chemical sensitive **g**=(200) imaging conditions. The cross-sectional view of QDC[01$\bar{1}$] along its axis reveals that: (i) the wetting layer (WL) has covered the whole patterned surface, (ii) the QDCs are formed in the grooves of the pattern, and (iii) small QDs (SQDs) are nucleated on the (n11)A facetted sidewalls [8] of the grooves. A similar $\mathbf{g}_{200}$ DFTEM micrograph of QDC[011] (Fig.1(b)) shows the same features except that the grooves are shallower and their sidewalls are less clearly facetted. Furthermore, no SQDs are observed in QDC[011] , but some QDs are nucleated on the flat (100) ridges of the groove pattern. The absence of SQDs on the sidewalls of the [011]-oriented grooves is probably due to the groove morphology, but we cannot exclude the effect of the facet type, which is (n11)B for [011]-oriented grooves [8]. According to the atomic force microscopy (AFM) analysis of uncapped QDCs presented in Ref. [8], the QD density in QDC[01$\bar{1}$], QDC[011], and in the SAQD sample is around 1.5×10^{10} cm^{-2}. A comparison of the WL morphologies in Figs. 1(a) and (b) with the AFM results [8] shows that the groove depth and the sidewall angle are preserved during capping.

Figure 2(a)-(c) present TD-PL results for QDC[01$\bar{1}$], QDC[011], and SAQDs, respectively. The insets in Figure 2 show PL spectra measured at 20K using three different excitation powers. With the two smallest excitation powers (5e-5 W and 5e-4 W) only the ground state (GS) emission is observed. When the excitation power is increased to 5e-3 W the GS emission saturates and a peak of the first excited state is observed. It should be noted that the emission from the QDs accumulated on the ridges of the [011]-oriented grooves overlaps with the PL peaks of the QDC[011]. Therefore, the emission from these QDs is observed as a broadening of the PL peaks of QDC[011], not as separate peaks. The temperature dependency of the GS peak PL intensity was determined for QDC[01$\bar{1}$], QDC[011], and SAQDs by fitting Gaussian peaks to the PL spectra measured at each temperature point within the range from 20K to 300K. The results are shown in the main plots of Fig. 2. As shown in Fig. 2(a), QDC[01$\bar{1}$] exhibits an increase of PL intensity within the temperature range from 20 K to 70 K. This effect is clearly observed with the two smallest excitation powers, but nearly vanishes when the excitation power is increased to the level that saturates the GS emission. As shown in Fig. 2(b) and (c), QDC[011] and the SAQDs exhibit a slow PL quenching below 100 K and a rapid PL quenching at higher

temperatures, which suggests a bi-exponential temperature-dependency of the PL intensity. However, no increase of PL intensity with increasing temperature is observed for QDC[011] and the SAQDs, where no SQDs were observed in the DFTEM micrographs (Fig. 1(a), (b)). Since no PL was detected from the SQDs in QDC[01$\bar{1}$] with the InGaAs photodiode, we employed the μPL setup equipped with a CCD camera to measure the PL emission around the WL peaks of QDC[01$\bar{1}$], QDC[011], and SAQDs. As shown in Fig. 3, all samples exhibit WL emission at around 1.43eV. The WL peaks show fine structure which is attributed to monolayer fluctuations. On the low energy side of all spectra in Fig. 3 we observe the continuous ensemble PL emission from the highest excited states of QDCs or SAQDs. Notice that the μPL spectra of QDC[01$\bar{1}$] exhibits narrow emission lines located at energies slightly below the WL peak, while such features are not observed for QDC[011] or SAQDs. These narrow emission lines arise from excitons confined to the SQDs. Therefore, it suggests that the most probable cause for the increase of PL intensity observed for QDC[01$\bar{1}$] is carrier transfer [15-18] from the SQDs to the QDs accumulated in the bottom of the grooves. Such thermally activated process can be modeled with coupled rate equations. Thus, we propose a rate equation based model for a four-state system consisting of the GaAs barrier, the WL, and the GS of the QDCs and SQDs. The scheme for the rate equation model is presented in Fig. 4. In our model we assume:

1) We consider carrier populations in the WL, QDCs, and SQDs, which are designated by n_1, n_2, and n_3, respectively.

2) The carriers are generated from the GaAs barrier to the WL at rate g.

3) Carriers in the WL are captured to the QDCs and SQDs with probabilities c_2 and c_3, respectively, or are thermally excited to the GaAs barrier at rate $\alpha_1=e_1\exp(-E_1/kT)$.

4) The carriers in the QDCs either recombine at rate r_2 or escape to the WL at rate $\alpha_2=e_2\exp(-E_2/kT)$.

5) The carriers in the SQDs either recombine at rate r_3 or escape to the WL at rate $\alpha_3=e_3\exp(-E_3/kT)$.

6) Radiative recombination in the WL is not taken into account, because the TD-PL measurement was carried out with low or moderate excitation power.

7) The mechanism of the carrier transfer is assumed to be thermal emission from the SQDs and recapture to the QDCs. Possibility of nonresonant multiphonon-assisted tunneling [17] is excluded for the sake of simplicity.

The rate equations of the four-state system shown in Fig. 4 are the following:

$$\begin{aligned}
\frac{dn_1}{dt} &= g - n_1\alpha_1 - n_1c_2 + n_2\alpha_2 - n_1c_3 + n_3\alpha_3 \\
\frac{dn_2}{dt} &= n_1c_2 - n_2\alpha_2 - n_2r_2 \\
\frac{dn_3}{dt} &= n_1c_3 - n_3\alpha_3 - n_3r_3
\end{aligned} \tag{1}$$

The temperature dependency of PL from QDC[01$\bar{1}$] is obtained from the steady state solution of the coupled rate

equations, which is as follows.

$$I_{PL}(T) = n_2 r_2 = \frac{g}{\frac{(\alpha_2 + r_2)}{r_2 c_2}\left(\alpha_1 + c_2 + c_3 - \frac{\alpha_3 c_3}{\alpha_3 + r_3}\right) - \frac{\alpha_2}{r_2}} \quad (2)$$

Since no SQDs were observed in QDC[011] or in the SAQD sample (Fig. 1(b) and (c)), the temperature dependency of their PL intensity can be obtained from Eq. (2) by assuming a zero carrier capture probability from the WL to the SQDs, *i.e.* c_3=0. By doing so we get

$$I_{PL}(T) = n_2 r_2 = \frac{g}{1 + \frac{\alpha_1 \alpha_2}{r_2 c_2} + \frac{\alpha_1}{c_2}}, \quad (3)$$

which corresponds to the state solution for a three-level system [18] consisting of the GaAs barrier, the WL, and the QDCs.

The temperature dependency of the PL intensity for QDC[01$\bar{1}$] (Fig. 2(a)) was fitted according to Eq. (2) which takes into account the carrier transfer from the SQDs. In the cases QDC[011] and SAQDs (Fig. 2(b) and (c)) the fitting was carried out according to Eq. (3) due to the absence of the SQDs. The activation energies of the carrier escape channels obtained as fitting parameters are shown in Table 1. The activation energies were determined for excitation powers of 5e-5 W, 5e-4 W, and 5e-3W. The values in Table 1 are the averages of the values obtained using different excitation powers for each sample and the error margins were estimated from the difference of the largest and smallest value.

As shown in Table 1, the activation energy E_1, corresponding to the carrier escape from the WL, is around 14-22 meV for both QDCs and SAQDs. Comparison of the values of E_1 with the separation of the WL and GaAs PL peaks, which is around 150 meV for all investigated samples, reveals that E_1 is too small to correspond to the direct emission of carriers from the WL to the GaAs band edge. Therefore, we attribute E_1 to the thermally activated capture of carriers from the WL by nonradiative recombination centers [19-21]. Activation energies of the traps responsible for the quenching of the PL from InAs QDs are in the range 17–83 meV [20].

As shown in Table 1, the activation energy E_2, corresponding to the carrier escape from QDCs or SAQDs, is 220 meV for the SAQDs and around 109-116 meV for the QDCs. Three possible mechanisms for carrier escape from QDs have been proposed in the literature depending on the relation between the activation energy and the band gap difference (ΔE_g): i) Exciton escape when $E_2 = \Delta E_g$ [11,22], ii) single carrier escape when $E_2 < \Delta E_g/2$ [22], and iii) escape of uncorrelated electron-hole pairs when $E_2 = \Delta E_g/2$ [23]. The energy separation between the WL and the GS PL peaks was observed to be 250 meV for both QDCs and SAQDs at the temperature range within which the rapid quenching is

observed. We can thus assume that ΔE_g is close to 250 meV. Therefore, it is clear that the predominant carrier escape mechanism for the SAQDs is exciton escape. In the case of the QDCs, since E_2 is only slightly less than half of the separation of the WL and the GS peaks, it can be either single carrier escape or escape of uncorrelated electron-hole pairs. The confinement energy of the less bound carrier would determine the activation energy of single carrier escape, but since the exact energy level structure of QDCs grown in a groove is unknown, we cannot make a direct comparison. However, since both the barrier materials and the ground state peak energies are the same for SAQDs and QDCs, no major difference is expected between the confinement energies of these two structures. On the other hand, some point defects are expected to form in the regrowth interface of the QDC samples. The electric field induced by the charge fluctuations in these point defects is considered as the cause of the exciton linewidth broadening in site-controlled QDs [24]. However, it should be noted that the UV-NIL process used in this study has been shown to enable fabrication of site-controlled InAs QDs with resolution limited exciton linewidth of 35 μeV using a 30 nm GaAs buffer between the QDs and patterned surface [10]. Thus the density of point defects is expected to be very low. In this study we are using a 60 nm GaAs buffer, which places the QDs even further away from the regrowth interface. Therefore, we can exclude the possibility of direct tunneling of carriers from QDCs to the point defects. On the other hand, the electric field induced by the charge fluctuations in the point defects may disturb the excitons in the thermal escape process, but it is unlikely that this interaction is strong enough to completely break correlation between electrons and holes. Instead, we suggest that the carrier dynamics in the QDCs are affected by interdot interaction. The side-to-side distance between the neighboring QDs along the chains varies from few nanometers to around 15 nm, which may enable capture or tunneling of one carrier type to the neighboring QD during the escape process. In terms of the rate equation model, such process would be similar to single carrier escape since electron (hole) escapes the QDC and hole (electron) returns to the QDC carrier population n_2 by being transferred to the neighboring QD.

According to Table 1, the activation energy E_3 that corresponds to the carrier transfer from the SQDs to QDC[$01\bar{1}$] via the WL is 11 meV, which is reasonable considering that the energy separation between the low energy side of the WL peak and excitons in the SQDs (Fig. 3) is in the range of 5-50 meV. As shown in Fig. 2(a), the influence of carrier transport from the SQDs to QDC[$01\bar{1}$] is significantly reduced when the excitation power is increased up to 5e-3 W. Such behavior is expected with high power excitation because the additional carriers thermally released from the SQDs cannot significantly increase the PL intensity of the QDCs because the GS emission is already at the saturation level.

4. Conclusions

We have presented a study of carrier dynamics in site-controlled QDCs using temperature-dependent PL and a rate equation based model. We have shown that the $[01\bar{1}]$-oriented QDCs exhibit an increase of PL intensity in the temperature range from 20-70 K due to thermally activated carrier transport from the SQDs which are accumulated on the sidewalls of the $[01\bar{1}]$-oriented grooves. The activation energy for this process was estimated to be 11 meV. Furthermore, we have shown that the defect related carrier loss mechanism, which accounts for the PL quenching at low temperatures, is similar for QDCs and SAQD. In addition, the carrier loss mechanism that causes the rapid quenching of SAQD PL at high temperatures was identified as exciton escape, while for the QDCs it is either single carrier escape or escape of uncorrelated electron-hole pairs.

Acknowledgement

We acknowledge D. Steffen for her help with TEM specimen preparation. Financial support from Academy of Finland projects DAUNTLESS (decision number 123951) and DROPLET (decision number 138940) is acknowledged. T. V. Hakkarainen acknowledges financial support from Finnish National Graduate School in Materials Physics and J. Tommila from National Graduate School in Nanoscience (NGS-NANO).

References

[1] Hongbo Lana and Yucheng Ding, Nanotoday **7**, 94-123 (2012).

[2] A. Mohan, M. Felici, P. Gallo, B. Dwir, A. Rudra, J. Faist, and E. Kapon, Nature Photonics **4**, 302 (2010).

[3] C.-J. Wang, L. Y. Lin, and B. A. Parviz, IEEE Journal of Selected Topics in Quantum Electronics **11**, 500 (2005).

[4] S. Kiravittaya, H. Heidemeyer, and O. G. Schmidt, Physica E **23**, 253 (2004).

[5] M. Mehta, D. Reuter, A. Melnikov, A. D. Wieck, and A. Remhof, Appl. Phys. Lett. **91**, 123108 (2007).

[6] P. Alonso-González, L. González, Y. González, D. Fuster, I. Fernández-Martínez, J. Martín-Sánchez, and L. Abelmann, Nanotechnology **18**, 355302 (2007).

[7] T. V. Hakkarainen, J. Tommila, A. Schramm, A. Tukiainen, R. Ahorinta, M. Dumitrescu, and M. Guina, Appl. Phys. Lett. **97**, 173107 (2010).

[8] T. V. Hakkarainen, J. Tommila, A. Schramm, A. Tukiainen, R. Ahorinta, M. Dumitrescu, and M. Guina, Nanotechnology **22**, 295604 (2011).

[9] J. Tommila, A. Tukiainen, J. Viheriälä, A. Schramm, T. Hakkarainen, A. Aho, P. Stenberg, M. Dumitrescu, and M. Guina, J. Cryst. Growth **323**, 183 (2011).

[10] A. Schramm, J. Tommila, C. Sterlow, T. V. Hakkarainen, A. Tukiainen, M. Dumitrescu, A. Mews, T. Kipp, and M. Guina, Nanotechnology **23**, 175701 (2012).

[11] S. Sanguinetti, M. Henini, M. G. Alessi, M. Capizzi, P. Frigeri,and S. Franchi, Phys. Rev. B **60**, 8276 (1999).

[12] E. C. Le Ru, J. Fack, and R. Murray, Phys. Rev. B **67**, 245318 (2003).

[13] Y. Zhang, C. Huang, F. Liu, B. Xu, J. Wu, Y. Chen, D. Ding, W. Jiang, X. Ye, and Z. Wang, J. Appl. Phys. **90**, 1973 (2001).

[14] Yu. I. Mazur, Z. M. Wang, G. G. Tarasov, V. P. Kunets, G. J. Salamo, Z. Y. Zhuchenko, and H. Kissel, J. Appl. Phys. **98**, 053515 (2005).

[15] L. Brusaferri, S. Sanguinetti, E. Grilli, M. Guzzi, A. Bignazzi, F. Bogani, L. Carraresi, M. Colocci, A. Bosacchi, P. Frigeri, and S. Franchi, Appl. Phys. Lett. **69**, 3354 (1996).

[16] Y. Mazur, X. Wang, Z. Wang, G. Salamo, M. Xiao, and H. Kissel, Appl. Phys. Lett. **81**, 2469 (2002)

[17] Y. I. Mazur, Z. M. Wang, G. G. Tarasov, M. Xiao, G. J. Salamo, J. W. Tomm, and V. G. Talalaev, Appl. Phys. Lett. **86**, 063102 (2005).

[18] D. Bimberg, M. Sondergeld and E. Grobe, Phys. Rev. B **4**, 3451 (1971).

[19] D. Colombo, S. Sanguinetti, E. Grilli, M. Guzzi, L. Martinelli, M. Gurioli, P. Frigeri, G. Trevisi, and S. Franchi, J. Appl. Phys. **94**, 6513 (2003)

[20] K. Mukai, N. Ohtsuka, and M. Sugawara, Appl. Phys. Lett. **70**, 2416 (1997)

[21] S. Sanguinetti, D. Colombo, M. Guzzi, E. Grilli, M. Gurioli, L. Seravalli, P. Frigeri, and S. Franchi, Phys. Rev. B 74, 205302 (2006).

[22] G. Gélinas, A. Lanacer, R. Leonelli, R. A. Masut, and P. J. Poole, Phys. Rev. B **81**, 235426 (2010).

[23] W. D. Yang, R. R. Lowe-Webb, H. Lee, and P. C. Sercel, Phys. Rev. B **56**, 13314 (1997).

[24] C. Schneider, A. Huggenberger, T.S. Sünner, T. Heindel, M. Strauß, S. Göpfert, P. Weinmann, S. Reitzenstein, L. Worschech, M. Kamp, S. Höfling, A. Forchel, Nanotechnology **20**, 434012 (2009).

Figure 1: Cross-sectional DFTEM micrographs of (a) QDC[$01\bar{1}$] and (b) QDC[011] obtained using the chemically sensitive **g=**(200) imaging conditions.

Figure 2. Temperature dependency of PL intensity for QDC[$01\bar{1}$], QDC[011], and SAQDs, in (a)-(c), respectively. The insets present PL spectra measured at 20K. The squares, circles, and triangles represent measurement data. The solid lines in (a) are fit curves according to Eq. (2), and in (b) and (c) according to Eq. (3).

Figure 3. Micro-PL spectra measured from QDC[$01\bar{1}$], QDC[011], and SAQDs at the temperature of 5 K using 100 μW excitation at 405 nm.

Figure 4. Schematic representation of the rate equation model.

Table 1. Activation energies of carrier escape channels obtained by fitting the theoretical model to the PL data. The activation energies for QDC[01 $\bar{1}$] were obtained from Eq. (2), and those for QDC[011] and SAQDs from Eq. (3).

Sample	E_1 (meV)	E_2 (meV)	E_3 (meV)
QDC[01-1]	22+/-2	116+/-5	11+/-1
QDC[011]	14+/-2	109+/-10	-
SAQD	17+/-4	220+/-50	

● We grew site-controlled InAs quantum dot chains (QDC) on NIL patterned GaAs(100). ● We perform a temperature-dependent PL study. ● We develop a rate equation model. ● [01-1]-oriented QDCs shown increase of PL at 20-70K. ● QDCs and reference SAQDs exhibit different carrier escape mechanisms. ●

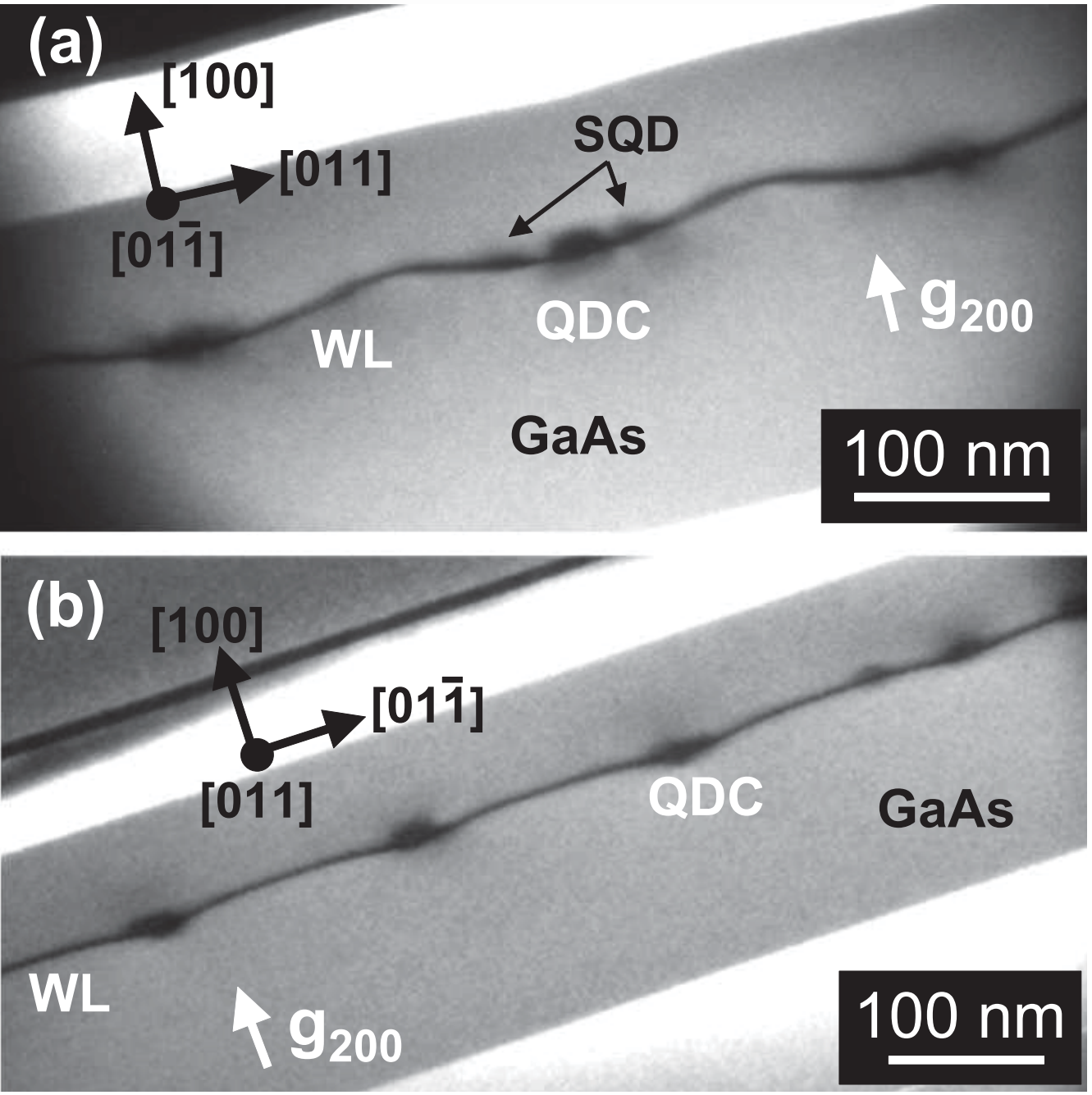

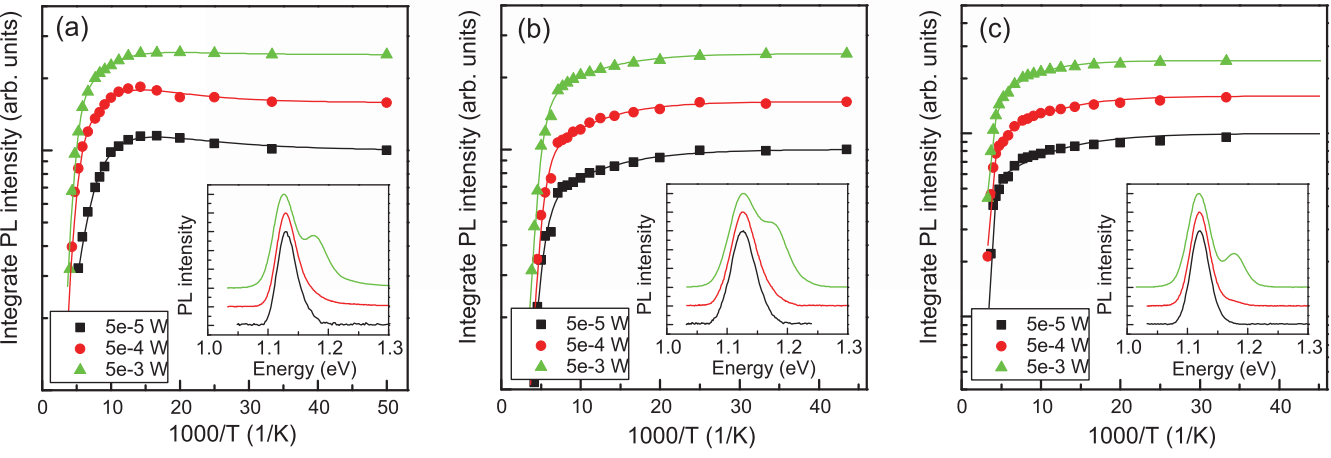

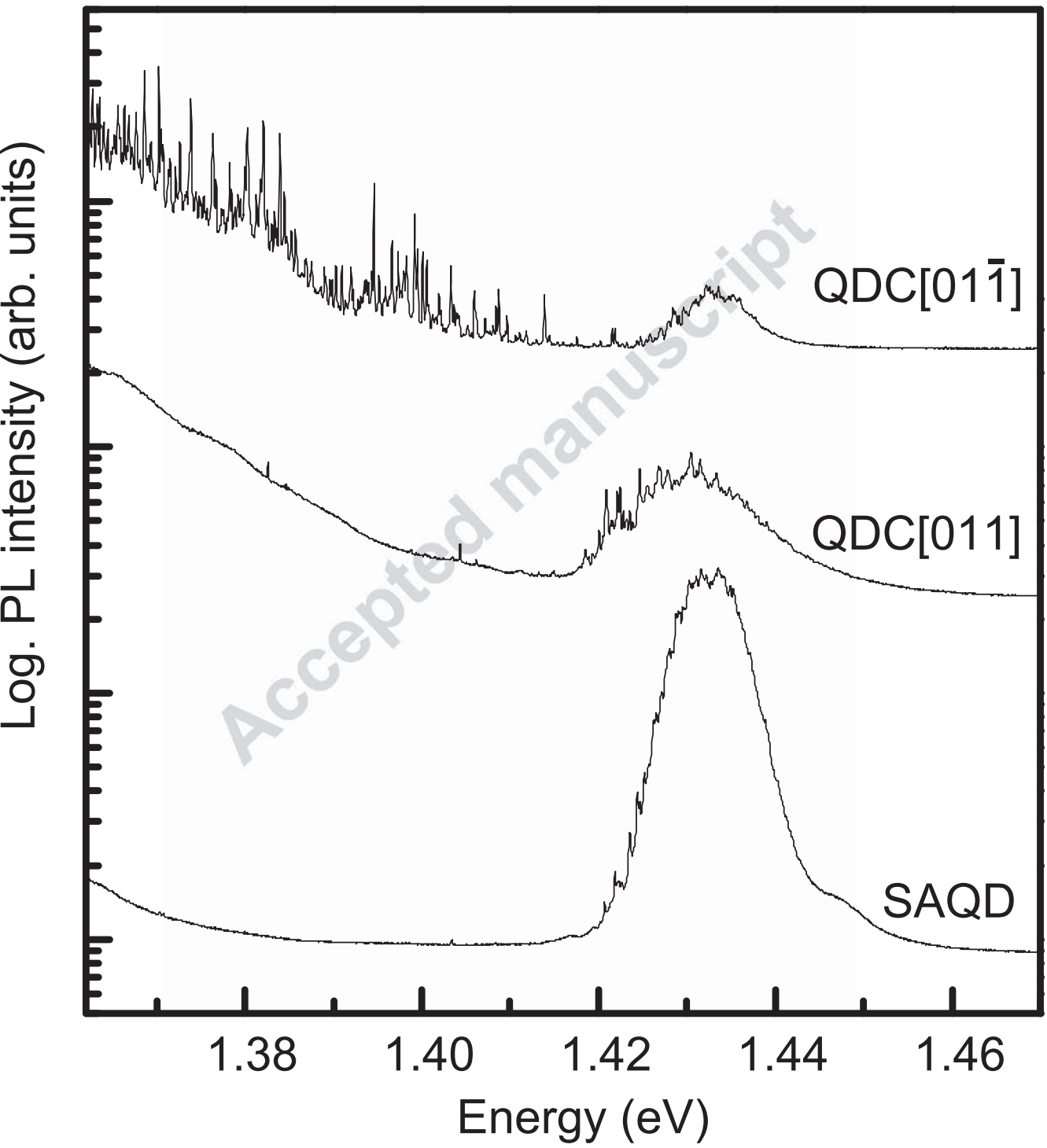

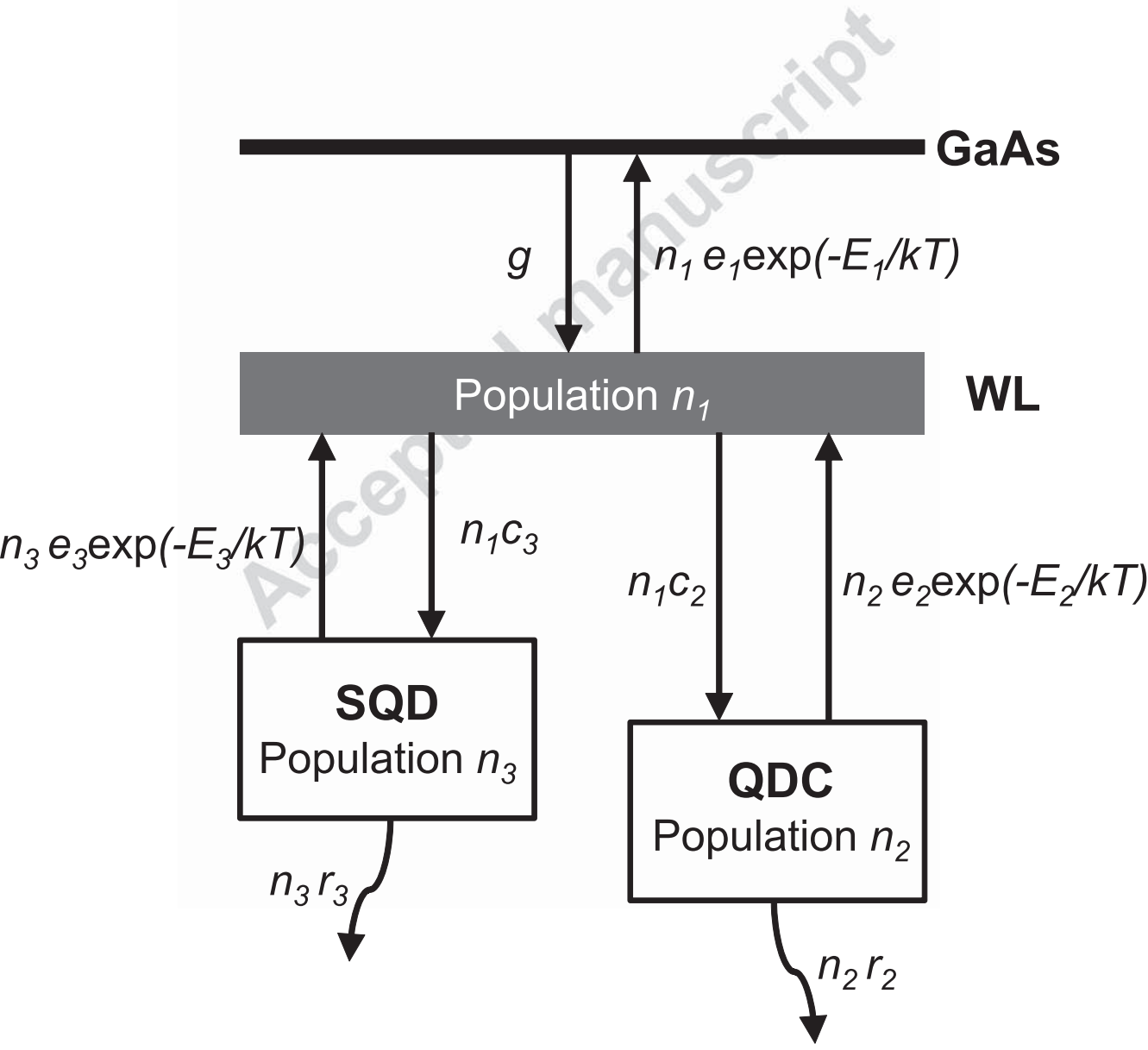

Publication 7

T. V. Hakkarainen, E. Luna, J. Tommila, A. Schramm, and M. Guina, ” Impact of the non-planar morphology of pre-patterned substrates on the structural and electronic properties of embedded site-controlled InAs quantum dots”, Journal of Applied Physics 114, 174304 (2013).

P7

Impact of the non-planar morphology of pre-patterned substrates on the structural and electronic properties of embedded site-controlled InAs quantum dots

T. V. Hakkarainen,[1] E. Luna,[2] J. Tommila,[1] A. Schramm,[1] and M. Guina[1]
[1]*Optoelectronics Research Centre, Tampere University of Technology, P.O. Box 692, FIN-33101 Tampere, Finland*
[2]*Paul-Drude-Institut für Festkörperelektronik, Hausvogteiplatz 5-7, 10117 Berlin, Germany*

(Received 23 August 2013; accepted 18 October 2013; published online 5 November 2013)

We present an experimental and theoretical analysis of the influence of a surface nanopattern on the properties of embedded InAs/GaAs quantum dots (QD). In particular, we analyze QDs grown on nanoimprint lithography (NIL) patterned grooves and investigate the influence of the non-planar surface morphology on the size, shape, strain distribution, and electronic structure of the embedded QDs. We show that the height reduction of InAs QDs during GaAs capping is significantly less pronounced for the QDs grown on the pattern than for the self-assembled QDs. Furthermore, the pattern has a strong impact on the strain and composition profile within the QD. The experimentally observed strain distribution was successfully reproduced with a three-dimensional model assuming an inverse-cone type composition gradient. Moreover, we show that the specific morphology of the QDs grown in the grooves gives rise to an increase of the vertically polarized photoluminescence emission which was explained by employing 8-band **k.p** calculations. Our findings emphasize that the surface curvature of the pattern not only determines the nucleation sites of the QDs but also has a strong impact on their morphological properties including shape, size, composition profile, and strain distribution. These properties are strongly cross-correlated and determine the electronic and optical characteristics of the QDs. © *2013 AIP Publishing LLC*. [http://dx.doi.org/10.1063/1.4828734]

I. INTRODUCTION

The ability to deterministically position InAs quantum dots (QDs) at the moment of nucleation is instrumental for practical approaches to implement future quantum optical devices, such as single-[1] and entangled-photon sources.[2] The deterministic positioning of InAs QDs can be achieved by the so-called site-controlled growth, where the QDs nucleate in pits or grooves defined by various lithography methods, such as nanoimprint lithography (NIL),[3–5] E-beam lithography,[6–8] focused ion beam implantation,[9] interference lithography,[10] or atomic force microscopy lithography.[11] The accumulation of indium adatoms on the lithographically defined locations is driven by local gradients in the surface chemical potential due to surface curvature, strain, as well as the orientation dependent surface free energy.[12,13] However, the patterned surface may influence the shape, composition, and elastic strain fields of the QD and thus determine its electronic structure. Although detailed structural studies on uncapped QDs grown on a patterned surface have already been carried out,[14–16] the influence of the patterned surface on the morphology and chemical properties of embedded QDs is still largely unknown. Yet a thorough understanding of its impact is essential for site-controlled QDs applications, for example, entangled-photon emitters, where polarization-independent emission and minimal fine structure splitting are required.[17]

In this paper, we report on the correlation between the microstructure and the carrier localization of InAs QDs grown by molecular beam epitaxy (MBE) on NIL patterned grooves. The properties of the QDs grown on the pattern are compared to those of self-assembled InAs QDs (SAQD), both types of QDs exhibiting a similar density and size before capping. The influence of the pattern on the morphology of the embedded QDs is investigated by means of a statistical transmission electron microscopy (TEM) analysis. Furthermore, the analysis of high-resolution (HR) TEM micrographs allows mapping the elastic strain distribution in QDs formed both on the pattern and on a planar surface. The observed experimental strain distribution is compared with predictions from a three-dimensional continuum elasticity based model solved using finite-element method (FEM). Our investigations reveal significant structural differences between the site-controlled QDs and the SAQDs. These structural differences are reflected in the electronic properties of the QDs, which are studied by polarization-resolved photoluminescence (PL) experiments and are supported by a quantum mechanical model. By combining the experimental and theoretical results, we are able to get deep understanding of the influence of the groove pattern on the main properties of site-controlled embedded QDs.

The paper is organized as follows. Section II describes the experimental details including the growth of the structures. In Sec. III we present the experimental and computational results in the following order: analysis of the QD morphology by TEM in Sec. III A, polarization-resolved PL measurements in Sec. III B, strain analysis from HRTEM and strain simulations in Sec. III C, and 8-band **k.p** calculations of the electronic properties in Sec. III D. Finally, we

present the discussion and the conclusion in Secs. IV and V, respectively.

II. EXPERIMENTAL DETAILS

Two InAs/GaAs QD structures were grown by MBE on GaAs(100). The first structure, *QD*1, consists of InAs quantum dots regrown on ultraviolet (UV) NIL[3–5,18–21] patterned [01$\bar{1}$]-oriented grooves. Detailed descriptions of the UV-NIL patterning process and chemical surface preparation prior to the regrowth can be found in Refs. 3 and 4. The UV-NIL patterned grooves were overgrown by a 60 nm GaAs buffer at 490 °C. The QDs were grown on the buffer by depositing 2.2 monolayers of InAs at 515 °C. The capping of the QDs was performed in two steps. The first 20 nm of GaAs was deposited on the QDs immediately after the QD growth at 515 °C. Then the temperature was elevated to 590 °C for the growth of 50 nm GaAs layer, 50 nm AlGaAs carrier confinement layer, and 10 nm GaAs cap. The growth rates for GaAs, InAs, and AlGaAs were 0.6 μm/h, 0.05 μm/h, and 1.2 μm/h, respectively. The second structure, *QD*2, consists of self-assembled InAs QDs grown on planar GaAs(100) under identical conditions as QD1. The detailed layer structure of both QD1 and QD2 is schematically shown in Fig. 1. Additional samples with uncapped QDs were prepared for atomic force microscopy (AFM) analysis of the QD heights, which revealed that the QD density is around $1.4 \times 10\,\mathrm{cm}^{-2}$ and average height 12 nm both for the QDs grown on the pattern and for the SAQDs grown on the planar surface. It should be noted that at lower growth temperatures the density of QDs in [01$\bar{1}$]-oriented grooves is limited by anisotropic In adatom migration. On the other hand, if the sample temperature is increased up to 525 °C for the QD growth, the facets that form the groove sidewalls change from (611)A to low surface energy (411)A facets. This gives rise to InAs accumulation on the groove sidewalls, which reduces QD density in the grooves.[18] The influences of the anisotropic In migration and facetted pattern make the situation different compared to InAs deposition on shallow pit patterns, where typically QD density and/or size are larger than on planar area due to the increase of nucleation rate arising from the local surface curvature.[22]

TEM investigations were carried out using a Jeol JEM 3010 microscope operating at 300 kV, equipped with a GATAN slow-scan charge-coupled device camera. Cross-sectional TEM foils were prepared in the [011] and [01$\bar{1}$] projections, using mechanical thinning followed by Ar-ion milling. The optical characterization of the QD structures was performed by polarization-resolved cleaved-edge PL measurements that were carried out in a closed-loop He-cryostat cooled down to 10 K. The PL measurement configuration is schematically illustrated in Fig. 1. The sample was excited by the 405 nm line of a GaN diode laser. The excitation beam was focused on the top surface of the sample with a $f = 200$ mm lens (L1). The PL signal emitted through the cleaved (01$\bar{1}$) facet was collected with a $f = 150$ mm lens (L2). The collection angle of the PL light was narrowed down to approximately 10° with an adjustable aperture (A) in order to prevent collection of light emitted through the top surface of the sample. The intensities of the [100]-oriented transverse magnetic (TM) and [011]-oriented transverse electric (TE) polarization components of the PL emission were measured using a rotatable half-wave plate (WP) and a fixed linear polarizer (POL) that were placed before the entrance slit of a monochromator, as shown in Fig. 1. Finally, the PL intensity was detected with a Peltier-cooled InGaAs photodiode.

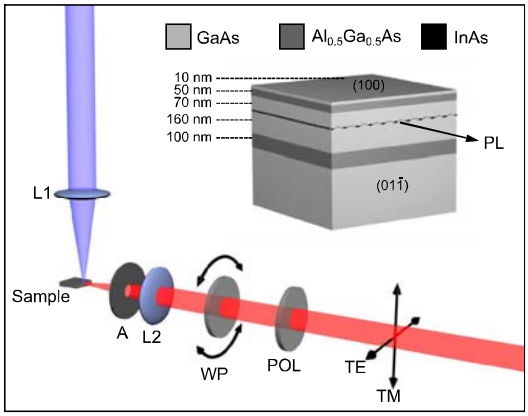

FIG. 1. Schematic illustration of the cleaved-edge PL measurement setup consisting of excitation (L1) and collection (L2) lenses, an adjustable aperture (A), a rotatable half-WP, and a POL. The crossed arrows indicate the electric field orientations for TE and TM polarizations. The inset shows the layer structure of QD1 and QD2 (not in scale).

III. RESULTS

A. Quantum dot morphology

The insets in Figs. 2(b) and 2(c) show exemplary AFM pictures of uncapped QD1 and QD2, respectively. The

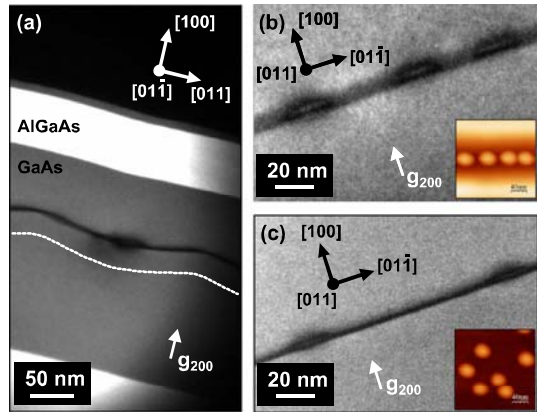

FIG. 2. Chemically sensitive cross-sectional $\mathbf{g} = (200)$ DFTEM micrographs. In (a) and (b) QD1 is viewed along the [01$\bar{1}$] and [011] zone axes, respectively. The dotted line in (a) shows an AFM profile of the groove before QD growth and GaAs capping. (c) Shows QD2 viewed along the [011] zone axis. The insets in (b) and (c) show AFM pictures of QD1 and QD2 before capping. The color scale in the AFM pictures is 24 nm.

average size and density of the QDs is similar on planar and on patterned surfaces. However, the QDs grown on the patterned surface align as a chain in the bottom of the groove. A detailed structural analysis of uncapped QDs on groove patterned GaAs is presented in Ref. 18. The average QD height, determined from a large number of uncapped QDs, is 12 nm for both QD1 and QD2. It is known that the height of the InAs QDs is significantly reduced when they are capped with GaAs (Ref. 23); thus, the height of embedded QDs is dictated not only by their initial height but also by the capping process.

The main panels in Fig. 2 show dark field TEM (DFTEM) micrographs of the capped samples QD1 and QD2. The DFTEM micrographs were taken using two-beam $\mathbf{g}=(200)$ imaging conditions. Since $\mathbf{g}_{200}$ DFTEM is sensitive to the chemical composition for semiconductors with zinc blende structure, it provides a reliable determination of the QDs dimensions and morphology. Due to the chemical sensitivity of the $\mathbf{g}_{200}$ DFTEM imaging conditions, the interface QD/capped layer is clearly identified since the high In content in the QD produces a well-defined and strong change in the intensity contrast at the interface: in In(Ga)As the (200) reflection intensity in kinematic approximation shows a parabolic dependence with the In content with a minimum located in the range between 15% and 20% of In.[24,25] The intensity associated to the QDs studied here, containing about [In] = 90 to 100%, must therefore pass through a minimum at the interfaces where the concentration gradually drops down to zero, giving rise to the dark contrast at the interface and thus allowing the clear identification of the interface position and the QD height. Due to this dependence of $\mathbf{I}_{200}$ on the chemical composition, the use of cross-section $\mathbf{g}_{200}$ DFTEM is highly recommended for reliable QDs size and shape determination.[26,27] Figures 2(a) and 2(b) show $\mathbf{g}_{200}$ DFTEM micrographs of QD1 viewed along the $[01\bar{1}]$ and [011] zone axes, respectively. As observed, QD1 exhibits neither extended defects nor detectable marks or defects arising from the regrowth process. The $[01\bar{1}]$ cross-sectional view [Fig. 2(a)], i.e., along the groove orientation, reveals that (i) the wetting layer (WL) has covered the whole corrugated surface and (ii) the QDs nucleated in the grooves of the pattern. When QD1 is viewed along the [011] zone axis [Fig. 2(b)] we observe a chain of QDs formed in a groove and a projection of the WL that covers the corrugated surface. A truncated pyramidal QD shape with a slight elongation along the $[01\bar{1}]$ direction is observed both for QD1 [Fig. 2(b)] and QD2 [Fig. 2(c)]. A truncated pyramidal cross-section can be associated to several different three-dimensional QD shapes, such as truncated pyramids with square base oriented along either $\langle 001\rangle$[28–30] or $\langle 011\rangle$ directions,[29,31] where the $\langle 001\rangle$ and $\langle 011\rangle$ oriented pyramids are composed of {110} and {111} facetted sidewalls, respectively. There are also several reports of truncated pyramids with octagonal bases,[32–34] which are composed of a combination of {110} and {111} facets. A detailed evaluation of about 40 QDs per sample indicated that the QDs in both QD1 and QD2 are truncated pyramids bound by (100) top facets and inclined side facets. The existence of both {110} and {111} side facets was observed in both samples, but a statistical evaluation of the facet angles revealed that the steeper {111} planes are the predominant facets in QD1 while shallower {110} planes are the predominant facets in QD2.

The DFTEM micrographs reveal also other differences in the morphology of QD1 and QD2. While QD2 [Fig. 2(c)] has a flat bottom, we find that the shape of the groove determines the shape of the lower part of QD1 [Fig. 2(a)]. In particular, we observe that the bottom of QD1 replicates the groove morphology, i.e., it is flat only in a reduced area at the center and curves on the sides towards the groove sidewalls. The dotted line in Fig. 2(a) represents an AFM cross-section of the groove profile before QD growth and GaAs capping. The AFM cross-section is taken from Fig. 3 which shows the groove profile before and after InAs deposition. By comparing the AFM cross-sections in Fig. 3 as well as the TEM picture and the dotted line in Fig. 2(a) we observe that neither InAs deposition nor GaAs capping influences the groove morphology. Furthermore, it is obvious from Fig. 2 that the QDs grown in the grooves are taller than the QDs grown on the planar surface. In order to investigate the QD size in both samples more thoroughly, we have performed a statistical analysis of the QD height h, base width b, and aspect ratio $AR = h/b$. The average QD dimensions and their standard deviations were determined after analyzing more than 40 QDs per sample from DFTEM micrographs with [011] zone axis. As a result, we obtained $h = 8.3\,\text{nm} \pm 1.0\,\text{nm}$, $b = 29.0\,\text{nm} \pm 3.0\,\text{nm}$, and $AR = 0.29 \pm 0.4$ for QD1 and $h = 5.5\,\text{nm} \pm 0.6\,\text{nm}$, $b = 28.1\,\text{nm} \pm 3.1\,\text{nm}$, and $AR = 0.20 \pm 0.3$ for QD2. As these values indicate, AR is significantly larger for QD1 than for QD2, and the difference originates predominantly from the difference in the QD height. Since the height of the QDs before capping was found to be the same (12 nm) for both QD1 and QD2, the difference of the aspect ratios between the QDs grown on the nanopattern and on the planar surface seems to appear during the capping process.

The difference in the aspect ratios of QD1 and QD2 is expected to have a significant impact on their optical

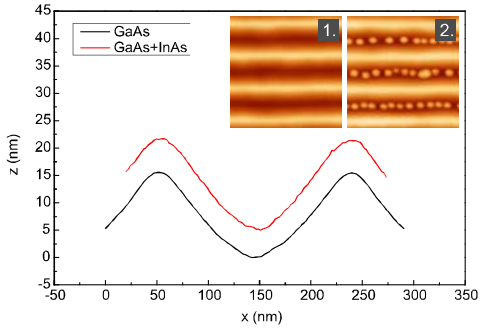

FIG. 3. AFM cross-sections showing the groove shape after the NIL pattern has been overgrown with 60 nm of GaAs and after subsequent deposition of InAs. The cross-sections after the GaAs and InAs depositions are taken from insets 1 and 2, respectively.

properties, as will be discussed in Sec. III B. In particular, the aspect ratio, in conjunction with the compressive strain, determines the polarization of edge-emitted PL from InAs/GaAs SAQDs.[35] Typically the TE polarization dominates over the TM polarization due to the small aspect ratio ($AR < 1$) and compressive strain state of the InAs/GaAs SAQDs, but the relative intensity of the TM polarization with respect to the TE polarization can be enhanced by increasing the AR.[36,37] The magnitude of the TM polarized PL emission is particularly important, for example, for coupling QDs to surface plasmons in a metal film or nanostructure.[38]

B. Photoluminescence polarization

The cleaved-edge PL spectra shown in Figs. 4(a) and 4(b) were measured from the $(01\bar{1})$ facets of QD1 and QD2 as illustrated in Fig. 1. As shown in Figs. 4(a) and 4(b), the PL spectra of both samples show two peaks corresponding to the recombination of electrons and holes in the ground state and in the first excited state, respectively. The position of the ground state peak is 1.12 eV for both QD1 and QD2. Gaussian peaks were fitted to each spectrum in order to obtain the integrated intensities of the ground state peaks I_{TM} and I_{TE} for TM and TE polarizations, respectively. The polarization anisotropy of the PL emission was then determined by the degree of polarization $DOP = (I_{TM} - I_{TE})/(I_{TM} + I_{TE}) \times 100\%$. According to the definition of DOP, positive (negative) values indicate TM (TE) polarized emission and $DOP = 0$ un-polarized emission. By using the intensities obtained from the Gaussian fits we get $DOP = -19\%$ for QD1 and $DOP = -59\%$ for QD2. The polarization anisotropy of QD2 is in agreement with previous observations on InAs/GaAs SAQDs with a similar AR.[36] The nearly un-polarized emission observed for QD1, however, cannot be explained merely by the higher AR since, as deduced from its morphology, the carrier confinement in QD1 should be predominantly in the vertical direction. On the other hand, the QD aspect ratio is not the only factor that determines the polarization anisotropy. Other factors, like the strain state, may play an important role as well. Thus, in Subsections III C–III D we will concentrate on the influence of the groove patterned surface on the strain and composition distribution in the QDs as well as on their impact on the carrier confinement.

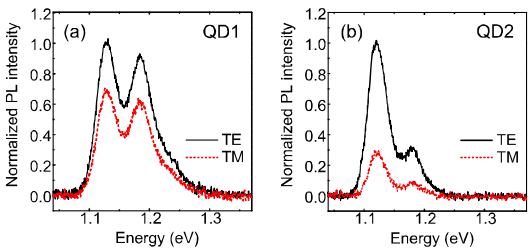

FIG. 4. Cleaved-edge PL spectra for QD1 (a) and QD2 (b) measured at 10 K for TM and TE polarizations.

C. Strain

1. Strain distribution based on HRTEM

The HRTEM micrographs shown in Figs. 5(a) and 5(c) reveal that both QD1 and QD2 grow coherently strained on top of the GaAs prepatterned and planar surfaces, respectively. The coherent strain in the InAs QDs produces a tetragonal distortion of the cubic unit cells that can directly be assessed from the HRTEM images. The thickness of the specimen for HRTEM is 10–50 nm, and hence only one QD is present in most of the HRTEM images. Some HRTEM micrographs reveal signatures of two overlapped QDs. These images, however, were excluded from the strain analysis. In our case, we use the LADIA program package[39] to evaluate the strain distribution. In short, this method is based on the local measurements of the lattice spacing in HRTEM micrographs, where the intensity maxima are identified related to the positions of atomic columns. The positions of these maxima are determined with respect to a reference lattice on the same micrograph, which in our case is the GaAs matrix. The tetragonal lattice distortion of the layer is then the derivative of the displacement between the atomic positions and the reference lattice.[40] Figures 5(b) and 5(d) display the out-of-plane ($\varepsilon_{zz} = \varepsilon_{\perp}$) strain distributions in QD1 and in QD2, derived from the HRTEM micrographs in Figs. 5(a) and 5(c), respectively. The out-of-plane strain is given by

$$\varepsilon_{\perp} = \frac{a_{\perp} - a_{GaAs}}{a_{GaAs}}, \tag{1}$$

where $a_{\perp}$ is the out-of-plane lattice constant and a_{GaAs} is the GaAs lattice parameter. The strain maps in Fig. 5 evidence not only the morphological differences between QD1 and QD2 (in particular, the different h and AR) but also reveal the significant differences in their strain distributions. In QD2, grown on the planar surface, the maximum $\varepsilon_{\perp}$ localizes

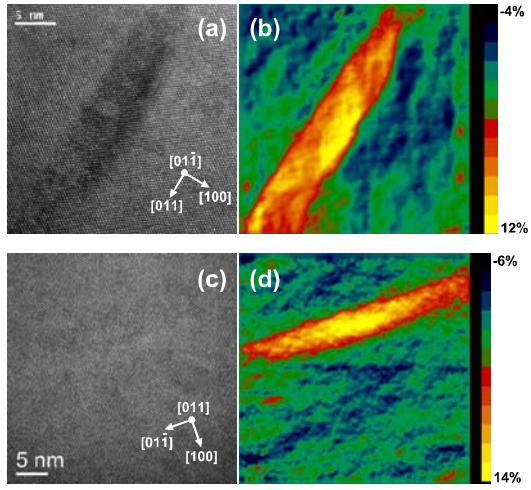

FIG. 5. HRTEM images of QD1 (a) and QD2 (c). (b), (d) Display the out-of-plane strain $\varepsilon_{\perp}$ maps obtained from the HRTEM images in (a) and (c), respectively, after the analysis with the LADIA software.

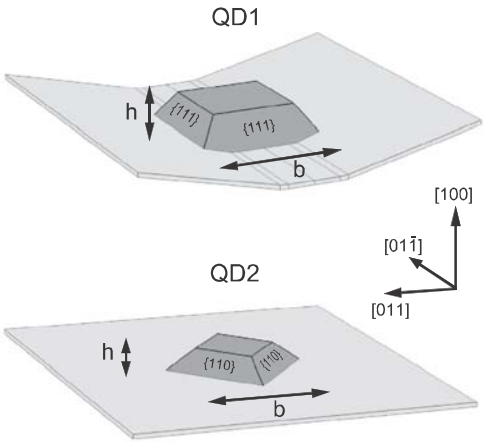

FIG. 6. Schematic illustration of the QD and WL geometries used in the strain simulation for QD1 and QD2. The GaAs matrix has been excluded from the picture for the sake of clarity.

at the center of the QD with $\varepsilon_{\perp(\max)}$ around 12.2%. These features are in agreement with previous works on the strain field of InAs SAQDs.[41,42] On the other hand, unlike QD2, the maximum strain at QD1 localizes at the very top part of the QD and amounts to the lower value of about 10.7%. The examination of QD1 along both [01$\bar{1}$] and [011] zone axes yields the same result, and, in particular, it confirms this specific strain distribution where the maximum strain value localizes at the upper part of the QD.

2. Strain model

The strain distribution in a QD depends on both the composition and the shape of the QD. In order to get a further insight into our experimentally observed different strain distributions in QD1 and QD2, we compare our results with theoretical predictions from continuum mechanical strain simulations. Figure 6 illustrates the QD and WL geometries of QD1 and QD2. The models are constructed based on the DFTEM data. We assume that both QD1 and QD2 are square based truncated pyramids and exclude the lateral elongation for the sake of simplicity. As discussed above, QD1 is bound by (100) top facets and {111} facetted sidewalls while the sidewalls of QD2 are formed by {110} planes and the top by (100) facet. The QD sizes that we use as input parameters for the strain calculations are extracted from the DFTEM statistics. In particular, we assume $b = 29$ nm and $h = 8.3$ nm for QD1 and $b = 28$ nm and $h = 5.5$ nm for QD2. It should be noted that the value of b was determined for both QD1 and QD2 from DFTEM micrographs taken along the [011] zone axis. Consequently, b is the side of the square base of QD1, but it is the diagonal of the base for QD2. Both QD1 and QD2 are standing on a 1 nm thick WL, which is included in the QD height. The morphology of the WL below QD1 is determined from DFTEM micrographs and AFM profiles of the groove (cf., Figs. 2(a) and 3). When observed along the [01$\bar{1}$] direction, we have a 16 nm wide flat section in the bottom of the groove which is surrounded by 13° steep (611)A facetted groove sidewalls,[18] as schematically plot in Fig. 6. The matrix around the QDs is assumed to be pure GaAs.

In order to investigate the influence of the QD morphology on the strain distribution, we first assume that both QDs (i.e., QD1 and QD2) consist of *pure* InAs material. Later we will incorporate a more realistic composition profile into the model. The QD-WL structures shown in Fig. 6 were embedded in a $80 \times 80 \times 80$ nm^3 GaAs matrix, which defined the perimeters of the computational cell. The lattice mismatch between the InAs QD and the GaAs matrix was introduced by pseudo-thermal expansion of the QD.[43] The anisotropy of the elastic properties of GaAs and In(Ga)As crystals was also taken into account in the model. The elastic strain tensor was solved by minimizing the elastic strain energy in 3D by FEM.[44]

Figures 7(a) and 7(b) present 2D cross-sections of $\varepsilon_\perp$ for QD1 and QD2, respectively. The 3D shape of the QD allows elastic strain relaxation which is most pronounced in the

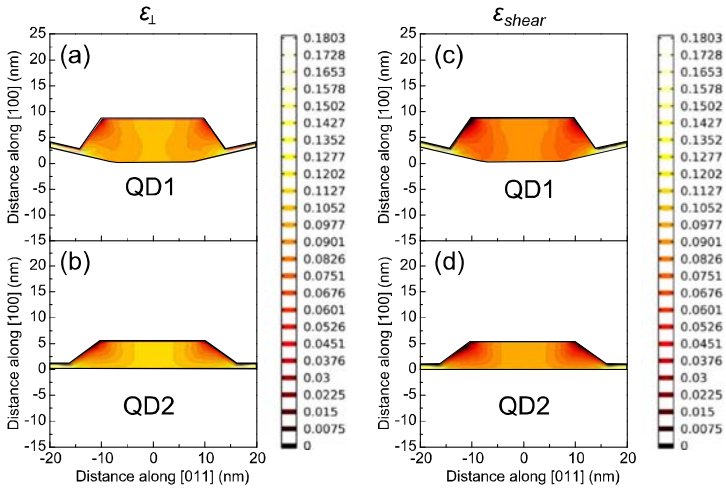

FIG. 7. 2D cross-sectional strain maps obtained from 3D FEM simulations assuming a uniform In composition. (a), (b) Show the out-of-plane strain component $\varepsilon_\perp$ for QD1 and QD2, respectively. (c), (d) Show the shear strain ε_{shear} distribution for QD1 and QD2, respectively. The cross-sections in (a)-(d) are taken along the center of the QD.

upper corners of both QD1 and QD2 as well as in the curved bottom of QD1. As shown in Figs. 7(a) and 7(b), both QD1 and QD2 exhibit an area of uniform high $\varepsilon_\perp$ value in the middle section of the QD. According to the model, the maximum values of $\varepsilon_\perp$ in QD1 and QD2 are 10.9% and 11.7%, respectively. These values are in remarkable agreement with the data extracted from the experimental strain maps shown in Figs. 5(b) and 5(d) (cf., Sec. III C 1). Moreover, an advantage of solving the complete strain tensor is that we can investigate also the magnitude of other strain components, such as (i) the shear strain $\varepsilon_{shear} = \varepsilon'_{zz} - 0.5 \times (\varepsilon'_{xx} + \varepsilon'_{yy})$ that gives rise to the splitting of the heavy and light hole valence bands and (ii) the hydrostatic strain $\varepsilon_{hydro} = \varepsilon'_{xx} + \varepsilon'_{yy} + \varepsilon'_{zz}$ that changes the energy separation between the conduction and valence bands.[45,46] It should be noted here that the strain components ε'_{xx}, ε'_{yy}, *and* ε'_{zz} are calculated with respect to the equilibrium lattice constant of the QD material, and not with respect to the lattice constant of the GaAs substrate like in Eq. (1). Figures 7(c) and 7(d) show the cross-sectional distributions of ε_{shear} in QD1 and QD2, respectively. Both structures QD1 and QD2 have an area of high ε_{shear} in the middle of the QD, but in [01$\bar{1}$] cross-section [Fig. 7(c)] the ε_{shear} distribution of QD1 adopts an hourglass shape due to the additional elastic strain relaxation provided by the curved geometry of the lower part of QD1. Such hourglass distribution is observed neither in QD2 [Fig. 7(d)] nor in [011] cross-section of QD1 (not shown). In the case of compressive strain, it is known that ε_{shear} lifts up the heavy hole band and pulls down the light hole band.[45,46] Therefore, the distribution of ε_{shear} is expected to influence the localization of heavy holes within the QD. In particular, in comparison to QD2, the shear strain distribution of QD1 may provide an additional lateral hole confinement along the [011] direction. On the other hand, according to the strain model, the distribution of ε_{hydro} (not shown) is very uniform within both QD1 and QD2. The value of ε_{hydro} is -8.9% in QD1 and -8.0% in QD2, which would cause a larger strain-induced bandgap widening in QD1 than in QD2.

As we have mentioned already, the main difference in the morphology of QD1 and QD2 concerns the aspect ratio and the shape at the lower part of the QD. In comparison to QD2, the geometry of QD1 provides a more pronounced elastic strain relaxation which results in a smaller $\varepsilon_\perp$ and in a larger magnitude of ε_{hydro}, as well as in a more rapid decay of ε_{shear} towards the lateral sides of the QD. In order to evaluate the relative contributions of *AR* and of the geometry of the bottom of the QD to the strain field, additional simulations were performed for a QD with the same truncated pyramidal shape as QD1 in Fig. 6, but on a planar WL (not shown). This geometry, referred to as QD3, has the same *AR* as QD1, but has a planar bottom like QD2. By comparing the simulation results from these three different QD geometries, we can conclude that 80% of the difference in $\varepsilon_\perp$ and ε_{hydro} between QD1 and QD2 arises from the aspect ratio and 20% from the shape of the bottom of the QD. Interestingly, we find that the waist-shape ε_{shear} distribution in the center of QD1 originates from the peculiar shape at the bottom of QD1, which depends on the groove morphology.

The previous strain calculations, which were performed assuming a uniform InAs composition for the QDs, show that the experimentally observed differences in the maximum value of $\varepsilon_\perp$ between QD1 and QD2 can be accounted for by their different morphologies. However, simulations assuming QDs with a uniform composition (i.e., InAs) do not reproduce the low value of $\varepsilon_\perp$ observed in the bottom part of QD1 [cf., Fig. 5(b)]. Thus, in the following, we will refine our model by introducing a more realistic composition profile for QD1.

Since the experimentally observed strain profile in QD1 [cf., Fig. 5(b)] strongly resembles observations on $In_{0.5}Ga_{0.5}As/GaAs$ QDs where an inverse-cone type composition profile was proposed,[42,47] we incorporate a graded In composition profile of the inverse-cone type in our strain calculations, as illustrated in Figs. 8(a) and 8(b) for QD1 and QD2, respectively. The graded composition profiles have pure InAs material along the line that runs vertically through

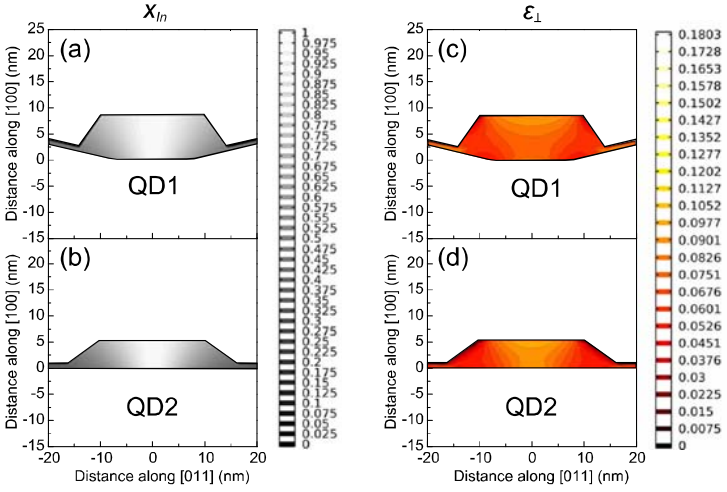

FIG. 8. 2D cross-sections showing an inverse-cone type graded In composition profile (x_{In}) for QD1 (a) and QD2 (b). The out-of-plane strain $\varepsilon_\perp$ distributions for QD1 (c) and QD2 (d) are obtained from FEM simulations using the x_{In} distributions in (a) and (b), respectively. The cross-sections in (a)-(d) are taken along the center of the QD.

the center of the QD and an inverse-cone type gradient towards the bottom corners where the In composition x_{In} is approximately 0.5. Figures 8(c) and 8(d) show the simulated $\varepsilon_{\perp}$ distribution maps for QD1 and QD2 obtained from strain simulations assuming the composition profiles in Figs. 8(a) and 8(b), respectively. As observed, the introduction of the graded composition profile for QD1 [Fig. 8(c)] yields to an excellent agreement both qualitatively and quantitatively between the predicted and the experimental strain maps [cf., Fig. 5(b)]: the model predicts a maximum $\varepsilon_{\perp}$ value of about 10.1% in the upper part of the QD whereas $\varepsilon_{\perp}$ reduces towards the bottom of QD1. Regarding QD2, as shown in Fig. 8(d), the graded composition profile produces a vertical strain gradient which, however, is not observed in the experimental strain maps [cf., Fig. 5(d)]. In this case, the uniform In composition model [Fig. 7(b)] yields a better agreement with the experimental strain distribution [Fig. 5(d)] than the inverse-cone type graded composition profile.

Finally, Figure 9 shows the ε_{shear} and ε_{hydro} distributions calculated for QD1 assuming the inverse-cone composition grading. As shown in Fig. 9(a), the 2D ε_{shear} distribution in the $[01\bar{1}]$ cross-section of QD1 exhibits an hourglass shape similar to what was observed for the uniform composition model in Fig. 7(c) due to the lateral ε_{shear} anisotropy caused by the asymmetric shape of the bottom of the QD. Figure 9(b) shows line profiles of ε_{shear} along the lateral $[01\bar{1}]$ and [011] directions, which demonstrate the existence of the lateral ε_{shear} anisotropy also in QD1 having the inverse-cone composition grading. In particular, the ε_{shear} anisotropy is observed at a distance of approximately 5–8 nm from the center of QD1 at the locations indicated by the arrows in Fig. 9(b). As shown in Fig. 9(c), the distribution of ε_{hydro} in QD1 with graded composition strongly resembles the composition distribution in Fig. 8(a): The magnitude of ε_{hydro} is largest in the center of QD1, and it decreases towards the lower corners. The maximum value of ε_{hydro} in Fig. 9(c) is -9.0%, which is similar to the value obtained assuming the uniform composition model ($\varepsilon_{hydro} = -8.9\%$). Contrary to ε_{shear}, no lateral anisotropy of ε_{hydro} is observed for QD1 with graded composition as shown in Fig. 9(d).

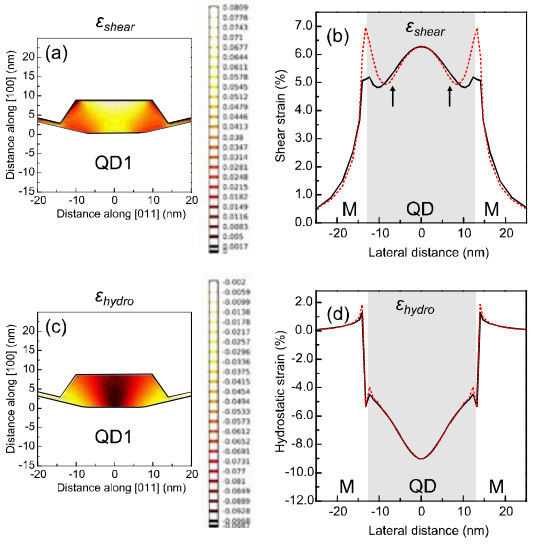

FIG. 9. 2D and 1D cross-sections of the shear strain and the hydrostatic strain distribution for QD1 with inverse-cone type graded In composition profile. The 2D distributions of ε_{shear} (a) and ε_{hydro} (c) are mapped from the $[01\bar{1}]$ cross-sectional plane running through the center of the QD. The 1D line profiles of ε_{shear} (b) and ε_{hydro} (d) are taken along horizontal lines that run through the center of the QD at the height of 2.5 nm. The black (solid) and red (dotted) lines represent $[01\bar{1}]$ and [011] directions, respectively. In (b) and (d) the location of the QD is indicated by the gray background and the GaAs matrix (M) by the white background.

D. Electron and hole states

The impact of the structural differences between QD1 and QD2 on the carrier localization is investigated by solving Schrödinger equation and evaluating the electron and hole wave functions and eigenenergies assuming the QD geometries shown in Fig. 6. From the simulated and experimental strain profiles presented in Sec. III C, we assume that QD1 has an inverse-cone type composition gradient as shown in Fig. 8(a) while QD2 consists of pure InAs. The WL is excluded from the quantum mechanical model for the sake of simplicity. The electron and hole ground state wave functions (Ψ_e and Ψ_h) and the energies (E_e and E_h) in QD1 and QD2 are solved in 3D with an 8-band **k.p** model using the nextnano[3] simulation package.[48,49] Strain and piezoelectricity are included in the model. Figures 10(a) and 10(b) show the simulated confinement potentials as well as the electron and hole ground states in QD1 with an inverse-cone composition gradient and QD2 composed of pure InAs material, respectively. In both QD1 [Fig. 10(a)] and QD2 [Fig. 10(b)], the hole ground states lie very close to the heavy hole valence band edge while the electron ground state in QD1 is located closer to the conduction band edge than in QD2 due to the larger h value in QD1. Moreover, the band gap is larger in QD1 than in QD2 due to the larger hydrostatic strain in QD1. It should be also noted that although both electrons and holes in QD1 are confined around the In-rich center, the tails of their wave functions extend to the In-poor sides of the QD where the band gap is larger. This effect slightly lifts the electron states and lowers the hole states compared with the case of QD1 with a uniform In

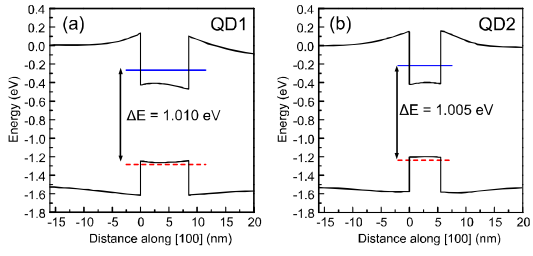

FIG. 10. Simulated conduction and heavy hole valence band edges for QD1 with inverse-cone type graded composition profile (a) and QD2 composed of pure InAs (b). The band edge curves are taken vertically along the center of the QD geometries presented in Fig. 5. The energies of the electron and hole ground states are indicated by the blue (solid) and red (dashed) lines, respectively.

composition (simulation not shown). Consequently, the energy separation between the electron and hole ground states $\Delta E = E_e\text{-}E_h$ is similar for both QD1 and QD2, regardless of the fact that the former has a significantly larger height. In other words, the effects of the difference in the QD height are compensated by the contributions arising from the difference in the hydrostatic strain as well as in the composition. This prediction in fact explains the very similar experimental PL peak energies observed in Fig. 4 for QD1 and QD2, despite their different morphology and composition profile.

Figure 11 shows lateral cross-sections of the valence band edge in QD1 which illustrates the influence of the lateral ε_{shear} anisotropy on the hole confinement. As shown in Fig. 11(a), the heavy hole band exhibits a clear anisotropy between the [011] and [01$\bar{1}$] directions at a distance of approximately 5–8 nm from the center of QD1 (indicated by the arrows), where the heavy hole band edge is located at a lower energy in the [011] direction than along the [01$\bar{1}$] one. It should be noted that this is the same location where the lateral ε_{shear} anisotropy was observed in Fig. 9(b). Generally speaking, the heavy hole band is influenced by both ε_{shear} and ε_{hydro} (Refs. 45 and 46) as well as by the composition profile. The composition gradient used in our model, however, is laterally symmetric; thus, the anisotropy in the heavy hole band edge is caused by an asymmetry in either ε_{shear} or ε_{hydro}. Hence, we evaluate the contributions of ε_{shear} and ε_{hydro} on the heavy hole band anisotropy by looking at the split-off band edge [Fig. 11(b)] which is influenced by ε_{hydro} but not by ε_{shear}.[45,46] It is obvious from Fig. 11(b) that the split-off band edge has only a marginal anisotropy between the [011] and [01$\bar{1}$] directions, which is in agreement with the fact that no lateral anisotropy of ε_{hydro} was observed in Fig. 9(d). Therefore, the anisotropy of the heavy hole band edge originates predominantly from the lateral anisotropy of ε_{shear} (cf., Sec. III C).

Figure 12 shows the probability densities of the ground state electrons and holes calculated for QD1 with the inverse-cone composition gradient and for QD2 composed of pure InAs material. We consider the QDs geometries shown in Fig. 6. We immediately observe that the vertical size of both electron and hole orbitals is larger in QD1 than in QD2

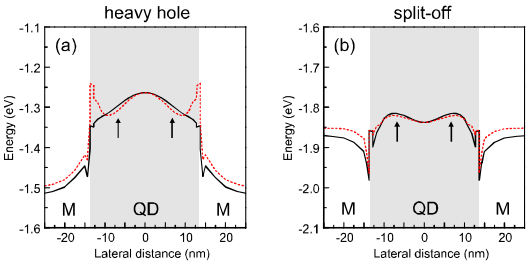

FIG. 11. Simulated heavy hole (a) and split-off (b) valence band edges for QD1 with inverse-cone type graded composition profile. The band edge curves are taken along the horizontal [011] and [01$\bar{1}$] oriented lines that run through the center of QD1 at the height of 2.5 nm. The location of the QD in (a) and (b) is indicated by the gray background and the GaAs matrix (M) by the white background.

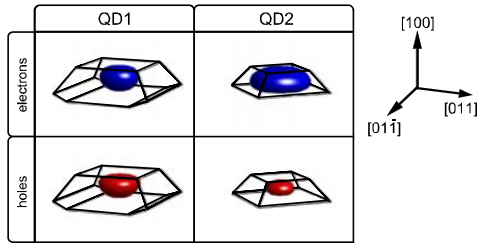

FIG. 12. Probability densities of the ground state electrons and holes for QD1 with inverse-cone type graded composition profile (a) and for QD2 composed of pure InAs (b).

due to the larger value of h in QD1. Moreover, we find that the inverse-cone composition gradient provides an additional lateral carrier confinement in QD1. Note that the anisotropy of both electron and hole orbitals between the vertical [100] direction and the lateral [011] direction is significantly smaller in QD1 than in QD2. Furthermore, the lateral anisotropy of the heavy hole band edge in QD1 [cf., Fig. 11(a)] causes an additional hole confinement along the [011] direction, which gives rise to an in-plane hole anisotropy between the [011] and [01$\bar{1}$] directions. In order to compare the predictions of the quantum-mechanical model with the experimental cleaved-edge PL results shown in Sec. III B, we calculate the theoretical value of *DOP* for the dipole transitions between the electron and hole ground states from the **k.p** momentum matrix elements. The theoretical calculations yield a *DOP* of −21% for QD1 and −61% for QD2. These values are in remarkable agreement with the experimental values of −19% (QD1) and −59% (QD2), respectively, that we obtained from the polarization-resolved cleaved-edge PL measurements.

IV. DISCUSSION

In Sec. III we have shown that despite their similar size before capping, QD1 and QD2 exhibit several structural differences: (i) After capping, the dots in QD1 are taller than in QD2, (ii) the shape of the bottom of QD1 is determined by the groove morphology, and (iii) QD1 exhibits an inverse-cone type graded composition profile whereas QD2 is best described assuming a uniform composition. Furthermore, QD1 loses 31% of its pristine height during the capping process while the height of QD2 is reduced by 54%. Therefore, it is obvious that the patterned surface has a significant effect on the evolution of the QD morphology during the capping process. The reduction of QD height occurs due to the outdiffusion of In atoms from the top of the QD during the deposition of the first monolayers of the GaAs capping layer.[23] This process is driven by the minimization of the elastic energy and of the surface energy. For site-controlled SiGe/Si QDs, it has been shown that the elastic energy before capping is reduced due to the elastic strain relaxation provided by the non-planar shape of the bottom of the QD on the surface pattern.[16] InAs/GaAs QDs grown on the groove pattern are expected to exhibit a similar elastic strain relaxation before capping due to their specific morphology at the

bottom. Thus, owing to the fact that QDs on the patterned surface have already undergone a first elastic relaxation process, the reduction of elastic energy by the dissolution of the top of the QD during the capping process is expected to be less pronounced than in QDs grown on a planar surface. Hence the structural difference (i) is caused by (ii), i.e., the fact that the QDs in QD1 are taller after capping than the QDs in QD2 is a consequence of the non-planar bottom in QD1. On the other hand, once the QDs are fully covered with GaAs, the elastic energy stored in QD1 is expected to be larger than in QD2 because QD1 has a larger volume than QD2. Therefore, QD1 would be more susceptible to undergo strain-driven group III intermixing than QD2.[50] This hypothesis is supported by our experimental observation that QDs grown on a groove pattern intermix more rapidly in post-growth thermal annealing experiments than similar SAQDs grown on a planar surface.[19] Furthermore, it has been shown for the SiGe/Si material system that an increased *AR* increases the tendency for intermixing at the bottom corners of the QDs,[51] inducing the formation of a composition gradient similar to that in Fig. 8(a). Such dependency between the *AR* and intermixing is highly probable also for the InAs/GaAs QDs considering the similarities of the SiGe/Si and InAs/GaAs material systems.[52,53] Thus, process (iii) is a consequence of (i).

From strain simulations, we know that both the specific shape of QD1 as well as the inverse-cone type composition profile have a significant influence on the elastic strain distribution. Compared to QD2 grown on a planar surface, QD1 has a lower out-of-plane strain $\varepsilon_{\perp}$, a larger magnitude of the hydrostatic strain ε_{hydro}, and exhibits a pronounced lateral anisotropy in the shear strain ε_{shear}. It is known that the shear strain causes the splitting of the heavy hole and light hole bands. Furthermore, the confinement of holes is sensitive to the shear strain distribution in the QD, which is strongly affected by the non-planar shape of the bottom of the QD and, hence, by the pattern morphology. In the case of QD1 grown in a groove, we find that the lateral asymmetry of the pattern causes an asymmetry of the hole orbital along the groove direction. In Refs. 3 and 18 we showed that the in-plane optical anisotropy of QDs grown in grooves with different orientations is a combined effect of two components. The first one is the polarization caused by the QD shape elongation which is along the along the $[01\bar{1}]$ direction regardless of the orientation of the groove. As discussed in In Refs. 3 and 18, the second source of in-plane anisotropy causes polarization along the groove direction. Such anisotropy could be caused, for example, by quantum mechanical dot-to-dot coupling along the groove, but in the light of the current evidence, the most probable cause for this second source of polarization is the lateral hole orbital asymmetry discussed above.

Finally, we would like to discuss one of the main practical results of this investigation, which is the influence of the patterned surface on the TM-TE polarization of the QDs. As shown in Fig. 4 and discussed in Sec. III B, QD2 exhibits a TE-dominant PL emission that is typical for flat-bottom compressively strained InAs QDs while the relative intensity of the TM polarized emission is significantly stronger for QD1. This can be partly explained by the different aspect ratios of QD1 and QD2, but in order to fully understand this effect, we have to consider also the influence of the composition gradient as well as the asymmetry of the shear strain distribution in QD1 due to the shape of the bottom of the QD. As shown in Fig. 12, both electrons and holes in QD1 are confined in the In-rich center of the inverse-cone gradient profile, which provides an additional lateral carrier confinement compared to a similar structure with uniform composition. The influence of the composition gradient is especially evident on the electron orbital which in the case of a uniform composition would occupy the complete volume of the QD, as it does in QD2 (cf., Fig. 12). Consequently, both electron and hole orbitals in QD1 are more symmetric than the actual QD shape. Furthermore, it should be taken into account that due to the asymmetric shear strain distribution in QD1, the holes experience a stronger lateral confinement along the [011] direction (perpendicular to the groove) than along the $[01\bar{1}]$ direction (parallel to the groove). All these factors influence the ratio of TM and TE polarizations emitted along the $[01\bar{1}]$ direction. By including the experimentally observed shapes of QD1 and QD2 as well as the composition gradient in QD1 in the calculation of the *DOP*, we obtain an excellent agreement with the experimental PL results.

V. CONCLUSION

We have shown that the growth on a groove patterned surface has a strong impact on the morphology of site-controlled InAs QDs. In particular, the embedded QDs grown on the pattern have an inverse-cone type composition gradient, and they are larger in height than the reference self-assembled QDs grown on a planar surface although their dimensions before capping are similar. Furthermore, we find that the groove determines the shape of the bottom of the QDs which further influences the elastic strain distribution within the QDs. As we have shown, these morphological differences are reflected in the electronic and optical properties of the QDs. In particular, we report on a significant increase of the vertically (TM) polarized PL emission in the QDs grown on the pattern, compared to those grown on the planar surface. The experimentally observed polarization anisotropies are well reproduced with an 8-band **k.p** model assuming the QD morphologies deduced from the structural analysis. By combining experiment and calculations we demonstrate that a nanopattern has a heavy influence on the morphology of the QDs, mainly aspect ratio, strain profile, composition profile. These properties are strongly cross-correlated, and they all influence the electronic and optical characteristics of the QDs. The consequence of our findings is two-fold: (i) The morphology of the pattern has to be carefully considered in order to avoid unwanted optical anisotropies, but (ii) the morphology of the pattern can also be used as a design parameter for obtaining QDs with properties that are precisely suitable for a given application.

ACKNOWLEDGMENTS

We acknowledge D. Steffen for her help with TEM specimen preparation and Dr. J. Simonen for his help with

the FEM calculations. Financial support from Academy of Finland projects Photonics QCA (Decision No. 263594) and DROPLET (Decision No. 138940) as well as INTAS project QUADSYS (ID 70) is acknowledged. T. V. Hakkarainen acknowledges financial support from Finnish National Graduate School in Materials Physics and J. Tommila from the National Graduate School in Nanoscience.

[1]J. Claudon, J. Bleuse, N. S. Malik, M. Bazin, P. Jaffrennou, N. Gregersen, C. Sauvan, P. Lalanne, and J.-M. Gérard, Nat. Photonics **4**, 174 (2010).
[2]R. M. Stevenson, R. J. Young, P. Atkinson, K. Cooper, D. A. Ritchie, and A. J. Shields, Nature **439**, 179–182 (2006).
[3]T. V. Hakkarainen, J. Tommila, A. Schramm, A. Tukiainen, R. Ahorinta, M. Dumitrescu, and M. Guina, Appl. Phys. Lett. **97**, 173107 (2010).
[4]J. Tommila, A. Tukiainen, J. Viheriälä, A. Schramm, T. Hakkarainen, A. Aho, P. Stenberg, M. Dumitrescu, and M. Guina, J. Cryst. Growth **323**, 183 (2011).
[5]A. Schramm, J. Tommila, C. Sterlow, T. V. Hakkarainen, A. Tukiainen, M. Dumitrescu, A. Mews, T. Kipp, and M. Guina, Nanotechnology **23**, 175701 (2012).
[6]C. Schneider, M. Straub, T. Sunner, A. Huggenberger, D. Wiener, S. Reitzenstein, M. Kamp, S. Hofling, and A. Forchel, Appl. Phys. Lett. **92**, 183101 (2008).
[7]J. Skiba-Szymanska, A. Jamil, I. Farrer, M. B. Ward, C. A. Nicoll, D. J. P. Ellis, J. P. Griffiths, D. Anderson, G. A. C. Jones, and D. A. Ritchie, Nanotechnology **22**, 065302 (2011).
[8]K. D. Jöns, P. Atkinson, M. Müller, M. Heldmaier, S. M. Ulrich, O. G. Schmidt, and P. Michler, Nano Lett. **13**, 126 (2013).
[9]Y. Morishita, M. Ishiguro, S. Miura, and Y. Enmei, J. Cryst. Growth **237**, 1291 (2002).
[10]P. Alonso-González, L. González, Y. González, D. Fuster, I. Fernández-Martínez, J. Martín-Sánchez, and L. Abelmann, Nanotechnology **18**, 355302 (2007).
[11]J. Martiin-Saìnchez, G. Muñoz-Matutano, J. Herranz, J. Canet-Ferrer, B. Alén, Y. Gonzaìlez, P. Alonso-González, D. Fuster, L. González, and J. Martiìnez-Pastor, ACS Nano **3**, 1513 (2009).
[12]D. J. Srolovitz, Acta. Metall. **37**, 621 (1988).
[13]N. N. Ledentsov, V. A. Shchukin, M. Grundmann, N. Kirstaedter, J. Böhrer, O. Schmidt, D. Bimberg, V. M. Ustinov, A. Yu. Egorov, A. E. Zhukov, P. S. Kop'ev, S. V. Zaitsev, N. Yu. Gordeev, Z. I. Alferov, A. I. Borokov, A. O. Kosogov, S. S. Ruvimov, P. Werner, U. Gösele, and J. Heydenreich, Phys. Rev. B **54**, 8743 (1996).
[14]G. Biasiol, V. Baranwal, S. Heun, M. Prasciolu, M. Tormen, A. Locatelli, T. O. Mentes, M. A. Niño, and L. Sorba, J. Cryst. Growth **323**, 176 (2011).
[15]S. Kiravittaya, A. Rastelli, and O. G. Schmidt, Appl. Phys. Lett. **87**, 243112 (2005).
[16]Z. Zhong, W. Schwinger, F. Schäffler, G. Bauer, G. Vastola, F. Montalenti, and L. Miglio, Phys. Rev. Lett. **98**, 176102 (2007).
[17]D. J. P. Ellis, R. M. Stevenson, R. J. Young, A. J. Shields, P. Atkinson, and D. A. Ritchie, Appl. Phys. Lett. **90**, 011907 (2007).
[18]T. V. Hakkarainen, J. Tommila, A. Schramm, A. Tukiainen, R. Ahorinta, M. Dumitrescu, and M. Guina, Nanotechnology **22**, 295604 (2011).
[19]T. V. Hakkarainen, V. Polojärvi, A. Schramm, J. Tommila, and M. Guina, Nanotechnology **23**, 115702 (2012).
[20]T. V. Hakkarainen, A. Schramm, J. Tommila, and M. Guina, J. Appl. Phys. **111**, 014306 (2012).
[21]J. Tommila, Ch. Strelow, A. Schramm, T. V. Hakkarainen, M. Dumitrescu, T. Kipp, and M. Guina, Nanoscale Res. Lett. **7**, 313 (2012).
[22]S. Kiravittaya, H. Heidemeyer, and O. Schmidt, Physica E (Amsterdam) **23**, 253 (2004).
[23]G. Costantini, A. Rastelli, C. Manzano, P. Acosta-Diaz, R. Songmuang, G. Katsaros, O. G. Schmidt, and K. Kern, Phys. Rev. Lett. **96**, 226106 (2006).
[24]H. Cerva, Appl. Surf. Sci. **50**, 19 (1991).
[25]E. Luna, A. Trampert, E.-M. Pavelescu, and M. Pessa, New J. Phys. **9**, 405 (2007).
[26]R. Beanland, Ultramicroscopy **102**, 115 (2005).
[27]J. P. McCaffrey, M. D. Robertson, S. Fafard, Z. R. Wasilewski, E. M. Griswold, and L. D. Madsen, J. Appl. Phys. **88**, 2272 (2000).
[28]G. D. Lian, J. Yuan, L. M. Brown, G. H. Kim, and D. A. Ritchie, Appl. Phys. Lett. **73**, 49 (1998).
[29]M. V. Maximov, A. F. Tsatsul'nikov, B. V. Volovik, D. A. Bedarev, A. Y. Egorov, A. E. Zhukov, A. R. Kovsh, N. A. Bert, V. M. Ustinov, P. S. Kop'ev, Z. I. Alferov, N. N. Ledentsov, D. Bimberg, I. P. Soshnikov, and P. Werner, Appl. Phys. Lett. **75**, 2347 (1999).
[30]H. Blank, D. Litvinov, R. Schneider, D. Gerthsen, T. Passow, and K. Scheerschmidt, Cryst. Res. Technol. **44**, 1083 (2009).
[31]F. Heinrichsdorff, A. Krost, M. Grundmann, D. Bimberg, A. Kosogov, and P. Werner, Appl. Phys. Lett. **68**, 3284 (1996).
[32]O. Flebbe, H. Eisele, T. Kalka, F. Heinrichsdorff, A. Krost, D. Bimberg, and M. Dähne, J. Vac. Sci. Technol. B **17**, 1639 (1999).
[33]H. Eisele, O. Flebbe, T. Kalka, C. Preinesberger, F. Heinrichsdorff, A. Krost, D. Bimberg, and M. Dähne, Appl. Phys. Lett. **75**, 106 (1999).
[34]K. Ozasa, Y. Aoyagi, M. Iwaki, and H. Kurata, J. Appl. Phys. **94**, 313 (2003).
[35]A. V. Koudinov, I. A. Akimov, Yu. G. Kusrayev, and F. Henneberger, Phys. Rev. B **70**, 241305 (2004).
[36]P. Jayavel, H. Tanaka, T. Kita, O. Wada, H. Ebe, M. Sugawara, J. Tatebayashi, Y. Arakawa, and T. Akiyama, Appl. Phys. Lett. **84**, 1820 (2004).
[37]M. Usman, V. Tasco, M. Todaro, M. D. Georgi, E. P. O'Reilly, G. Klimeck, and A. Passaseo, Nanotechnology **23**, 165202 (2012).
[38]R. A. Soref, S. Y. Cho, W. R. Buchwald, R. E. Peale, and J. W. Cleary, "Silicon plasmonic waveguides," in *An Introduction to Silicon Photonics*, edited by S. Fathpour and B. Jalali (Taylor and Francis, UK, 2010).
[39]K. Du, Y. Rau, N. Y. Jin-Phillipp, and F. Phillipp, J. Mater. Sci. Technol. **18**, 135–138 (2002).
[40]R. Bierwolf, M. Hohenstein, F. Phillipp, O. Brandt, G. E. Crook, and K. Ploog, Ultramicroscopy **49**, 273–285 (1993).
[41]H.-C. Chung, Y.-F. Lai, C.-P. Liu, Y.-L. Lai, Y.-C. Fang, and L. Hsu, Appl. Phys. Lett. **92**, 051903 (2008).
[42]M. A. Migliorato, A. G. Cullis, M. Fearns, and J. H. Jefferson, Phys. Rev. B **65**, 115316 (2002).
[43]G. R. Liu and Q. Jerry, Semicond. Sci. Technol. **17**, 630 (2002).
[44]T. Benabbas, Y. Androussi, and A. Lefebvre, J. Appl. Phys. **86**, 1945 (1999).
[45]C. G. Van de Walle, Phys. Rev. B **39**, 1871 (1989).
[46]M. P. C. M. Krijn, Semicond. Sci. Technol. **6**, 27 (1991).
[47]N. Liu, J. Tersoff, O. Baklenov, A. L. Holmes, Jr., and C. K. Shih, Phys. Rev. Lett. **84**, 334 (2000).
[48]J. A. Majewski, S. Birner, A. Trellakis, M. Sabathil, and P. Vogl, Phys. Status Solidi C **1**, 2003 (2004).
[49]D. Grützmacher, T. Fromherz, C. Dais, J. Stangl, E. Müller, Y. Ekinci, H. H. Solak, H. Sigg, R. T. Lechner, E. Wintersberger, S. Birner, V. Holý, and G. Bauer, Nano Lett. **7**, 3150 (2007).
[50]M. O. Lipinski, H. Schuler, O. G. Schmidt, K. Eberl, and N. Y. Jin-Phillipp, Appl. Phys. Lett. **77**, 1789 (2000).
[51]D. Digiuni, R. Gatti, and F. Montalenti, Phys. Rev. B **80**, 155436 (2009).
[52]G. Costantini, A. Rastelli, C. Manzano, R. Songmuang, O. G. Schmidt, K. Kern, and H. von Känel, Appl. Phys. Lett. **85**, 5673 (2004).
[53]J. Stangl, V. Holy, and G. Bauer, Rev. Mod. Phys. **76**, 725 (2004).

Tampereen teknillinen yliopisto
PL 527
33101 Tampere

Tampere University of Technology
P.O.B. 527
FI-33101 Tampere, Finland

ISBN 978-952-15-3220-7
ISSN 1459-2045